Lattice QCD static potentials with light quarks and their application to study tetraquarks in the Born-Oppenheimer approximation

Dissertation
zur Erlangung des Doktorgrades
der Naturwissenschaften

vorgelegt beim Fachbereich Physik
der Johann Wolfgang Goethe-Universität
in Frankfurt am Main

von
Lasse Falk Müller
aus Frankfurt am Main, Hessen

Frankfurt am Main 2024
(D30)

vom Fachbereich Physik der
Johann Wolfgang Goethe-Universität als Dissertation angenommen.

Dekan: Prof. Dr. Roger Erb

Gutachter: Prof. Dr. Marc Wagner

Datum der Disputation:

Deutsche Zusammenfassung

Das Standardmodell der Teilchenphysik gilt nach dem aktuellen Stand der Forschung als die vielversprechendste und am gründlichsten erforschte Theorie zur Beschreibung der Wechselwirkungen zwischen den kleinsten Bausteinen der Materie. In diesem wird die starke Wechselwirkung zwischen sogenannten Quarks, Elementarteilchen mit Farbladung, durch die sogenannte Quantenchromodynamik (QCD) beschrieben. Diejenigen Teilchen, die aus Quarks zusammengesetzt sind, werden als Hadronen bezeichnet. Im Rahmen des Quarkmodells können Hadronen entweder aus einem Quark und einem Antiquark bestehen (Mesonen) oder aus drei (Anti)Quarks (Baryonen), wie beispielsweise Protonen und Neutronen, die die Atomkerne bilden. Die QCD erlaubt jedoch auch Zustände, die nicht in dieses Schema passen und daher als exotische Zustände bezeichnet werden. Diese Arbeit konzentriert sich auf sogenannte Tetraquarks, exotische Mesonen, die aus zwei Quarks und zwei Antiquarks bestehen.

Tetraquarks und andere exotische Teilchen stellen ein zunehmend aktuelles Thema in verschiedenen Bereichen der theoretischen und experimentellen Physik dar. Seit etwas mehr als einem Jahrzehnt werden vermehrt Kandidaten für diese Zustände in Beschleunigerexperimenten wie LHCb, BESII und Belle entdeckt. Auf theoretischer Ebene zählt die numerische Methode des Gitter-QCD zu den etabliertesten Verfahren zur Lösung der hochkomplexen Gleichungen der Quantenchromodynamik (QCD). Dabei wird die Raumzeit diskretisiert, und die Felder der Quarks und Gluonen, die die starke Wechselwirkung vermitteln, werden auf und zwischen den Punkten des resultierenden Gitters simuliert. Dies erfordert den Einsatz von Hochleistungsrechnern, auf denen Berechnungen teilweise über Monate oder sogar Jahre hinweg durchgeführt werden müssen.

Die vorliegende Arbeit ist in zwei verwandte, jedoch unabhängige Teile gegliedert. Im ersten Teil wird eine Gitter-QCD-Berechnung durchgeführt, um das Potenzial zwischen zwei statischen Antiquarks in Anwesenheit von zwei dynamischen leichten Quarks zu ermitteln. Obwohl diese Berechnung bereits in der Vergangenheit durchgeführt wurde, zielt dieser Arbeit darauf ab, die bestehenden Ergebnisse signifikant zu verbessern. In dieser Berechnung werden zusätzliche Datenpunkte des Potenzials berücksichtigt, die auch Punkte außerhalb der gleichen Koordinatenachse einschließen. Des Weiteren werden die Daten mithilfe von sogenannten Tree-Level-Verbesserungen behandelt, die auszunutzen, dass sich die Form des Potenzials bei geringen Abständen erfahrungsgemäß ähnlich wie ein Coulomb-Potenzial verhält.

Die Ergebnisse dieser Gitterstudie zeigen vielversprechende Entwicklungen im Vergleich zu bestehenden Resultaten, weisen jedoch noch einige Herausforderungen auf. Eine Hauptmotivation zur präziseren Bestimmung dieser Potenziale war die Diskrepanz in der Bindungsenergie, die mit diesen Potenzialen berechnet werden kann (ungefähr 60 MeV),

im Vergleich zu den Energien aus Gitter-QCD-Berechnungen mit nicht-relativistischen, aber dynamischen schweren Antiquarks (ungefähr 100 MeV). Bedauerlicherweise konnten unsere Ergebnisse dieses Problem nicht vollständig lösen, sie deuten jedoch deutlich darauf hin, dass die Bindungsenergie niedriger ist als bisher angenommen. Zusätzlich haben die neuen Daten das Potenzial, die Form des Potenzials genauer zu bestimmen. Möglicherweise lassen sich in Zukunft auch Erkenntnisse über verwandte Potenziale in der Nukleonenphysik aus diesen Potenzialen ableiten. Es gibt vage Anzeichen für den Ein-Pion-Austausch im langreichweitigen Teil des Potenzials, wie er in der Nukleonenphysik schon lange vermutet wird. Zusammenfassend hat dieser Abschnitt der Arbeit sein angestrebtes Ziel nicht erreicht, stellt jedoch einen vielversprechenden Beginn dar, diese Potenziale in hoher quantitativer Qualität zu berechnen. Im Rahmen der technischen Umsetzung dieser Gitterrechnung und der phänomenologischen Analyse der Ergebnisse wurden erhebliche Fortschritte erzielt.

Der zweite Teil dieser Studie untersucht ein grundlegend anderes Tetraquarksystem, das aus einem schweren Quark-Antiquark-Paar und einem leichten Quark-Antiquark-Paar besteht. Diesmal liegt der Fokus nicht auf der Gitterrechnung für dieses System, sondern auf der Verwendung existierender statischer Potenziale in einem Framework, das mithilfe quantenmechanischer Streutheorie gebundene Zustände und Streuzustände bestimmen kann. Die bestehende Methode, die ursprünglich für zwei gekoppelte Kanäle mit verschwindendem Drehimpuls entwickelt wurde - einen für das Quark-Antiquark-System und einen für das Meson-Meson-System - wird in dieser Studie um einen zusätzlichen Meson-Meson-Kanal mit Strange-Quarks und für beliebige Drehimpulse erweitert. Des Weiteren erfolgt eine Untersuchung der Resonanzen hinsichtlich ihrer Natur als Quark-Antiquark- oder Meson-Meson-Zustand durch Berechnung des Beitrags der jeweiligen Kanäle zur Resonanz.

Die entwickelte Methode ermöglicht eine qualitative Reproduktion der bestehenden experimentellen Ergebnisse. Besonderes Augenmerk liegt dabei auf der Analyse der Resonanzen $\Upsilon(10750)$, $\Upsilon(10860)$ und $\Upsilon(11020)$. Unsere Ergebnisse deuten eindeutig darauf hin, dass $\Upsilon(10750)$ nicht als gewöhnlicher Quark-Antiquark-Zustand anzusehen ist, sondern als krypto-exotischer Zustand vom Typ Υ. Hinsichtlich $\Upsilon(10860)$ können wir die gängige Interpretation als $\Upsilon(5S)$ bestätigen. Für das $\Upsilon(11020)$ haben wir Kandidaten mit Drehimpuls 0 und 2 identifiziert. Allerdings können wir aufgrund der hohen Energie im Rahmen dieser Studie keine definitive Aussage treffen. Obwohl die Ergebnisse das qualitative Spektrum gut widerspiegeln, weisen einige Energien im Vergleich zum Experiment und anderen theoretischen Vorhersagen starke systematische Fehler auf. Diese Diskrepanzen sind teilweise erwartet, da wir Näherungen verwenden und beispielsweise den Spin der schweren Quarks vernachlässigen. Dennoch sind sie auch zum Großteil auf systematische Fehler der Gitterstudie zurückzuführen, die mittlerweile fast 20 Jahre alt ist. Wir gehen davon aus, dass die Qualität der Ergebnisse in diesem Rahmen erheblich von neuen Gitterdaten profitieren würde.

Contents

1 Introduction **1**

I Antistatic-antistatic-light-light lattice QCD static potentials **3**

2 Introduction **5**

3 Lattice QCD **7**
3.1 Path integral formalism . . . 7
3.2 Discretization of gauge fields . . . 8
3.3 Discretization of fermions . . . 8

4 Static-light meson spectroscopy on the lattice **11**
4.1 Operator and correlation function . . . 11
4.1.1 Excited state contamination . . . 12
4.2 Static-light meson mass . . . 12
4.3 Static potentials . . . 14
4.3.1 $\bar{Q}\bar{Q}q_1q_2$ . . . 15
Correlation function . . . 15
Quantum numbers of $\bar{Q}\bar{Q}q_1q_2$ static potentials . . . 17
Angular momentum $|L|$ and rotational symmetry on the lattice . . . 18
Shapes of $\bar{Q}\bar{Q}q_1q_2$ potentials . . . 21
4.3.2 $\bar{Q}Q\bar{q}q$ . . . 22
Correlation function . . . 22
Quantum numbers of $\bar{Q}Q\bar{q}q$ static potentials . . . 23
4.4 Fermion propagator computation . . . 23
4.4.1 Point-to-all propagator . . . 24
4.4.2 Stochastic timeslice-to-all propagators . . . 24
4.5 Smearing techniques . . . 25
4.5.1 APE-smearing of gauge links . . . 25
4.5.2 Gaussian smearing of source and sink . . . 25
4.5.3 HYP static action . . . 26
4.5.4 Projection to SU(3) . . . 26
4.6 Tree-level improvement . . . 27

5 Lattice QCD results for anti-static-anti-static-light-light tetraquark potentials 29
5.1 Lattice setup . . . 29
5.2 Static-light meson masses . . . 30
5.3 Results for $\bar{Q}\bar{Q}ud$ potentials . . . 31
5.3.1 $\bar{Q}\bar{Q}ud$ effective potentials . . . 33
5.3.2 Potentials with asymptotic value $2m^S$ . . . 35
Possible phenomenological explanations of the potentials' behavior . 35
5.3.3 Off-axis separations . . . 38
5.3.4 Results for $\bar{Q}\bar{Q}us$ potentials . . . 39
5.3.5 $\bar{Q}\bar{Q}q_1q_2$ potentials in the Schrödinger equation . . . 40
Fitting ansatz . . . 40
Binding energy . . . 41

6 Conclusion 43

II Bottomonium resonances in the Born-Oppenheimer approximation using lattice QCD static potentials 45

7 Introduction 47

8 Studying bottomonium in the Born-Oppenheimer approximation using static potentials from lattice QCD 49
8.1 Scattering theory in quantum mechanics . . . 49
8.2 Quantum numbers . . . 51
8.3 Coupled channel Schroedinger equation . . . 52
8.4 Relating $V(r)$ to static potentials from lattice QCD . . . 52
8.5 Schrödinger equation for definite angular momentum $\tilde{J}$ . . . 54
8.5.1 Eigenbasis for angular momentum $\tilde{J}$ . . . 54
8.5.2 Partial wave decomposition . . . 56
8.5.3 Projection to definite angular momentum . . . 56
8.5.4 Boundary conditions . . . 58
8.5.5 T-matrix . . . 59
8.6 Extension by a $\bar{M}_sM_s$ channel . . . 60
8.6.1 5x5 coupled channel Schrödinger equation . . . 60
8.6.2 4x4 T-matrix . . . 62
8.7 Quarkonium and meson-meson content . . . 62

9 Results for bottomonium resonances in the Born-Oppenheimer approximation using lattice QCD static potentials 65
9.1 Numerical solution . . . 65
9.1.1 Determination of bound state energies . . . 65

9.1.2 Numerical methods to compute the eigenphase sum $\delta_{\vec{J}}(E)$ and find poles of T(E) in the complex plane . . . 66
9.1.3 Technical difficulties of finding poles in the complex plane . . . 66
9.2 Parameter setting . . . 67
9.3 Eigenphase sum and pole positions in the complex plane . . . 67
9.4 Percentages of quarkonium and meson-meson composition . . . 70
9.5 Comparison to experimental results . . . 72
9.5.1 Bound states . . . 72
9.5.2 Resonances . . . 73
9.6 Systematic errors and comparison to other theoretical predictions . . . 74

10 Conclusion **77**

Bibliography **79**

III Appendix **93**

Appendix **95**

A Conventions **95**

B Additional material for Part I - Antistatic-antistatic-light-light lattice QCD static potentials **97**
B.1 Effective potentials . . . 97
B.2 $\bar{Q}\bar{Q}us$ potentials . . . 100
B.3 Parameters from fitting of $\bar{Q}\bar{Q}q_1q_2$ static potentials . . . 101

C Additional material for Part II - Bottomonium resonances in the Born-Oppenheimer approxima- tion using lattice QCD static potentials **103**
C.1 Percentages of quarkonium and meson-meson composition . . . 103

CHAPTER 1

Introduction

The prevailing theoretical framework for describing the universe at the most fundamental level is the Standard Model of particle physics. This model encompasses three of the four fundamental forces: the strong interaction, the weak interaction, and the electromagnetic interaction, only excluding gravity, which operates on a vastly different scale.

The theory governing the strong interaction is known as Quantum Chromodynamics (QCD). QCD is the dominant force at subatomic distances and is fundamentally different from Quantum Electrodynamics (QED), the theory of electromagnetic interactions at the quantum level. Unlike QED, QCD is a non-abelian gauge theory, meaning its force carriers, the gluons, can interact with each other. This self-interaction property of gluons makes QCD inherently more complex. The elementary particles that participate in strong interactions are termed quarks, and composite particles made of quarks are known as hadrons.

In Quantum Chromodynamics (QCD), three "color" charges must combine into a color singlet, i.e., a color-neutral state, to form a hadron. This can be achieved by pairing a color with its corresponding anti-color or by combining three different colors or anti-colors. The most common and well-studied particles resulting from these combinations are mesons, consisting of a quark-antiquark pair, and baryons, composed of three quarks, each with a different color. Notable examples of baryons include protons and neutrons, the constituents of atomic nuclei collectively known as nucleons.

QCD distinguishes six types of quarks, referred to as "flavors". These quarks exhibit a wide range of masses. The lightest quarks, "up" (u) and "down" (d), have masses of approximately $m_u = 2.2$ MeV and $m_d = 4.7$ MeV, respectively [1]. Due to their relatively small masses, u and d quarks are readily created and annihilated in the QCD vacuum, leading to significant vacuum fluctuations. The other quark flavors are "strange" (s), "charm" (c), "bottom" (b), and "top" (t), with masses of approximately $m_s \approx 93$ MeV, $m_c \approx 1270$ MeV, $m_b \approx 4180$ MeV, and $m_t \approx 172760$ MeV [1].

The masses of the u and d quarks are significantly lower than those of the other quark flavors, which often justifies the approximation $m_u \approx m_d$, leading to the concept of isospin symmetry.

Another essential attribute of particles is the spin quantum number. Quarks, nucleons, and electrons possess a spin of 1/2, classifying them as fermions, particles with half-odd-integer spin. In contrast, mesons and gauge bosons, such as gluons, have a spin of 1, categorizing them as bosons, particles with integer spin. The fundamental distinction between fermions and bosons lies in the Pauli exclusion principle, which dictates that no

two fermions can simultaneously occupy the same quantum state. Conversely, bosons are not subject to this restriction, allowing multiple bosons to coexist in the same quantum state.

QCD also permits more complex hadronic states beyond mesons and baryons, provided they remain color-neutral. These states, known as "exotic states", encompass a variety of theoretically possible configurations. For instance, one can form color singlets by combining two quarks and two antiquarks (tetraquarks) or one quark with four antiquarks (pentaquarks). Additionally, due to the self-interacting nature of gluons, there is the potential for states where gluonic excitations influence the quantum numbers of the system, leading to hybrid mesons. Furthermore, it is theoretically possible to have color-neutral systems composed solely of gluons, known as glueballs. The potential existence of such exotic states has been anticipated since the formulation of QCD [2].

In recent decades, experimental observations have identified several hadronic states that do not conform to the conventional meson or baryon classifications but can be interpreted as exotic hadrons. Due to their initially ambiguous nature, these states are often referred to as "XYZ" states. The first tetraquark candidate, $Z_c(3900)$, was simultaneously discovered by the Belle and BES III collaborations in 2013 [3–5]. Subsequent discoveries of exotic candidates, such as Z_b and Z_c, have been reported by Belle [6], BES III [7–9], and LHCb [10]. Numerous tetraquark candidates have since been found in the past decade [11–24].

A particularly significant discovery was the T_{cc} state, observed by LHCb in recent years [25, 26]. This state lies distinctly below the threshold for a DD^* meson pair, indicating its exotic nature. The T_{cc} state is characterized by its composition of two anti-charm quarks and two light quarks, distinguishing it from conventional charmonium states and making it the first state with an explicit exotic nature.

Conducting calculations within the framework of QCD presents significant challenges due to the self-interacting nature of gluons. Unlike QED, which can be addressed perturbatively through expansions in terms of the small coupling constant $\alpha_{QED} \approx 1/137$, QCD's coupling constant α_{QCD} exhibits a strong dependence on the energy scale. Consequently, perturbative methods are only applicable at high energies or short distances. To address QCD calculations non-perturbatively, one of the most established techniques is lattice QCD, a numerical approach initially proposed by Wilson in 1974 [27].

In lattice QCD, spacetime is discretized, allowing the high-dimensional integrals arising in the path integral formalism to be evaluated numerically. Direct evaluation of these integrals would be computationally too expensive; hence, stochastic "Monte Carlo" methods are employed. These methods utilize importance sampling with the QCD action, significantly reducing computational costs at the expense of introducing statistical noise.

In this thesis, we will use lattice QCD and scattering theory from quantum mechanics to explore heavy-light tetraquarks, i.e. tetraquarks that contain two (anti)bottom quarks in addition to two light quarks, usually a combination of u and d quarks or s quarks.

This work consists of two parts. In the first part, we performed a lattice QCD study of the potential between two static antiquarks and two light quarks. In the second part, we use existing results for the potential between a static quark-antiquark pair in the presence of a light quark-antiquark pair to perform a scattering analysis in the Born-Oppenheimer approximation [28] and extract bound and resonance states.

Part I

Antistatic-antistatic-light-light lattice QCD static potentials

CHAPTER 2

Introduction

This first part of the thesis is about the lattice QCD computation of the potential between two anti-bottom quarks $\bar{b}\bar{b}$ in the presence of two light quarks, e.g. ud (in this thesis, when writing ud it includes the possibilities of the antisymmetric combination $ud - du$, and symmetric combinations, like $ud + du$, which correspond to isospin $I = 0$ and $I = 1$ respectively). This lattice study has been performed in the past [29, 30]; hence, this work aims to improve existing results.

The existing results have been utilized as a potential in a Schrödinger equation within the Born-Oppenheimer approximation to investigate a bound state in the $I(J^P) = 0(1^+)$ $\bar{b}\bar{b}ud$ sector (J denotes the total angular momentum and P the parity) at approximately -90^{+43}_{-36} MeV [30] without incorporating spin effects, and around -59^{+30}_{-30} MeV when spin effects are included [31]. Although there are no experimental observations for this system, multiple lattice computations employing various methodologies exist. Several studies have computed tetraquark masses using non-relativistic bottom quarks, either by solving a generalized eigenvalue problem to extract bound states [32–35], or by determining the bound state via the finite volume method [36–39] as proposed by Martin Lüscher in 1990 [40]. Another notable approach to studying this system is the HAL-QCD method [41] introduced in 2006 [42]. In particular, the binding energies derived from the finite volume method have gained significant acceptance due to multiple consistent results from independent groups and computations in recent years. The latest and most precise of these studies indicate a bound state energy of approximately -100 MeV, which is substantially lower than the values obtained using static potentials (for a comprehensive list of lattice QCD results, refer to Tab. 3 in [43]). One primary objective of our new computation of static $\bar{b}\bar{b}ud$ potentials is to provide a more accurate result and clarify this discrepancy.

The Born-Oppenheimer method has also predicted a resonance state in the $I(J^P) = 0(1^-)$ $\bar{b}\bar{b}ud$ sector [44–46], for which there are no corresponding experimental results or findings from other lattice methodologies.

While the initial investigations of $\bar{b}\bar{b}ud$ lattice QCD static potentials [29, 30] have yielded valuable insights, several limitations remain. The prior results were derived using twisted mass fermions, which inherently break the parity quantum number and, thus, are suboptimal for hadron spectroscopy. Additionally, the limited number of data points with significant uncertainties used to fit the potential has led to substantial statistical errors in the fit parameters, which in turn propagate to large uncertainties in the binding energies obtained from solving the Schrödinger equation. It is anticipated that applying modern lattice QCD techniques will enhance the precision of binding energy calculations

and resolve the discrepancies between the Born-Oppenheimer approximation results and those from different lattice QCD methodologies.

Moreover, refined results could be employed to investigate the $0(0^+)$ and $0(1^+)$ $\bar{b}\bar{c}ud$ systems. Previous lattice studies using the finite volume method have identified very shallow bound states with binding energies of only a few MeV in both sectors [47]. Although the static approximation becomes less accurate for lighter heavy quark masses, such as when one $\bar{b}$ quark is replaced by a $\bar{c}$ quark, it is anticipated that meaningful qualitative insights can still be derived for these channels.

It would be particularly interesting to consider experimentally observed systems, such as the T_{cc}. However, treating two $\bar{c}$ quarks within the static limit is questionable and is not expected to yield a reliable approximation. Nonetheless, it remains feasible to utilize the static potentials with additional relativistic $1/m_c$ corrections, which can be computed perturbatively within the framework of potential Non-Relativistic QCD (pNRQCD), an effective field theory [48–51]. Furthermore, these corrections can also be computed on the lattice, although this has proven to be a challenging endeavor [52–54].

Different heavy quark systems can be investigated utilizing the same static potential derived from lattice computations. However, to explore systems with varying light quark content, it is necessary to compute additional potentials. While the $\bar{b}\bar{b}us$ system has been examined in lattice studies alongside the $\bar{b}\bar{b}ud$ system, the static potentials for the former have not been previously computed. Therefore, a significant objective of this work is to compute the static potentials for the $\bar{b}\bar{b}us$ system for the first time.

This first part of the thesis is focused on a lattice QCD computation of antistatic-antistatic-light-light potentials. Thus, we begin by briefly formulating the fundamental principles of lattice QCD in Chapter 3, followed by a discussion of static-light meson spectroscopy in Chapter 4 with a focus on the relevant systems, that are studied in this work. Finally, in Chapter 5 we will present and discuss the results for $\bar{b}\bar{b}ud$ and $\bar{b}\bar{b}us$ static potentials.

CHAPTER 3

Lattice QCD

Lattice QCD is a non-perturbative approach to Quantum Chromodynamics (QCD), which is based on the discretization of space-time in a finite volume. The idea is to solve the high-dimensional integrals that appear when treating QCD with the path integral formalism in a stochastic manner. To this end, we transform the Minkowski space-time to Euclidean space-time by modifying the action according to $S_M \to iS_E$. This transformation eliminates the complex oscillations in the integration weight $\exp(iS_M) \to \exp(-S_E)$, allowing us to interpret this exponential as a probability distribution for performing importance sampling.

In this section, we briefly introduce lattice QCD and establish fundamental equations for later reference in this work. First, we explain the path integral formalism. Subsequently, we introduce the discretization of gauge and fermion fields.

We refer to standard textbooks such as [55, 56] for a more comprehensive and complete introduction to lattice QCD.

3.1 Path integral formalism

The path integral formalism is based on the principle of least action. In a quantum field theory like QCD, this translates to integration over all possible field configurations weighted by the action. We introduce the integration measure $\mathcal{D}\phi = \Pi_n \mathrm{d}\phi_n$, where n counts all possible field configurations. The expectation value of an observable $\mathcal{O}$ can then be expressed as

$$\langle \mathcal{O} \rangle = \frac{1}{Z} \int \mathcal{D}\psi \mathcal{D}\bar{\psi} \mathcal{D}A \, \mathcal{O}[\psi, \bar{\psi}, A] \, e^{-S_E[\psi, \bar{\psi}, A]}, \tag{3.1}$$

where ψ and $\bar{\psi}$ denote fermion fields, A corresponds to the gauge field and the normalization Z is the partition function given by

$$Z = \int \mathcal{D}\psi \mathcal{D}\bar{\psi} \mathcal{D}A \, e^{-S_E[\psi, \bar{\psi}, A]}. \tag{3.2}$$

The Euclidean action S_E is a functional of the fields ψ, $\bar{\psi}$, and A, and can be written as the sum of the gauge action $S_G[A]$ and the fermion action $S_F[\psi, \bar{\psi}, A]$. The gauge action is defined as

$$S_G[A] = \frac{1}{4} \int \mathrm{d}^4x \, F^a_{\mu\nu}(x) F^{\mu\nu}_a(x), \tag{3.3}$$

where $F^a_{\mu\nu}(x)$ represents the field strength tensor. The fermion action is given by

$$S_F[\psi, \bar{\psi}, A] = \int \mathrm{d}^4x\, \bar{\psi}(x)\left(\gamma_\mu D_\mu + m\right)\psi(x), \tag{3.4}$$

where γ_μ are the Dirac matrices, $D_\mu = \partial_\mu - igA_\mu(x)$ is the covariant derivative with the gauge coupling g, $\bar{\psi} = \psi^\dagger\gamma_0$ and m is the fermion mass.

3.2 Discretization of gauge fields

To discretize gauge fields, we rewrite $A_\mu(x)$ in terms of link variables

$$U_\mu(x) = e^{iagA_\mu(x)}, \tag{3.5}$$

where a is the lattice spacing. These link variables are elements of the gauge group $SU(3)$ and can be interpreted as the parallel transport of gauge bosons along the lattice. We define the plaquette $U_{\mu\nu}(x)$ as the product of link variables around the smallest possible loop in μ-ν directions starting at x, i.e.

$$U_{\mu\nu}(x) = U_\mu(x)U_\nu(x + a\hat{\mu})U^\dagger_\mu(x + a\hat{\nu})U^\dagger_\nu(x). \tag{3.6}$$

This plaquette is used in the fundamental discretization of the gauge action, the Wilson plaquette action [27],

$$S_G[A] = \frac{2}{g^2}\sum_{x,\mu<\nu}\left(1 - \frac{1}{3}\mathrm{ReTr}\left[U_{\mu\nu}(x)\right]\right). \tag{3.7}$$

This discretization approximates the gauge action up to $\mathcal{O}(a^2)$, which is sufficient for most studies as discretization effects are already quite small. The Wilson action can be further improved up to higher order in a by using the Lüscher-Weisz [57] or Iwasaki [58] gauge action.

3.3 Discretization of fermions

The fermion action can be discretized naively as

$$S_F^{\mathrm{naive}}[\psi, \bar{\psi}, U] = a^4\sum_x \bar{\psi}(x)D(x,y)\psi(y) \tag{3.8}$$

with the lattice Dirac operator $D(x,y)$ given by

$$D(x,y) = \sum_\mu \gamma_\mu \frac{U_\mu(x)\delta_{x+\hat{\mu},y} - U_{-\mu}(x)\delta_{x-\hat{\mu},y}}{2a} + m\delta_{x,y}. \tag{3.9}$$

The lattice propagator is the inverse of the Dirac operator. The lattice propagator for a free fermion in momentum space reads

$$\left(\tilde{D}_{\text{free}}\right)^{-1}(p) = \frac{m - \frac{i}{a}\sum_\mu \gamma_\mu \sin\left(p_\mu a\right)}{m^2 + \frac{1}{a^2}\sum_\mu \sin^2\left(p_\mu a\right)}. \tag{3.10}$$

A pole in the propagator corresponds to a fermion. It is easy to see that for a massless particle in the continuum limit, the pole is at $p = 0$,

$$\left(\tilde{D}_{\text{free}}\right)^{-1}(p) \xrightarrow[m\to 0]{a\to 0} \frac{-i\sum_\mu \gamma_\mu p_\mu}{p^2}. \tag{3.11}$$

On the lattice, $\left(\tilde{D_{\text{free}}}\right)^{-1}(p)$ also has a pole at $p = 0$. However, Eqn. (3.10) for a free fermion (i.e., $m = 0$) has poles not only for $p_\mu = 0$ but also $p_\mu = \pi/a$ (The momentum on the lattice is restricted to $-\pi/a < p_\mu \leq \pi/a$). With four components for the momentum, this leads to sixteen poles, one physical pole at $p = (0,0,0,0)$ and fifteen unphysical poles, where at least one of the four components is π/a. This so-called doubling problem leads to severe issues when simulating fermions on the lattice.

There are many ways to remove the doublers by changing the discretization while keeping the correct continuum limit (see [55]). In this thesis, we only used the method of Wilson fermions.

The idea of Wilson fermions is to add a term to the Dirac operator that distinguishes the physical pole from the doublers. The Wilson Dirac operator is given by

$$\tilde{D}_{\text{Wilson}}(p) = \tilde{D}(p) + \frac{1}{a}\sum_\mu \left(1 - \cos(p_\mu a)\right). \tag{3.12}$$

For the physical pole, i.e., $p = (0,0,0,0)$, the additional term vanishes. However, for the doublers, the additional term is non-zero and provides an additional term of $2/a$, which acts as an increased mass. This mass is inversely proportional to the lattice spacing a and thus diverges in the continuum limit, decoupling the doublers from the theory.

Wilson fermions obey symmetries like charge conjugation and parity, particularly important for hadron spectroscopy. The major downside of the addition by the Wilson term is that chiral symmetry is explicitly broken. Different fermion discretizations have been developed to address this issue. However, they contain different disadvantageous properties, such as significantly higher computational cost (domain-wall fermions [59, 60]) or the introduction of additional particle properties that have to be accounted for (staggered fermions [61]).

The standard Wilson fermion action from Eqn. (3.12) still contains discretization errors of $\mathcal{O}(a)$. These errors can be reduced to $\mathcal{O}(a^2)$ using Symanzik improvement [57, 62, 63], yielding so-called Wilson-Clover fermions.

CHAPTER 4

Static-light meson spectroscopy on the lattice

The masses of hadrons represent fundamental fermionic observables that can be computed on the lattice. By investigating particles with distinct quantum numbers, such as spin, parity, and flavor content, it is feasible to calculate the masses of various hadrons and thereby probe Quantum Chromodynamics (QCD) through comparison with experimental data.

This work focuses on meson states containing at least one heavy quark. The t quark is the heaviest, but its mean lifetime is approximately 10^{-25} seconds [1], causing it to decay into lighter quarks before forming hadronic states. Consequently, the term "heavy quark" typically refers to b quarks and rarely to c quarks. Studying observables involving bottom quarks in lattice QCD is challenging due to the small Compton wavelength (λ_C) of such heavy particles, which is difficult to resolve with commonly used lattice spacings.

One approach to address this issue is to employ an effective non-relativistic Lagrangian for bottom quarks [64–66], which has been utilized in studies of doubly heavy tetraquark systems involving the finite volume method [36, 38, 47]. Instead, we consider the limit of infinite mass for the heavy quarks, effectively treating them as static color sources without any dynamics.

A distinctive feature of static quarks is the well-defined distance between them, unlike dynamical quarks, which are not localized. This allows for defining a static potential $V(r)$ as a function of the separation distance r between two static quarks.

Throughout this chapter and Chapter 5, static quarks will be denoted as Q and light quarks as q.

We begin by describing the construction of operators in a general framework. Subsequently, we delve into the static-light meson system $\bar{Q}q$. Following this, we introduce the well-known static quark-antiquark potential. Finally, we explore the more complex static potentials for two-meson systems, deriving the correlation function for a system of two static-light mesons ($\bar{Q}\bar{Q}q_1q_2$). We conclude by outlining the steps to compute the correlation function for a $\bar{Q}Q\bar{q}q$ system, which will become important in the second part of this thesis.

4.1 Operator and correlation function

To investigate the mass or potential of a quark system, we begin by constructing an operator $\mathcal{O}(t)$ that has a significant overlap with the ground state. The correlation function is then defined as

$$\mathcal{C}(t_2 - t_1) = \left\langle \Omega \,\middle|\, \mathcal{O}^\dagger(t_2)\mathcal{O}(t_1) \,\middle|\, \Omega \right\rangle, \tag{4.1}$$

where $|\Omega\rangle$ represents the vacuum state. By inserting a complete set of states $\sum_n |n\rangle \langle n|$, the correlation function can be expressed as

$$\begin{aligned}\mathcal{C}(t_2 - t_1) &= \sum_n \left\langle \Omega \,\middle|\, \mathcal{O}^\dagger(t_2) \,\middle|\, n \right\rangle \langle n|\mathcal{O}(t_1)|\Omega\rangle \, \mathrm{e}^{-E_n(t_2-t_1)} \\ &\xrightarrow[t_2-t_1\to\infty]{} |\langle 0|\mathcal{O}|\Omega\rangle|^2 \, \mathrm{e}^{-E_0(t_2-t_1)},\end{aligned} \tag{4.2}$$

where, in the second step, we take the limit of large time separation $t = t_2 - t_1$, such that all excited states are exponentially suppressed, leaving only the ground state with energy E_0. By fitting an exponential function to the correlation function at large time separations t, we can extract the ground state energy E_0 and thus determine the state's mass. A more practical approach is to define an effective mass $m_{\mathrm{eff}}(t)$ as

$$am_{\mathrm{eff}}(t) = \ln\left(\frac{\mathcal{C}(t-a)}{\mathcal{C}(t)}\right), \tag{4.3}$$

and fit a constant for large time separations t.

4.1.1 Excited state contamination

The limit $t \to \infty$ must be approximated by a finite $t = t_{\max}$. Ideally, $t_{\max}$ is chosen such that the contribution of excited states is negligible. The contribution of the first excited state to the effective mass can be included by writing

$$am_{\mathrm{eff}}(t) = \ln\left(\frac{\mathcal{C}(t-a)}{\mathcal{C}(t)}\right) + \varepsilon(t) \tag{4.4}$$

with

$$\varepsilon(t) = \mathcal{O}\left(e^{-\Delta E t}\right), \quad \Delta E = E_1 - E_0, \tag{4.5}$$

where E_1 is the energy of the first excited state. This was initially proposed and demonstrated in the context of correlation matrices and the generalized eigenvalue problem [67].

This implies that if ΔE is small, i.e., the first excited state is close to the ground state, $t_{\max}$ generally needs to be larger to suppress the excitation. To put this into perspective, consider the relevant systems in this work, which involve heavy-light mesons, where typically $\Delta E \approx 400$ MeV ≈ 0.5 fm^{-1}. Thus, after $t = 0.5$ fm, the excited state is only suppressed by a factor of $1/e \approx 0.37$.

4.2 Static-light meson mass

The static-light meson consists of a static antiquark $\bar{Q}$ and a light quark q. We can construct a trial state for a static-light meson with the operator

$$\mathcal{O}^{\Gamma}_{\bar{Q}q}(\mathbf{r}) = \bar{Q}^a_A(\mathbf{r}) \Gamma_{AB} q^a_B(\mathbf{r}), \tag{4.6}$$

where a,b are color indices and A, B are spin indices. Typically, Γ is chosen to ensure that the trial state only overlaps with a particular sector, i.e., states with the same quantum numbers. This system's set of quantum numbers includes parity $\mathcal{P}$ and total angular momentum J. Note that, in the static limit, the heavy quark spin decouples from the system. Thus, the angular momentum quantum numbers of the light degrees of freedom determine the system's total angular momentum $j = |l \pm 1/2|$. We only consider vanishing orbital angular momentum $l = 0$; thus, the light quark spin dictates $j = 1/2, j_z = -1/2, +1/2$. This leads to two relevant choices for Γ in Eqn. (4.6):

- $\Gamma = (1+\gamma_0)\gamma_5/2$, which yields an S-wave state, i.e., $l = 0$, with $|j| = 1/2$ and $\mathcal{P} = -$. In terms of B mesons ($\bar{b}q$ with $q = u/d$), this would correspond to either $J^{\mathcal{P}} = 0^-$ ($B^{\pm}$ or B^0 meson) or $J^{\mathcal{P}} = 1^-$ (B^* meson) from experiment. We label this state as S.

- $\Gamma = (1+\gamma_0)/2$ or $\Gamma = (1-\gamma_0)\gamma_j\gamma_5/2$, which yields a state consisting of both S-wave and P-wave contributions and $\mathcal{P} = +$. In terms of B mesons, the possible experimental counterparts are (B_0^*) ($J^{\mathcal{P}} = 0^+$) and (B_1^*) ($J^{\mathcal{P}} = 1^+$) [68, 69]. We label this state as P_-.

With the operator (4.6), we can construct the correlation function

$$\begin{aligned}
\mathcal{C}^{\Gamma}_{\bar{Q}q}(t_2 - t_1) &= \left\langle \Omega \,\middle|\, \left(\bar{Q}^a_A(\mathbf{r}, t_2)\Gamma_{AB} q^a_B(\mathbf{r}, t_2)\right)^\dagger \bar{Q}^b_C(\mathbf{r}, t_1)\Gamma_{CD} q^b_C(\mathbf{r}, t_1) \,\middle|\, \Omega \right\rangle \\
&= \left\langle \Omega \,\middle|\, q^a_B(\mathbf{r}, t_2)^\dagger \Gamma^\dagger_{AB} \bar{Q}^a_A(\mathbf{r}, t_2)^\dagger \bar{Q}^b_C(\mathbf{r}, t_1)\Gamma_{CD} q^b_C(\mathbf{r}, t_1) \,\middle|\, \Omega \right\rangle \\
&= \left\langle \Omega \,\middle|\, \bar{q}^a_B(\mathbf{r}, t_2) \left(\gamma_0 \Gamma^\dagger_{AB} \gamma_0\right) Q^a_A(\mathbf{r}, t_2) \bar{Q}^b_C(\mathbf{r}, t_1)\Gamma_{CD} q^b_C(\mathbf{r}, t_1) \,\middle|\, \Omega \right\rangle \\
&= -\left\langle \Omega \,\middle|\, \left(\gamma_0 \Gamma^\dagger_{AB} \gamma_0\right) Q^a_A(\mathbf{r}, t_2) \bar{Q}^b_C(\mathbf{r}, t_1)\Gamma_{CD} \bar{q}^a_B(\mathbf{r}, t_2) q^b_C(\mathbf{r}, t_1) \,\middle|\, \Omega \right\rangle,
\end{aligned} \tag{4.7}$$

where we used that the quark fields are Grassmann variables and thus anticommute. We now integrate over all fermion fields to obtain a static propagator $\left(\mathcal{Q}^{-1}\right)^{ab}_{AB}(\mathbf{r}, t_2; \mathbf{r}, t_1)$ and a dynamic light propagator $\left(\mathcal{D}^{-1}\right)^{ab}_{AB}(\mathbf{r}, t_2; \mathbf{r}, t_1)$ and introduce $< ... >$ as a path integral over all gauge configurations to obtain

$$\begin{aligned}
\mathcal{C}^{\Gamma}_{\bar{Q}q}(t_2 - t_1) &= -\left\langle \mathrm{Tr}_{\mathrm{color,spin}} \left[\left(\gamma_0 \Gamma^\dagger \gamma_0\right) \left(\mathcal{Q}^{-1}\right)(\mathbf{r}, t_2; \mathbf{r}, t_1) \Gamma \left(\mathcal{D}^{-1}\right)(\mathbf{r}, t_2; \mathbf{r}, t_1)\right]\right\rangle \\
&= -\Bigg\langle \mathrm{Tr}_{\mathrm{color,spin}} \Bigg[\left(\gamma_0 \Gamma^\dagger \gamma_0\right) \\
&\qquad \times U(\mathbf{r}, t_2; \mathbf{r}, t_1) \left(\frac{1-\gamma_0}{2}\right) \Gamma \left(\mathcal{D}^{-1}\right)(\mathbf{r}, t_2; \mathbf{r}, t_1) \Bigg] \Bigg\rangle \mathrm{e}^{-M(t_2 - t_1)},
\end{aligned} \tag{4.8}$$

where $\mathrm{Tr}_{\mathrm{color,spin}}$ denotes the trace in color and spin space, and we used

$$\left(\Omega^{-1}(\mathbf{r},t_1;\mathbf{r},t_2)\right)^{ab}_{AB} = U^{ab}(\mathbf{r},t_1;\mathbf{r},t_2)\Bigg(\Theta(t_1-t_2)\left(\frac{1+\gamma_0}{2}\right)_{AB}\mathrm{e}^{-M(t_1-t_2)} + \Theta(t_2-t_1)\left(\frac{1-\gamma_0}{2}\right)_{AB}\mathrm{e}^{-M(t_2-t_1)}\Bigg) \tag{4.9}$$

for the static propagator, assuming $t_2 > t_1$ for the Heaviside step function $\Theta(t)$. Note that the time evolution of the static quark is essentially described by a straight path of links $U(\mathbf{r},t_1;\mathbf{r},t_2)$ from t_1 to t_2 at $\mathbf{r}$.
We also introduce a diagrammatic notation for the correlation function (4.8) as

$$\mathcal{C}^{\Gamma}_{\bar{Q}q}(t_1,t_2) = \tag{4.10}$$

where the straight line corresponds to the static quark propagator and the wiggly line corresponds to the light quark propagator. An in-depth discussion of static-light mesons can be found in [70, 71].

4.3 Static potentials

In the context of static quark systems, we define the static potential $V(r)$ as a function of the separation distance r between two static (anti)quarks. The simplest example of such a system is the well-known static quark-antiquark $\bar{Q}Q$ potential. The correlation function for this trial state is proportional to the Wilson loop

$$\begin{aligned} W_{\mu 0}(r,t) &= S_\mu(x,r)S_0(x+r\hat{\mu},t)S^\dagger_\mu(x+\hat{0},r)S^\dagger_0(x,t), \\ \text{with}\quad S_\mu(x,n) &= \Pi_{i=0}^{n-1}U_\mu(x+i\hat{\mu}). \end{aligned} \tag{4.11}$$

Note that this correlator depends solely on gauge fields and does not involve any fermion fields. Consequently, the static quark-antiquark potential can be effectively studied within pure gauge theory, i.e., lattice gauge theory with only gauge fields.

In this work, we aim to investigate states that include two light (anti)quarks in addition to the two static (anti)quarks corresponding to tetraquark systems containing two static-light mesons. For these systems, fermions contribute as valence quarks, necessitating the consideration of fermion propagators.

In the first part of this work, we will focus on the static potential of the $\bar{Q}\bar{Q}q_1q_2$ system. In the second part, we will examine the bottomonium-like $\bar{Q}Q\bar{q}_1q_2$ system, which has been studied in the context of string-breaking [72–74]. We will derive the correlation function of $\bar{Q}\bar{Q}q_1q_2$ in detail and discuss how to determine the quantum numbers of our trial states. Additionally, we will briefly outline the correlation function of $\bar{Q}Q\bar{q}_1q_2$ as a reference for the second part of this work.

4.3.1 $\bar{Q}\bar{Q}q_1q_2$

Correlation function

To investigate the $\bar{Q}\bar{Q}q_1q_2$ system, we construct a suitable creation operator,

$$\mathcal{O}^{\mp,\Gamma}_{\bar{Q}\bar{Q}q_1q_2}(\mathbf{r}_1,\mathbf{r}_2) = (\mathcal{C}\Gamma)_{AB}\left(\mathcal{C}\tilde{\Gamma}\right)_{CD}\Big(\left(\bar{Q}^a_C(\mathbf{r}_1)\,(q_1)^a_A(\mathbf{r}_1)\right)\Big(\bar{Q}^b_D(\mathbf{r}_2)\,(q_2)^b_B(\mathbf{r}_2)\Big) \mp (q_1 \leftrightarrow q_2)\Big), \tag{4.12}$$

where $\mathcal{C} = \gamma_0\gamma_2$ is the charge conjugation matrix. The $\mp$ sign distinguishes between antisymmetric and symmetric trial states, corresponding to $I = 0$ and $I = 1$ if $q_1 = u$ and $q_2 = d$.

The correlation function for this operator is given by

$$\begin{aligned}
\mathcal{C}^{\mp,\Gamma}_{\bar{Q}\bar{Q}q_1q_2}(\mathbf{r}_1,\mathbf{r}_2,t_2-t_1) =& \big\langle\Omega\big|\left(\mathcal{O}^{\mp,\Gamma}_{\bar{Q}\bar{Q}q_1q_2}(\mathbf{r}_1,\mathbf{r}_2,t_1)\right)^\dagger \mathcal{O}^{\mp,\Gamma}_{\bar{Q}\bar{Q}q_1q_2}(\mathbf{r}_1,\mathbf{r}_2,t_2)\big|\Omega\big\rangle \\
=& \Big\langle \Big(\Gamma_{AB}\tilde{\Gamma}_{CD}\bar{Q}^a_C(\mathbf{r}_1,t_1)\,(q_1)^a_A(\mathbf{r}_1,t_1)\bar{Q}^b_D(\mathbf{r}_2,t_1)\,(q_2)^b_B(\mathbf{r}_2,t_1)\Big)^\dagger \\
&\times \Gamma_{EF}\tilde{\Gamma}_{GH}\bar{Q}^c_G(\mathbf{r}_1,t_2)\,(q_1)^c_E(\mathbf{r}_1,t_2)\bar{Q}^d_H(\mathbf{r}_2,t_2)\,(q_2)^d_F(\mathbf{r}_2,t_2) \\
&- \Big(\Gamma_{AB}\tilde{\Gamma}_{CD}\bar{Q}^a_C(\mathbf{r}_1,t_1)\,(q_1)^a_A(\mathbf{r}_1,t_1)\bar{Q}^b_D(\mathbf{r}_2,t_1)\,(q_2)^b_B(\mathbf{r}_2,t_1)\Big)^\dagger \\
&\times \Gamma_{EF}\tilde{\Gamma}_{GH}\bar{Q}^c_G(\mathbf{r}_1,t_2)\,(q_2)^c_F(\mathbf{r}_1,t_2)\bar{Q}^d_H(\mathbf{r}_2,t_2)\,(q_1)^d_E(\mathbf{r}_2,t_2) \\
&\mp (q_1 \leftrightarrow q_2)\Big\rangle.
\end{aligned} \tag{4.13}$$

Using Wick's theorem, we express the correlation function (4.13) in terms of quark propagators M^{-1},

$$\left\langle\bar{\phi}_{i_1}\phi_{j_1}\cdots\bar{\phi}_{i_n}\phi_{j_n}\right\rangle = (-1)^n \sum_{P(1,2,\ldots,n)} \operatorname{sign}(P)\left(M^{-1}\right)_{i_1 j_{P_1}}\left(M^{-1}\right)_{i_2 j_{P_2}}\cdots\left(M^{-1}\right)_{i_n j_{P_n}}, \tag{4.14}$$

where ϕ represents the quark fields Q, q_1 and q_2. For $n = 4$, we consider the sum of twenty-four permutations, but most terms vanish since only quark operators with matching flavors can form a propagator. Additionally, static quarks Q can only propagate in the time direction. Consequently, each term in (4.13) contributes only once to the correlator. We obtain

$$\begin{aligned}
\mathcal{C}^{\mp,\Gamma}_{\bar{Q}\bar{Q}q_1q_2}(\mathbf{r}_1,\mathbf{r}_2,t_2-t_1) =& \Big\langle \left(\gamma_0\tilde{\Gamma}^\dagger\gamma_0\right)_{DC}\left(\gamma_0\Gamma^\dagger\gamma_0\right)_{BA}\Gamma_{EF}\tilde{\Gamma}_{GH}\Big[\\
&\operatorname{Tr}_{\text{color}}\left[\left(\mathcal{Q}^{-1}\right)_{CG}(\mathbf{r}_1,t_1;\mathbf{r}_1,t_2)\left(\mathcal{D}^{-1}_{q_1}\right)_{EA}(\mathbf{r}_1,t_2;\mathbf{r}_1,t_1)\right] \\
&\times \operatorname{Tr}_{\text{color}}\left[\left(\mathcal{Q}^{-1}\right)_{HD}(\mathbf{r}_2,t_1;\mathbf{r}_2,t_2)\left(\mathcal{D}^{-1}_{q_2}\right)_{FB}(\mathbf{r}_2,t_2;\mathbf{r}_2,t_1)\right] \\
&+ \operatorname{Tr}_{\text{color}}\Big[\left(\mathcal{Q}^{-1}\right)_{CG}(\mathbf{r}_1,t_1;\mathbf{r}_1,t_2)\left(\mathcal{D}^{-1}_{q_2}\right)_{FB}(\mathbf{r}_1,t_2;\mathbf{r}_2,t_1)
\end{aligned}$$

$$\times \left(\mathcal{Q}^{-1}\right)_{HD}(\mathbf{r}_2,t_1;\mathbf{r}_2,t_2)\left(\mathcal{D}_{q_1}^{-1}\right)_{EA}(\mathbf{r}_2,t_2;\mathbf{r}_1,t_1)\Big]$$
$$\mp (q_1 \leftrightarrow q_2)\Big]\Big\rangle. \tag{4.15}$$

Substituting the static quark propagator from (4.9), we obtain two connected and two disconnected diagrams,

$$\begin{aligned}
\mathcal{C}^{\mp,\Gamma}_{\bar{Q}\bar{Q}q_1q_2}(\mathbf{r}_1,\mathbf{r}_2,t_2-t_1) =& \mathrm{Tr}_{\mathrm{spin}}\left[\left(\gamma_0\tilde{\Gamma}^\dagger\gamma_0\right)\left(\frac{1-\gamma_0}{2}\right)\tilde{\Gamma}\left(\frac{1-\gamma_0}{2}\right)\right]\mathrm{e}^{-2M(t_2-t_1)}\\
&\times\Big\langle\left(\gamma_0\Gamma^\dagger\gamma_0\right)_{BA}\Gamma_{EF}\Big[\\
&\mathrm{Tr}_{\mathrm{color}}\left[U(\mathbf{r}_1,t_1;\mathbf{r}_1,t_2)\left(D_{q_1}^{-1}\right)_{EA}(\mathbf{r}_1,t_2;\mathbf{r}_1,t_1)\right]\\
&\times\mathrm{Tr}_{\mathrm{color}}\left[U(\mathbf{r}_2,t_1;\mathbf{r}_2,t_2)\left(D_{q_2}^{-1}\right)_{FB}(\mathbf{r}_2,t_2;\mathbf{r}_2,t_1)\right]\\
&+\mathrm{Tr}_{\mathrm{color}}\Big[U(\mathbf{r}_1,t_1;\mathbf{r}_1,t_2)\left(D_{q_2}^{-1}\right)_{FB}(\mathbf{r}_1,t_2;\mathbf{r}_2,t_1)\\
&\qquad\times U(\mathbf{r}_2,t_1;\mathbf{r}_2,t_2)\left(D_{q_1}^{-1}\right)_{EA}(\mathbf{r}_2,t_2;\mathbf{r}_1,t_1)\Big]\\
&\mp(q_1\leftrightarrow q_2)\Big\rangle
\end{aligned}$$

$\propto$ 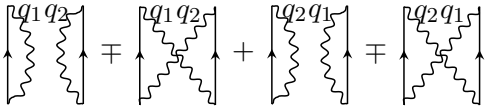 . (4.16)

Assuming isospin symmetry with $q_1 = u$ and $q_2 = d$, the correlation function reduces to two diagrams,

$\mathcal{C}^{\mp,\Gamma}_{\bar{Q}\bar{Q}ud}(\mathbf{r}_1,\mathbf{r}_2,t_2-t_1) \propto$ 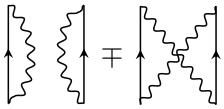 . (4.17)

In practice, it is advantageous to consider the ratio of the $\bar{Q}\bar{Q}q_1q_2$ correlator $\mathcal{C}^{\mp,\Gamma}_{\bar{Q}\bar{Q}q_1q_2}(\mathbf{r}_1,t_1|\mathbf{r}_2,t_2)$ to the static-light correlator $\mathcal{C}_{\bar{Q}q}(t_1,t_2)$,

$$\begin{aligned}
&\frac{\mathcal{C}^{\mp,\Gamma}_{\bar{Q}\bar{Q}q_1q_2}(\mathbf{r}_1,\mathbf{r}_2,t_2-t_1)}{\left(\mathcal{C}^{S}_{\bar{Q}q_1}(t_2-t_1)\right)\left(\mathcal{C}^{S}_{\bar{Q}q_2}(t_2-t_1)\right)}\\
&\qquad\xrightarrow[t\to\infty]{} A\exp\left(-\left(V^{\mp,\Gamma}_{\bar{Q}\bar{Q}q_1q_2}(\mathbf{r}_2-\mathbf{r}_1)-\left(m^{S}_{\bar{Q}q_1}+m^{S}_{\bar{Q}q_2}\right)\right)(t_2-t_1)\right),
\end{aligned} \tag{4.18}$$

where $m^S_{\bar{Q}q}$ denotes the mass of the ground state of the static-light meson with light quark q. The potential $V^{\mp,\Gamma}_{\bar{Q}\bar{Q}q_1q_2}(\mathbf{r}_2-\mathbf{r}_1)$ is by construction normalized with $m^S_{\bar{Q}q_1}+m^S_{\bar{Q}q_2}$, when

considering this ratio. Excitations may cancel each other, particularly at large distances where the $\bar{Q}\bar{Q}q_1q_2$ system is essentially two non-interacting static-light mesons.

Quantum numbers of $\bar{Q}\bar{Q}q_1q_2$ static potentials

Static $\bar{Q}\bar{Q}q_1q_2$ potentials can be classified using three quantum numbers:

- Total angular momentum along the separation axis $|j_z|$,
- Parity $\mathcal{P}$,
- Reflection symmetry along an axis perpendicular to the separation axis $\mathcal{P}_x$.

The structure of the light quarks, Γ in Eqn. (4.16), dictates the quantum numbers of the system, while the correlator remains invariant under the spin choice of the static quarks, which decouples as a constant. There are four possible choices for the spin structure of the static quarks that yield a non-zero correlation function: $(1+\gamma_0)\gamma_5$ or $(1+\gamma_0)\gamma_j$ with j = 1,2,3, all of which produce the same correlators. However, considering symmetry transformations, such as parity or rotations in spin space (corresponding to the angular momentum quantum number), of the operator in Eqn. (4.12), the heavy quark structure also contributes, albeit equivalently to each sector. We choose $\tilde{\Gamma} = (1+\gamma_0)\gamma_5$, with which the static quarks carry zero angular momentum and even $\mathcal{P}$ and $\mathcal{P}_x$. Thus, it is sufficient to consider the light quark spin structure, which immediately yields the quantum numbers of the system.

We can write down the light quark part of the operator from Eqn. (4.12) as

$$\left(\mathcal{O}^{\Gamma}_{q_1q_2}(r)\right)^{ab} = \left(q_1^a(-r)\right)^T \mathcal{C}\Gamma q_2^b(r) \mp (q_1 \leftrightarrow q_2), \tag{4.19}$$

where we assumed $\mathbf{r_1} = (0,0,-r)$ and $\mathbf{r_2} = (0,0,r)$. Note that this partial operator carries two open color indices, a and b, which are contracted with the static quark part of the full operator. To illustrate how to obtain the quantum numbers for a spin structure Γ, we will derive $|j_z|$, $\mathcal{P}$, and $\mathcal{P}_x$ for an exemplary light quark spin $\Gamma = \gamma_5$.

The angular momentum can be determined by using the rotation operator around the separation axis (w.l.o.g. z-axis) $\hat{R}_3(\alpha)$, which in spin space can be represented as a function of the γ-matrices via

$$\mathcal{R}_3(\alpha)(\psi(r)) = \exp\left(\frac{1}{2}\alpha\left[\gamma_1,\gamma_2\right]\right)\psi(r) = \left(1+\frac{1}{2}\alpha\left[\gamma_1,\gamma_2\right]+\mathcal{O}(\alpha^2)\right)\psi(r). \tag{4.20}$$

Applying this to $\mathcal{O}^{\gamma_5}_{q_1q_2}(r)$ yields

$$\begin{aligned}
\hat{R}_3(\alpha)\left(\mathcal{O}^{\gamma_5}_{q_1q_2}(r)\right)^{ab}\hat{R}_3^{\dagger}(\alpha) &= \left(q_1^a(-r)\right)^T\left(1+\frac{1}{2}\alpha\left[\gamma_1,\gamma_2\right]+\mathcal{O}(\alpha^2)\right)^T \\
&\quad\times\gamma_0\gamma_2\gamma_5\left(1+\frac{1}{2}\alpha\left[\gamma_1,\gamma_2\right]+\mathcal{O}(\alpha^2)\right)q_2^b(r) \mp (q_1\leftrightarrow q_2) \\
&= \left(q_1^a(-r)\right)^T\gamma_0\gamma_2\gamma_5 q_2^b(r) + \mathcal{O}(\alpha^2) \mp (q_1\leftrightarrow q_2) \\
&= \left(\mathcal{O}^{\gamma_5}_{q_1q_2}(r)\right)^{ab} + \mathcal{O}(\alpha^2),
\end{aligned} \tag{4.21}$$

which corresponds to angular momentum $J_3 = |j_z| = 0$, when comparing with $\mathcal{R}_3(\alpha)(\psi(r)) = (1 + i\alpha J_3 + \mathcal{O}(\alpha^2))\psi(r)$.

The parity transformation $\hat{P}$ in spin space is realized by $\mathcal{P}\psi(r) = \gamma_0\,\psi(-r)$, thus the trial state transforms according to

$$\begin{aligned}
\hat{P}\left(\mathcal{O}^{\gamma_5}_{q_1q_2}(r)\right)^{ab}\hat{P}^\dagger &= (q_1^a(+r))^T\ \gamma_0\gamma_0\gamma_2\gamma_5\gamma_0\ q_2^b(-r) \mp (u \leftrightarrow d) \\
&= -(q_2^b(-r))^T\ \gamma_0\gamma_5\gamma_2\ q_1^a(+r) \mp (u \leftrightarrow d) \\
&= (q_2^b(-r))^T\ \mathcal{C}\gamma_5\ q_1^a(+r) \mp (u \leftrightarrow d) \\
&= \mp\ \left(\mathcal{O}^{\gamma_5}_{q_1q_2}(r)\right)^{ba},
\end{aligned} \tag{4.22}$$

where in step two the nature of Grassmann numbers was used. The color indices a and b switch in comparison to the initial operator, which is compensated by a switch of the same color indices in the static quark part of the operator when applying this transformation. Thus, this results in negative parity $\mathcal{P} = -$ for antisymmetric flavor content (corresponding to $I = 0$ for $q_1 = u$ and $q_2 = d$) and $\mathcal{P} = +$ for symmetric flavor content (corresponding to $I = 1$ for $q_1 = u$ and $q_2 = d$).

The reflection along a perpendicular axis to the separation axis $\hat{P}_x$ can be realized by rotating around this axis, w.l.o.g. the x-axis, using the rotation operator $\mathcal{R}_1(\alpha)(\psi(r))$ and applying parity transformation $\hat{P}$ afterwards,

$$\begin{aligned}
\hat{P}_x\left(\mathcal{O}^{\gamma_5}_{q_1q_2}(r)\right)^{ab}\hat{P}_x &= \hat{P}\hat{R}_1(\alpha)\mathcal{O}^{\gamma_5}_{q_1q_2}(r)\hat{R}_1^\dagger(\alpha)\hat{P}^\dagger \\
&= u^T(-r)\left(1 + \frac{1}{2}\alpha\,[\gamma_2,\gamma_3] + \mathcal{O}(\alpha^2)\right)^T \\
&\qquad \gamma_0\gamma_0\gamma_2\gamma_5\gamma_0\left(1 + \frac{1}{2}\alpha\,[\gamma_2,\gamma_3] + \mathcal{O}(\alpha^2)\right) d(r) \mp (u \leftrightarrow d) \\
&= u^T(-r)\gamma_0\gamma_2\gamma_5 d(r) + \mathcal{O}(\alpha^2) \mp (u \leftrightarrow d), \\
&= +\left(\mathcal{O}^{\gamma_5}_{q_1q_2}(r)\right)^{ab},
\end{aligned} \tag{4.23}$$

i.e. $\mathcal{P}_x = +$.

The symmetries derived in this chapter all refer to the continuum. The $\mathcal{P}$ and $\mathcal{P}_x$ symmetries are discrete and transfer trivially to the lattice. The rotational symmetry corresponding to the quantum number $|j_z|$, however, is a continuum symmetry, which breaks down into subgroups on the lattice. The following section is dedicated to discussing this topic.

Angular momentum $|L|$ and rotational symmetry on the lattice

When computing the potential between two static quarks, the quark positions define a separation distance. On a lattice, a natural choice is to place both quarks along one coordinate axis. For instance, if the first quark is at the spatial position (0,0,0), the second quark can be placed at (r,0,0), (0,r,0), or (0,0,r), creating a pair with separation distance r. These are referred to as "on-axis" separations. It is also possible to place quarks in more complex relative positions, referred to as "off-axis" separations.

In the continuum, the system of static quarks is characterized by cylindrical symmetry around the separation axis of the quarks, denoted as $D_{\infty h}$. The D indicates cylindrical symmetry and ∞h signifies an infinite number of possible rotations around this axis. This rotation group is directly related to the angular momenta of the state. The $D_{\infty h}$ symmetry in the continuum allows for an infinite number of angular momentum representations ($L = 0, \pm 1, \pm 2, \ldots$).

On a discretized lattice, this symmetry breaks down to a subgroup. For on-axis separations, there are only four possible rotations around the axis, resulting in a D_{4h} symmetry. This reduction means it is impossible to distinguish an infinite number of angular momenta, leading to the mixing of continuum representations.

To investigate this mixing, we first construct a generic trial state $|H\rangle$ with defined angular momentum L, which in the continuum can be written as

$$|H\rangle = \int_0^{2\pi} \mathrm{d}\phi \exp(iL\phi)\mathcal{O}(\phi)\,|\Omega\rangle\,, \tag{4.24}$$

where $\mathcal{O}(\phi)$ is an operator depending on the angle ϕ with respect to the separation axis. On the lattice, the integral becomes a sum over the possible rotations n,

$$|H\rangle = \sum_{k=0}^{n} \exp(2iLk\pi/n)\mathcal{O}(2\pi k/n)\,|\Omega\rangle\,. \tag{4.25}$$

For on-axis separations, the remaining symmetry is D_{4h}, corresponding to $n = 4$ possible rotations by 0°, 90°, 180°, and 270°. We define a rotation $R_{|L|}(\phi)$ with respect to the absolute value of the angular momentum $|L|$ according to

$$R_{|L|}(\phi) = \frac{1}{2}\left(\exp(2iL\phi) + \exp(-2iL\phi)\right), \tag{4.26}$$

and rewrite Eqn. (4.25) to obtain

$$|H\rangle = \sum_{k=0}^{n} R_{|L|}(2\pi k/n)\mathcal{O}(2\pi k/n)\,|\Omega\rangle\,. \tag{4.27}$$

We can identify which continuum representations mix by investigating $R_{|L|}(0°)$, $R_{|L|}(90°)$, $R_{|L|}(180°)$, and $R_{|L|}(270°)$. Their values are collected in the first row of Tab. 4.1, showing that angular momenta $|L| = 0,4,8,\ldots$, $|L| = 1,3,5,\ldots$, and $|L| = 2,6,10,\ldots$ produce the same $R_{|L|}(\phi)$. This implies that only three different angular momentum representations can be constructed, and a trial state will always mix an infinite number of angular momenta within each representation. However, the lowest energy eigenstate in a given state typically corresponds to the lowest angular momentum in this representation. Consequently, studying the ground states for angular momenta $|L| = 0,1,2$ for on-axis separations is generally straightforward.

The relative position of the quarks can also be more complex. For instance, if the first quark is at (0,0,0), the second quark can be positioned at (a,b,c) where at least two out of

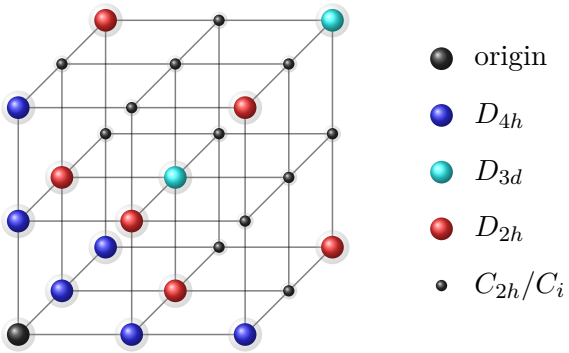

Figure 4.1: On- and off-axis separations and corresponding symmetry groups.

Table 4.1: Remaining symmetries on the lattice for different separation axes. The first column displays the separation axis of the static anti-quark pair with numbers a, b, and c different from each other and 0. The fourth column shows which angular momenta mix. The last four columns show how these angular momenta are realized on the lattice in terms of the eigenvalues of the rotation operator $R_{|L|}(\theta)$ from Eqn. (4.26) with $\theta \in \{k \cdot 2\pi/n\}$ with $k < n, k \in \mathbb{N}_0$ acting on a trial state.

Axis	Symmetry group	n	$\lvert L\rvert$	$R_{\lvert L\rvert}(0)$	$R_{\lvert L\rvert}(\pi/2)$	$R_{\lvert L\rvert}(\pi)$	$R_{\lvert L\rvert}(3\pi/2)$
(0,0,a)	D_{4h}	4	0,4,8,...	1	1	1	1
			1,3,5,...	1	0	-1	0
			2,6,10,...	1	-1	1	-1
				$R_{\lvert L\rvert}(0)$	$R_{\lvert L\rvert}(\pi/3)$	$R_{\lvert L\rvert}(2\pi/3)$	
(a,a,a)	D_{3d}	3	0,3,6,...	1	1	1	
			1,2,4,...	1	± 1	-1	
				$R_{\lvert L\rvert}(0)$	$R_{\lvert L\rvert}(\pi)$		
(0,a,a)	D_{2h}	2	0,2,4,...	1	1		
			1,3,5,...	1	-1		
				$R_{\lvert L\rvert}(0)$			
(0,a,b)	C_{2h}	1	0,1,2,...	1			
(a,a,b)	C_{2h}						
(a,b,c)	C_i						

a,b,c are non-zero. The separation distance of the quarks is $r = \sqrt{a^2 + b^2 + c^2}$, referred to as an "off-axis" separation.

The symmetry also changes for these separations, as rotations by 90° are no longer possible. We distinguish three relative positions for the second quark:

- On the space diagonal, parametrized by (a, a, a). The remaining symmetry is D_{3d}, i.e., $n = 3$ possible rotations by 0°, 120°, 240°.
- On the plane diagonal, parametrized by $(a, a, 0)$ and permutations. The remaining symmetry is D_{2h}, i.e., $n = 2$ possible rotations by 0°, 180°.
- In a different position, parametrized by $(0, a, b)$, (a, a, b), or (a, b, c) and permutations.

The remaining group is C_{2h}, C_{2h}, or C_i, respectively, with only $n = 1$ rotation by 0° possible.

Fig. 4.1 illustrates these relative quark positions on the lattice and the corresponding symmetry groups. Each symmetry group's properties and angular momenta mixing are summarized in Tab. 4.1. Generally, the mixing of angular momenta due to the rotation group becomes more problematic with off-axis separations.

Assuming the typical case where the lowest energy state has $|L| = 0$ and larger angular momentum states have higher energy, the ground state can still be extracted for all off-axis separations but may suffer from more contamination by higher angular momentum states. However, studying $|L| = 1$ states becomes impossible for off-axis separations with symmetries C_{2h} or C_i, as there is overlap with a lower energy state with $|L| = 0$, and the trial state will ultimately probe the lower-lying state instead. Thus, in this case, it is recommended to include only off-axis separations with symmetry groups D_{2h} and D_{3d}. Other off-axis separations could still be included when the ground and excited states are rigorously separated by considering correlation matrices [67].

Shapes of $\bar{Q}\bar{Q}q_1q_2$ potentials

We can phenomenologically deduce the shape of possible potentials depending on their quantum numbers. We expect that at large separations, the potential will asymptotically approach the mass of two static light mesons. There are three possible asymptotic values, which correspond to the combination of two static-light mesons with either parity $-$ (S) or parity $+$ (P_-).

Furthermore, at small distances we expect the dominant effect to be one-gluon exchange, which can either be attractive or repulsive. A simple rule to determine whether a potential for a given operator will be attractive or repulsive is introduced in [30]. It states that if the trial state is symmetric/antisymmetric under meson exchange, i.e., under combined exchange of flavor, spin, and parity, the resulting potential is attractive/repulsive.

This can be understood by investigating the symmetry of the wave functions. When we consider the one-gluon exchange of the heavy pair of antiquarks $\bar{Q}\bar{Q}$ at small separations, the potential is Coulomb-like, i.e., $V(r) \propto g^2/r$ with the coupling g and separation distance r. The $\bar{Q}\bar{Q}$ can be either in a color triplet representation $\mathbf{3}$ or anticolor sextet representation $\bar{\mathbf{6}}$, which has respectively a positive ($\mathbf{3}$) or negative ($\bar{\mathbf{6}}$) proportionality constant, due to the Casimir scaling, which corresponds to an attractive potential for the color triplet $\mathbf{3}$ and a repulsive potential for the anticolor sextet $\bar{\mathbf{6}}$. To produce a colorless state, the light quarks have to be in the antisymmetric color anti-triplet $\bar{\mathbf{3}}$ if the static quarks are in the $\mathbf{3}$ representation and in a symmetric color sextet $\mathbf{6}$ if the static quarks are in the $\bar{\mathbf{6}}$ representation. To ensure the antisymmetry of the light quarks, the combined symmetry with respect to the exchange of flavor, spin, and parity of the light quarks then has to be symmetric for the color anti-triplet $\bar{\mathbf{3}}$, leading to an attractive potential and antisymmetric for the anticolor sextet $\bar{\mathbf{6}}$, leading to a repulsive potential.

There are six qualitatively different shapes for the resulting potentials, as they can be either attractive (A) or repulsive (R) and have three possible asymptotic values SS ($m^S_{\bar{Q}q_1} + m^S_{\bar{Q}q_2}$), SP ($m^S_{\bar{Q}q_1} + m^{P_-}_{\bar{Q}q_2}$) and PP ($m^{P_-}_{\bar{Q}q_1} + m^{P_-}_{\bar{Q}q_2}$). In Tab. 4.2, we summarize a

Table 4.2: Quantum numbers and properties of the resulting $\bar{Q}\bar{Q}q_1q_2$ potentials: A = attractive, R = repulsive; SS, SP ,PP = asymptotic value $m^S_{\bar{Q}q_1} + m^S_{\bar{Q}q_2}$, $m^S_{\bar{Q}q_1} + m^{P_-}_{\bar{Q}q_2}$, $m^{P_-}_{\bar{Q}q_1} + m^{P_-}_{\bar{Q}q_2}$.

	$q_1q_2 - q_2q_1$			$q_1q_2 + q_2q_1$		
Γ	$\lvert j_z\rvert$	$\mathcal{P}$,$\mathcal{P}_x$	shape	$\lvert j_z\rvert$	$\mathcal{P}$,$\mathcal{P}_x$	shape
$\gamma_5 + \gamma_0\gamma_5$	0	−,+	A,SS	0	+,+	R,SS
1	0	+,−	A,SP	0	−,−	R,SP
γ_0	0	−,−	R,SP	0	+,−	A,SP
$\gamma_5 - \gamma_0\gamma_5$	0	−,+	A,PP	0	+,+	R,PP
$\gamma_3 + \gamma_0\gamma_3$	0	+,−	R,SS	0	−,−	A,SS
$\gamma_3\gamma_5$	0	+,+	A,SP	0	−,+	R,SP
$\gamma_0\gamma_3\gamma_5$	0	−,+	R,SP	0	+,+	A,SP
$\gamma_3 - \gamma_0\gamma_3$	0	+,−	R,PP	0	−,−	A,PP
$\gamma_{1/2} + \gamma_0\gamma_{1/2}$	1	+, + /−	R,SS	1	−, + /−	A,SS
$\gamma_{1/2}\gamma_5$	1	+, − /+	A,SP	1	−, − /+	R,SP
$\gamma_0\gamma_{1/2}\gamma_5$	1	−, − /+	R,SP	1	+, − /+	A,SP
$\gamma_{1/2} - \gamma_0\gamma_{1/2}$	1	+, + /−	R,PP	1	−, + /−	A,PP

complete set of sixteen Γ operators and the corresponding quantum numbers and potential shapes for $I = 0$ and $I = 1$. Note that the operators containing γ_1/γ_2 are degenerate due to symmetry, as they correspond to the two axes perpendicular to the separation axis. Typically, this degeneracy is used to combine results and increase statistics.

4.3.2 $\bar{Q}Q\bar{q}q$

Correlation function

The $\bar{Q}Q\bar{q}q$ system is more intricate, as generally more channels contribute. Specifically, $\bar{Q}Q\bar{q}q$ states can receive contributions from conventional quarkonium $\bar{Q}Q$. Consequently, at a minimum, one must consider both a quarkonium operator $\mathcal{O}_{\bar{Q}Q}$ and a $\bar{Q}Q\bar{l}l$ operator $\mathcal{O}_{\bar{Q}Q\bar{l}l}$ to study this tetraquark system adequately, where $\bar{l}l = \bar{u}u + \bar{d}d$ is the $I = 0$ combination of u/d light quarks. The correlation matrix can then be expressed as

$$
\begin{aligned}
&\mathcal{C}_{\bar{Q}Q\bar{l}l}(\mathbf{r}_1, t_1 | \mathbf{r}_2, t_2) \\
&= \begin{pmatrix}
\left\langle \mathcal{O}_{\bar{Q}Q}(\mathbf{r}_1, \mathbf{r}_2, t_1) \,\middle|\, \mathcal{O}_{\bar{Q}Q}(\mathbf{r}_1, \mathbf{r}_2, t_2) \right\rangle & \left\langle \mathcal{O}_{\bar{Q}Q\bar{l}l}(\mathbf{r}_1, \mathbf{r}_2, t_1) \,\middle|\, \mathcal{O}_{\bar{Q}Q}(\mathbf{r}_1, \mathbf{r}_2, t_2) \right\rangle \\
\left\langle \mathcal{O}_{\bar{Q}Q}(\mathbf{r}_1, \mathbf{r}_2, t_1) \,\middle|\, \mathcal{O}_{\bar{Q}Q\bar{l}l}(\mathbf{r}_1, \mathbf{r}_2, t_2) \right\rangle & \left\langle \mathcal{O}_{\bar{Q}Q\bar{l}l}(\mathbf{r}_1, \mathbf{r}_2, t_1) \,\middle|\, \mathcal{O}_{\bar{Q}Q\bar{l}l}(\mathbf{r}_1, \mathbf{r}_2, t_2) \right\rangle
\end{pmatrix} \\
&= \left(\quad \right), \qquad (4.28)
\end{aligned}
$$

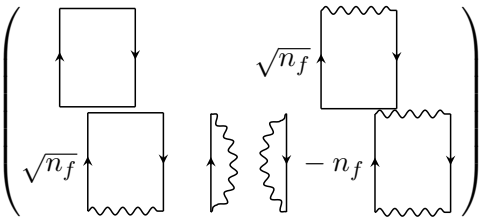

where n_f denotes the number of degenerate light flavors, e.g., $n_f = 2$ for degenerate u and d quarks. This correlation matrix is derived and discussed in detail in [72]. Note that the upper left element of the correlation matrix corresponds to the conventional Wilson loop, while the remaining elements also incorporate light quark propagators.

This correlation matrix can be straightforwardly expanded to include additional channels. For instance, in [73] and [74], the correlation matrix is extended by introducing a third channel that includes light strange quarks via a $\bar{Q}Q\bar{s}s$ operator.

Quantum numbers of $\bar{Q}Q\bar{q}q$ static potentials

Static quark-antiquark potentials are typically characterized by the following three quantum numbers, denoted as Λ_η^ε:

- $\Lambda = \Sigma, \Pi, \Delta, \ldots \Leftrightarrow |L| = 0, 1, 2, \ldots$: Total angular momentum with respect to the separation axis of the antiquarks.
- $\eta = g, u \Leftrightarrow \mathcal{P} \circ \mathcal{C} = +, -$: Behavior under parity $\mathcal{P}$ and charge conjugation $\mathcal{C}$.
- $\varepsilon = +, - \Leftrightarrow \mathcal{P}_x = +, -$: Behavior under reflection along an axis perpendicular to the separation axis.

If the system contains u and d quarks, isospin I is also a quantum number.

4.4 Fermion propagator computation

While computing gauge-like observables on the lattice is relatively straightforward by multiplying elements of the $SU(3)$ groups connecting the lattice points, e.g., as in Eqn. (4.11), computing fermionic structures is generally more complex. The quark propagator $\mathcal{D}^{-1}$ is given by the inverse of the Dirac operator $\mathcal{D}$. Naively inverting this operator would lead to $3 \times 4 \times L^3 \times T$ equations of the form

$$D^{ab}_{AB}(x; y) G^{bc}_{BC}(y; z) = \delta(x - z)\delta_{AC}\delta_{ac}. \tag{4.29}$$

For typical lattice sizes of around $L = T/2 = 32$, we would need to solve over ten million equations, making the numerical solution of this equation infeasible. Additionally, the entries of this full propagator would be highly correlated on a given gauge configuration. For these reasons, one computes estimates of this propagator instead. This estimation always revolves around solving the system of equations

$$\mathcal{D}^{ab}_{AB}(y; x)\phi^b_B(x) = \eta^a_A(y) \tag{4.30}$$

with source field $\eta^a_A(y)$ and sink field $\phi^b_B(x)$, which is usually referred to as the "propagator". The source field $\eta^a_A(y)$ is usually given, and $\phi^b_B(x)$ is determined by inverting the Dirac operator $\mathcal{D}^{ab}_{AB}(y; x)$ with respect to $\eta^a_A(y)$. We will briefly discuss the most straightforward method, computing one column of this propagator, referred to as the point-to-all propagator. Then, we will explain in detail the stochastic propagator used for computations in this work.

4.4.1 Point-to-all propagator

QCD is invariant under spatial translation, and thus, it is often sufficient to consider the propagation from one point to all other points. This leads to the system of equations

$$\mathcal{D}^{ab}_{AB}(y;x)\phi^b_B(x)[C,c,z] = \eta^a_A(y)[C,c,z] \quad \text{with} \quad \eta^a_A(y)[C,c,z] = \delta(x,y)\delta_{AC}\delta_{ac}, \tag{4.31}$$

which has to be solved twelve times, i.e., for each combination of color and spin indices, to obtain one column in position space of the full propagator. The cornered brackets indicate the indices in color, spin, and position space of the non-zero component of the point source. This results in the twelve solutions $\phi^b_B(x)[C,c,z]$, which are the point-to-all propagators, i.e.,

$$\phi^a_A(x)[B,b,y] = \left(\mathcal{D}^{-1}\right)^{ab}_{AB}(x;y). \tag{4.32}$$

This method is particularly suited for correlators where all propagators start at the same spacetime point and thus can be expressed by the point-to-all propagator straightforwardly. However, this is not the case for multi-particle systems; therefore, more sophisticated methods are needed.

4.4.2 Stochastic timeslice-to-all propagators

There are also stochastic methods to estimate the quark propagator numerically. A prevalent method is stochastic timeslice-to-all propagators. This means a random source propagating to any spatial point on a given timeslice to all spacetime points of the lattice. We define N stochastic timeslice-sources according to

$$\eta^a_A(t,\mathbf{x})[t_0,n] = \delta_{tt_0}\zeta^a_A(\mathbf{x})[n], \tag{4.33}$$

where $\zeta^a_A(\mathbf{x})[n]$ are uniformly distributed random numbers that satisfy

$$\frac{1}{N}\sum_{n=1}^{N}\left(\zeta^a_A(\mathbf{x})[n]\right)^*\zeta^b_B(\mathbf{y})[n] = \delta(\mathbf{x},\mathbf{y})\delta_{AC}\delta_{ac} + \mathcal{O}(N^{-\alpha}), \tag{4.34}$$

where $\mathcal{O}(N^{-\alpha})$ indicates an unbiased noise created by the random variables. A common and straightforward choice is $\zeta^a_A(\mathbf{x})[n] \in \{(\pm 1 \pm i)/\sqrt{2}\}$, which creates an unbiased noise of $\mathcal{O}(1/\sqrt{2})$, i.e., $\alpha = 1/2$. This yields the system of linear equations

$$\mathcal{D}^{ab}_{AB}(t_2,\mathbf{y};t_1,\mathbf{x})\phi^b_B(t_1,\mathbf{x})[t_0,n] = \eta^a_A(t_2,\mathbf{y})[t_0,n]. \tag{4.35}$$

The propagator can then be estimated as

$$\begin{aligned}\frac{1}{N}\sum_{n=1}^{N}&\phi^a_A(t_1,\mathbf{x})[t_0,n]\left(\eta^b_B(t_2,\mathbf{y})[t_0,n]\right)^\dagger \\ &= \left(\mathcal{D}^{-1}\right)^{ac}_{AC}(x;z)\frac{1}{N}\sum_{n=1}^{N}\eta^c_C(t_2,\mathbf{z})[t_0,n]\left(\eta^b_B(t_2,\mathbf{y})[t_0,n]\right)^\dagger\end{aligned}$$

$$= \left(\mathcal{D}^{-1}\right)^{ab}_{AB}(x;\mathbf{y},t_0) + \sum_{c,C,\mathbf{z}} \left(\mathcal{D}^{-1}\right)^{ac}_{AC}(x;\mathbf{z},t_0)\mathcal{O}(N^{-\alpha}), \tag{4.36}$$

where we used Eqn. (4.34) in the second step and $\mathcal{O}(N^{-\alpha})$ corresponds to the unbiased noise created by the random variables.

Because of the additional noise introduced to the system, stochastic propagators must be used carefully. The number of noise sources should be kept small enough to minimize stochastic noise, but at the same time, more sources can also increase statistics. At a minimum, the number of stochastic sources must be larger than the number of propagators in the operator.

4.5 Smearing techniques

To ensure that the trial states created by the operators have a significant overlap with the ground state, it is crucial to employ smearing techniques. The large overlap allows for extracting effective masses or potentials at relatively small time separations, where the signal-to-noise ratio remains favorable. Smearing enhances the overlap by replacing the quark fields with a linear combination of the original fields and their neighbors. This process is iterative, and the number of smearing steps and parameters must be optimized. Spatial smearing effectively extends the fields, increasing their overlap with the ground state. However, smearing of the time links must be performed cautiously as it alters the action. The following sections discuss the smearing techniques utilized in this work.

4.5.1 APE-smearing of gauge links

APE smearing [75] replaces the original gauge links $U_j(x)$ with a linear combination of the original link and its staples (see Fig. 4.2, left). The staples are the links connected to the original link by a path of length one. The APE-smearing is defined by the iterative equation

$$\begin{aligned} U_j^{N_{\mathrm{APE}}}(x) = P_{\mathrm{SU(3)}}\Bigg(& U_j^{N_{\mathrm{APE}}-1}(x) \\ & + \alpha_{\mathrm{APE}} \sum_{k=\pm1,\pm2,\pm3}^{k\neq\pm j} \left(U_k^{N_{\mathrm{APE}}-1}(x) U_j^{N_{\mathrm{APE}}-1}(x+\hat{k}) U_k^{N_{\mathrm{APE}}-1\dagger}(x+\hat{j}) \right) \Bigg), \end{aligned} \tag{4.37}$$

where $P_{\mathrm{SU(3)}}$ denotes the projection of the link back to the SU(3) group. The parameter α_{APE} and the number of smearing steps must be optimized. Typical parameters are $\alpha_{\mathrm{APE}} = 0.5$, and the number of smearing steps ranging from $N_{\mathrm{APE}} = 10$ to $N_{\mathrm{APE}} = 50$, depending on the lattice spacing a.

4.5.2 Gaussian smearing of source and sink

Gaussian smearing [76] replaces the original quark fields with a linear combination of the original field and its neighbors. This iterative process requires optimization of the number

of smearing steps and parameters. The smearing is defined by the iterative equation

$$\psi^{N_{\text{Gauss}}}(x) = \frac{1}{1+6\kappa}\Bigg(\psi^{N_{\text{Gauss}}-1}(x) + \\ + \kappa \sum_{k=\pm1,\pm2,\pm3} \Big(U_k(x)\psi^{N_{\text{Gauss}}-1}(x+\hat{k})\Big)\Bigg), \tag{4.38}$$

where κ is the smearing parameter and N_{Gauss} is the number of smearing steps. The width of the Gaussian smearing can be controlled by the number of smearing steps and the smearing parameter, approximated by

$$\sigma \approx \sqrt{\frac{2N_{\text{Gauss}}\kappa}{1+6\kappa}}. \tag{4.39}$$

Typical parameters are $\kappa = 0.5$, and the number of smearing steps ranging from $N_{\text{Gauss}} = 10$ to $N_{\text{Gauss}} = 120$, depending on the lattice spacing a. Eqn. (4.39) can be used to tune the number of smearing steps, ensuring that the smearing width remains constant across different lattice spacings a.

4.5.3 HYP static action

The HYP static action, also known as hypercubic blocking, extends the thin link in the time direction to a hypercubic block through multiple APE-like blocking steps (see Fig. 4.2(b), right). This involves three steps of APE-smearing, each followed by a projection back to the SU(3) group,

$$\begin{aligned} U_\mu^{HYP}(x) &= P_{\text{SU(3)}}\left[(1-\alpha_1)\,U_\mu(x) + \frac{\alpha_1}{6}\sum_{\pm\nu\neq\mu} V_{\nu;\mu}(x)V_{\nu;\mu}(x+\hat{\nu})V^\dagger_{\nu;\mu}(x+\hat{\mu})\right], \\ V_{\mu,\nu}(x) &= P_{\text{SU(3)}}\left[(1-\alpha_2)\,U_\mu(x) + \frac{\alpha_2}{4}\sum_{\pm\rho\neq\nu\mu} W_{\rho;\nu\mu}(x)W_{\mu;\rho\nu}(x+\hat{\rho})W^\dagger_{\rho;\nu\mu}(x+\hat{\mu})\right], \\ W_{\mu,\nu}(x) &= P_{\text{SU(3)}}\left[(1-\alpha_3)\,U_\mu(x) + \frac{\alpha_3}{2}\sum_{\pm\eta\neq\rho\nu\mu} U_\eta(x)U_\mu(x+\hat{\eta})U^\dagger_\eta(x+\hat{\mu})\right], \end{aligned} \tag{4.40}$$

where α_1, α_2, and α_3 are the smearing parameters. Common parameter choices are $\alpha_1 = 0.75$, $\alpha_2 = 0.6$, $\alpha_3 = 0.3$ for the HYP static action, and $\alpha_1 = 1$, $\alpha_2 = 1$, $\alpha_3 = 0.5$ for the HYP2 static action. Typically, only one smearing step ($N_{\text{HYP}} = 1$) is performed. Note that HYP smearing of the time links also changes the gauge action to the HYP static action.

4.5.4 Projection to SU(3)

The smearing algorithms for gauge links typically involve the addition of two SU(3) matrices, which does not yield an SU(3) matrix as a result. Since the links must be elements of the gauge group SU(3), the resulting matrices must be projected back to SU(3), as indicated in

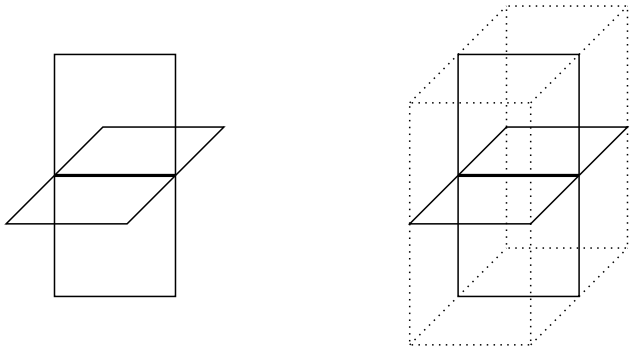

Figure 4.2: Left: Illustration of APE smearing where the thick line in the center is the original link, while other lines indicate path of links that are summed over to create the smeared link. Right: Illustration of HYP smearing indicating, that multiple levels of smearing are performed, contained within a hypercube.

Eqns. (4.37) and (4.40) by $P_{\mathrm{SU}(3)}$. There are multiple methods to achieve this projection.

An exact projection [72] to SU(3) is given by

$$P_{\mathrm{SU}(3)}(U) = \frac{U'}{\det(U')^{\frac{1}{3}}} \quad \text{with} \quad U' = U\left(U^\dagger U\right)^{-\frac{1}{2}} \in \mathrm{U}(3). \tag{4.41}$$

The inverse square root of $U^\dagger U$ is calculated in its eigenbasis, considering the positive root of the respective eigenvalues. For the third root of the determinant $\det(U')^{\frac{1}{3}}$, the root closest to unity is chosen. This construction ensures unitarity and gauge covariance.

An alternative iterative method [77] involves the steps

$$U \to U/\sqrt{\mathrm{Tr}\left(UU^\dagger\right)/3}, \tag{4.42}$$

followed by N_{proj} iterations of

$$U \to X\left(1 - \frac{i}{3}\mathrm{Im}\left(\det X\right)\right) \quad \text{with} \quad X = U\left(\frac{3}{2} - \frac{1}{2}U^\dagger U\right). \tag{4.43}$$

This projection is more efficient if only a few iterations N_{proj} are needed, i.e., the gauge link U is already close to SU(3), or the observable is relatively insensitive to deviations from unitarity. Generally, the exact projection from Eqn. (4.41) is recommended.

4.6 Tree-level improvement

Tree-level improvement [78] is a technique to mitigate systematic discretization errors at short distances. This method matches the continuum potential at tree level of perturbation theory,

$$V^0_{\mathrm{cont}} \propto \left(\frac{1}{r}\right)_{\mathrm{cont}} \tag{4.44}$$

with its lattice counterpart,

$$V_{\text{lat}}^{0} \propto \left(\frac{1}{r}\right)_{\text{lat}} = \frac{4\pi}{a} G\left(\mathbf{r}/a\right). \tag{4.45}$$

where $G\left(\mathbf{r}/a\right)$ represents the lattice propagator at tree level, dependent on the discretization of the static action. For the Wilson plaquette gauge action introduced in Eqn. (3.7), it is given by

$$G\left(\mathbf{r}/a\right) = \frac{1}{a}\int_{-\pi}^{\pi} \frac{\mathrm{d}^3 k}{(2\pi)^3} \frac{\Pi_{j=1}^{3} \cos\left(r_j k_j/a\right)}{4\sum_{j=1}^{3} \sin^2\left(k_j/2\right)}. \tag{4.46}$$

Upon applying HYP smearing to the time-links, the gauge action changes to the HYP static action, which has a more intricate lattice propagator [79],

$$G_{\text{HYP}}(\mathbf{r}/a) = \frac{1}{(2\pi)^3}\int_{-\pi}^{\pi} \frac{\Pi_{j=1}^{3} \cos\left(r_j p_j/a\right)\left(1-(2\alpha_1/3)\,\Sigma_{i=1}^{3}\sin^2\left(p_i\right)\Omega_{i0}(p)\right)^2}{4\sum_{j=1}^{3}\sin^2\left(p_j/2\right)}\mathrm{d}^3 p \tag{4.47}$$

with

$$\Omega_{\mu\nu} = 1+\alpha_2\left(1+\alpha_3\right)-\alpha_2\left(1+2\alpha_3\right)\left(\sum_{j=1}^{3}\sin^2(p_j/2)-\sin^2(p_\mu/2)-\sin^2(p_\nu/2)\right) + \alpha_2\alpha_3\Pi_{\eta\neq\mu,\nu}\sin^2(p_\eta/2). \tag{4.48}$$

Using Eqns. (4.44) and (4.45), we can define an improved separation as

$$\frac{1}{4\pi r_{\text{impr}}} = \frac{G\left(\mathbf{r}/a\right)}{a}. \tag{4.49}$$

This improvement can be applied to any static potential involving the gluon propagator as the tree-level diagram. An even more advanced method of tree-level improvement, applicable to pure gauge static $\bar{Q}Q$ potentials, is known as the V-method [79–81].

CHAPTER 5

Lattice QCD results for anti-static-anti-static-light-light tetraquark potentials

In this section, we present the results of a lattice QCD computation of the static $\bar{Q}\bar{Q}q_1q_2$ potential by evaluating the correlation function derived in Sec. 4.3.1.

We begin by outlining the parameters of the three lattice ensembles of our computation. Subsequently, we discuss the static-light meson mass computed on these ensembles, which is closely related to the tetraquark system. We then present the results for $\bar{Q}\bar{Q}ud$ potentials, providing a detailed analysis of the effective masses and investigating the effects of different symmetries regarding off-axis separations. Following this, we present results for the $\bar{Q}\bar{Q}us$ system and finally compute the binding energy for the $I(J^P) = 0(1^+)$ tetraquark system using the Born-Oppenheimer approximation.

5.1 Lattice setup

The configurations utilized in this study are provided by the Coordinated Lattice Simulations (CLS) effort [82, 83], employing two dynamical flavors of $O(a)$-improved Wilson quarks and the Wilson plaquette action. The lattice parameters of the ensembles used are detailed in Tab. 5.1. Ensemble N6, characterized by a relatively small lattice spacing of $a = 0.0486$, was selected to investigate the potential at short distances. Ensemble A5, with a similar pion mass m_π and volume L, features a lattice spacing approximately 1.5 times larger than N6's lattice spacing.

The third ensemble, G8, has a pion mass much closer to the physical pion mass, allowing for the study of pion mass dependence. However, G8 also differs in lattice spacing and physical volume compared to A5 and N6.

We use stochastic propagators for the dynamical light quarks, with twelve sources per timeslice, and six (for ensemble N6) or eight (for ensembles A5 and G8) timeslices per configuration. These timeslices are separated by at least $8a$, ensuring they are essentially uncorrelated.

Table 5.1: Lattice details and smearing parameters consistent with algorithms defined in Section 4.5.1 and 4.5.2.

Ensemble	T/a	L/a	a[fm]	m_π[MeV]	N_{cfg}	α_{APE}	n_{APE}	κ_{G}	n_{G}
A5	64	32	0.0755	331	100	0.5	30	0.5	50
G8	128	64	0.0658	185	30	0.5	35	0.5	70
N6	96	48	0.0486	340	50	0.5	50	0.5	120

APE smearing is applied to the gauge fields, and Gaussian smearing is used for the fermion fields. The smearing parameters are listed in Tab. 5.1. Additionally, the HYP2 static action is employed.

Our computation code is based on the "openQ*D" code base [84] and might be included in future releases.

5.2 Static-light meson masses

For large separations, the $\bar{Q}\bar{Q}q_1q_2$ system is expected to behave as two non-interacting static-light mesons. The static-light meson masses are computed using the same configurations and stochastic propagators as part of the ratio of correlation functions defined in Eqn. (4.18).

Fig. 5.1 presents the effective mass plots for the static-light meson correlators from Eqn. (4.8) with spin structures $\Gamma = (1+\gamma_0)\gamma_5/2$ for the S meson and $\Gamma = (1+\gamma_0)/2$ for the P_- meson, with light quarks $q = u/d$ and $q = s$ for all three ensembles A5, N6, and G8. The plateau is fitted as indicated by the constant plotted in the fitting range of $t > 9a$ and $t > 8a$ for the S and P_- mesons, respectively.

The effective mass is shown only for $t > 2a$ because $m_{\text{eff}}(t = 1a)$ includes the correlator at $t = 0$, which is not meaningful due to large discretization errors. The effective mass for the S meson exhibits the typical behavior of m_{eff} as a monotonic decay to the plateau. Conversely, the m_{eff} of the P_- meson shows an unusually low data point at $t = 2a$, likely due to significant discretization effects at small distances.

Quantitative results on the static-light meson mass cannot be provided, as the mass diverges in the continuum limit due to the self-energy of the static quark. However, the mass differences between the S meson and the P_- meson can be computed, as the divergences cancel out. Tab. 5.2 summarizes the results for $m^{P_-}_{\bar{Q}q} - m^{S}_{\bar{Q}q}$ for both systems.

Computing the static-light correlation function requires substantially less computational time than the $\bar{Q}\bar{Q}q_1q_2$ correlation function, making it computationally inexpensive to reduce the statistical errors of this mass difference. However, these results for static-light mesons are just a byproduct of studying the $\bar{Q}\bar{Q}q_1q_2$ system. See [70, 71] for dedicated studies of the static-light system.

From now on, we will denote the masses as m^S and m^{P_-}, dropping the indices and assuming the meson systems are implicitly determined by the considered tetraquark system.

Table 5.2: Mass difference of the P_- and S meson for the ensembles A5, N6 and G8.

Ensemble	$(m^{P_-}_{\bar{Q}u/d} - m^{S}_{\bar{Q}u/d})$[MeV]	$(m^{P_-}_{\bar{Q}s} - m^{S}_{\bar{Q}s})$[MeV]
A5	384.0(12.4)	403.5(11.8)
N6	333.5(8.6)	374.4(5.3)
G8	347.8(9.2)	372.0(6.6)

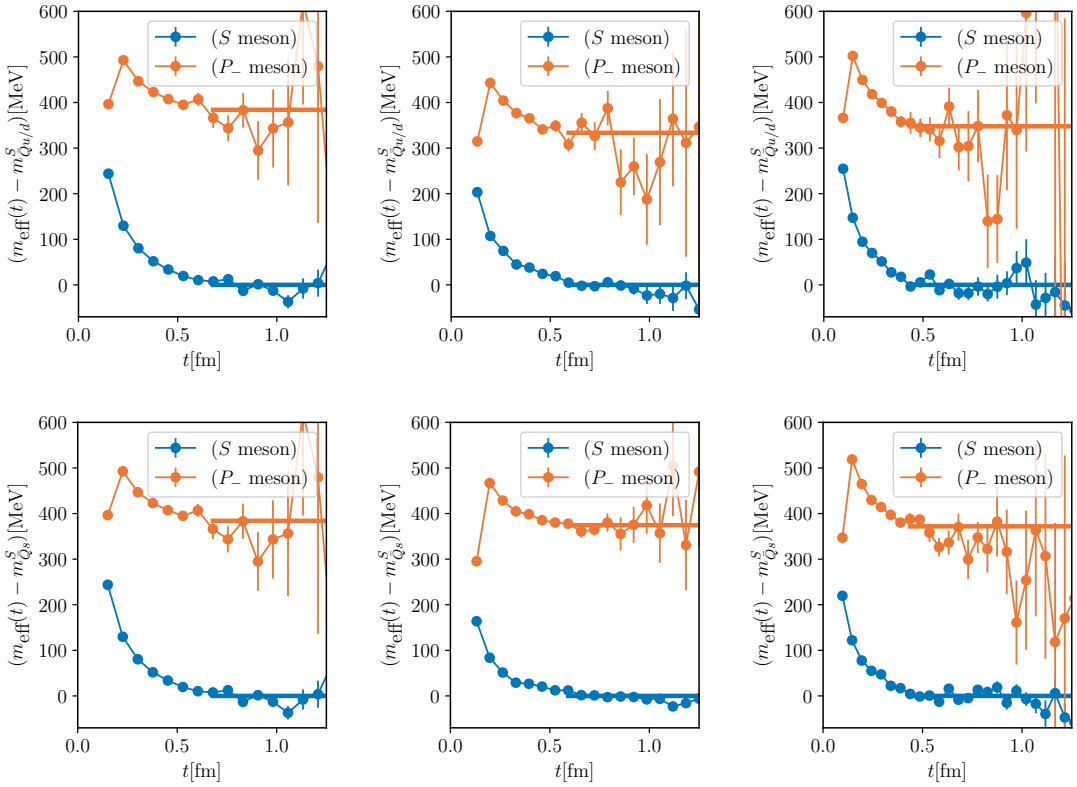

Figure 5.1: Effective masses of the S and P_- mesons $m_{\mathrm{eff}}(t)$ with light u/d (top) and s (bottom) quarks for ensembles A5 (left), G8 (center), and N6 (right) as a function of the temporal separation t normalized by the mass of the S meson $m^S_{\bar{Q}q}$. Constants indicate the fitting results and ranges of the plateaus.

5.3 Results for $\bar{Q}\bar{Q}ud$ potentials

Similarly to the static-light meson analysis, we compute the $\bar{Q}\bar{Q}ud$ correlation function and extract the potential from effective masses for each separation distance $r = |\mathbf{r}|$. This potential is computed for on-axis separations up to $r = 1.2$ fm and for all possible off-axis separations for $r \leq 4a$. Additionally, a subset of off-axis separations, including the space diagonal (x,x,x), the plane diagonal $(x,x,0)$, and all separations of the form $(x,1,2)$ for $r \leq 10a$ (with $x \in \mathbb{Z}$ and averaging over all permutations), is considered. Tree-level improvement was applied, and thus, the potentials are presented as functions of the improved distance r_{impr} determined by Eqn. (4.49).

We investigated all thirty-two independent creation operators listed in Tab. 4.2 and plotted the resulting potentials for ensemble N6 in Figs. 5.2 and 5.3. The shapes of the resulting potentials, i.e., whether they are attractive or repulsive and their asymptotic values, are consistent with our expectations and previous work [30].

It is important to note that our results are obtained using a single correlation function; thus, excited states cannot be rigorously computed. The results for excited states that we

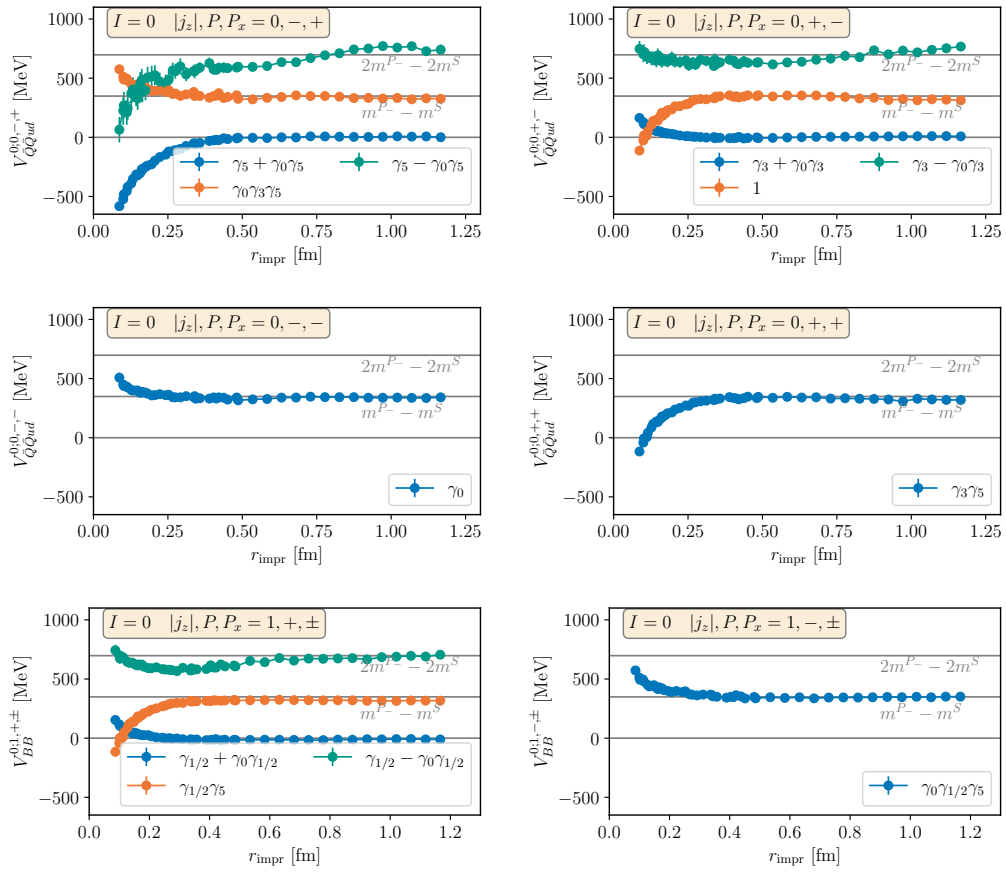

Figure 5.2: All twelve $\bar{Q}\bar{Q}ud$ potentials for $I = 0$ extracted from correlation functions corresponding to the creation operators collected in Tab. 4.2. Results for ensemble N6.

obtain stem from operators that have significant overlap with these states, causing the decay to the ground states to occur on a larger time scale. Consequently, our results for the excited states should only be interpreted qualitatively.

The primary focus of this work is on the attractive ground state potentials, which are the most promising candidates for hosting bound states and resonances, making them particularly interesting for phenomenological studies like [85]. Repulsive potentials with the lowest asymptotic value of $2m^S$ are also relevant as they can contribute to phenomenological descriptions, for instance, when including spin-splitting in the Born-Oppenheimer approximation [31, 46]. However, these repulsive potentials intersect with attractive potentials with an asymptotic value of $m^S + m^{P-}$ at small separations, rendering the results unreliable at these distances.

Before analyzing these specific potentials, we discuss the effective potentials, which serve as a good indicator of the data's quality.

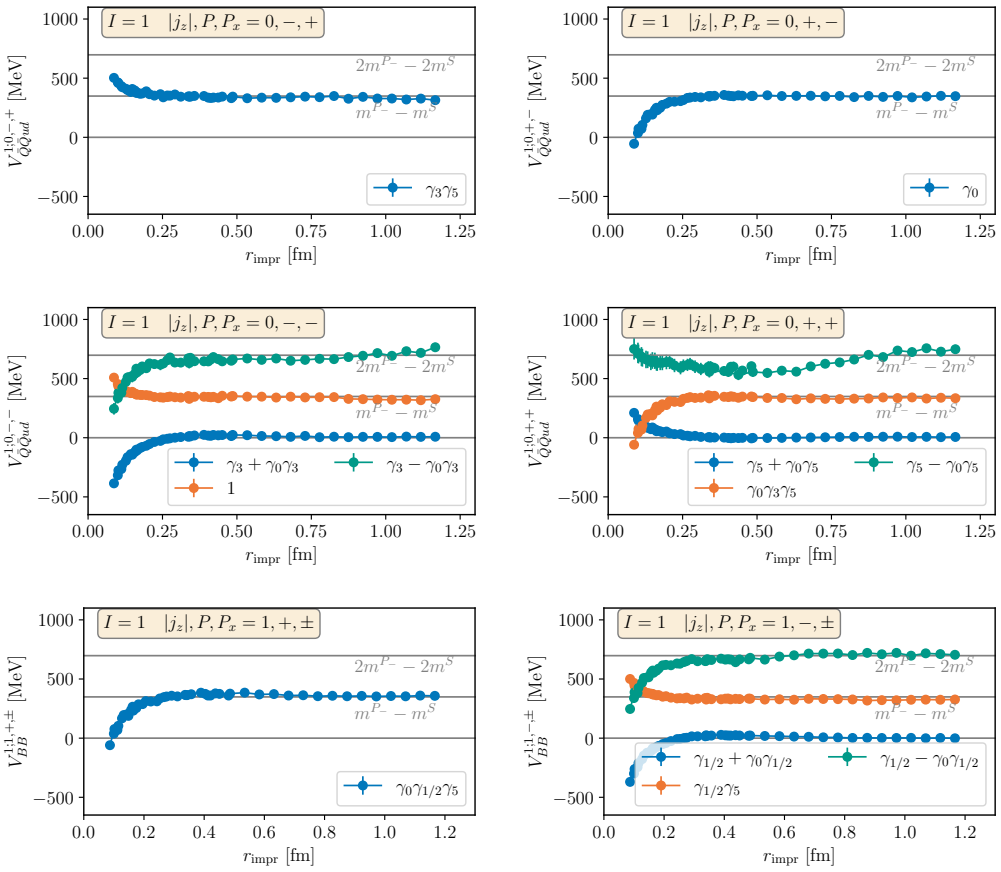

Figure 5.3: All twelve $\bar{Q}\bar{Q}ud$ potentials for $I = 1$ extracted from correlation functions corresponding to the creation operators collected in Tab. 4.2. Results for ensemble N6.

5.3.1 $\bar{Q}\bar{Q}ud$ effective potentials

For static potentials, it is necessary to fit constants to the effective potential $V^{I;|j_z|,\mathcal{P},\mathcal{P}_x}_{\bar{Q}\bar{Q}ud,\text{eff}}(r)$ for each on- and off-axis separation.

As previously discussed, the excited states are not well-defined in this study and only provide a qualitative picture. Additionally, these sectors generally exhibit larger statistical errors. Therefore, we extract the plateaus at fixed, relatively small temporal separations of $t = 4a$ for ensembles A5 and G8 and $t = 6a$ for ensemble N6.

For the ground states, we examine the effective potential more closely. Fig. 5.4 presents an example of the effective potentials for on-axis separations, ensemble N6, and the most attractive ground state with $\Gamma = \gamma_5 + \gamma_0\gamma_5$. Note that $V^{I;\Gamma}_{\bar{Q}\bar{Q}ud,\text{eff}}(r)$ stem from the ratio $C^{I,\Gamma}_{\bar{Q}\bar{Q}ud}(r)/C^{S}_{\bar{Q}u/d}$.

The effective potential declines slowly at small separations until the statistical errors become sufficiently large to fit a constant. However, it is plausible that the curve is approaching a lower plateau than indicated by the fit. This strongly suggests that the

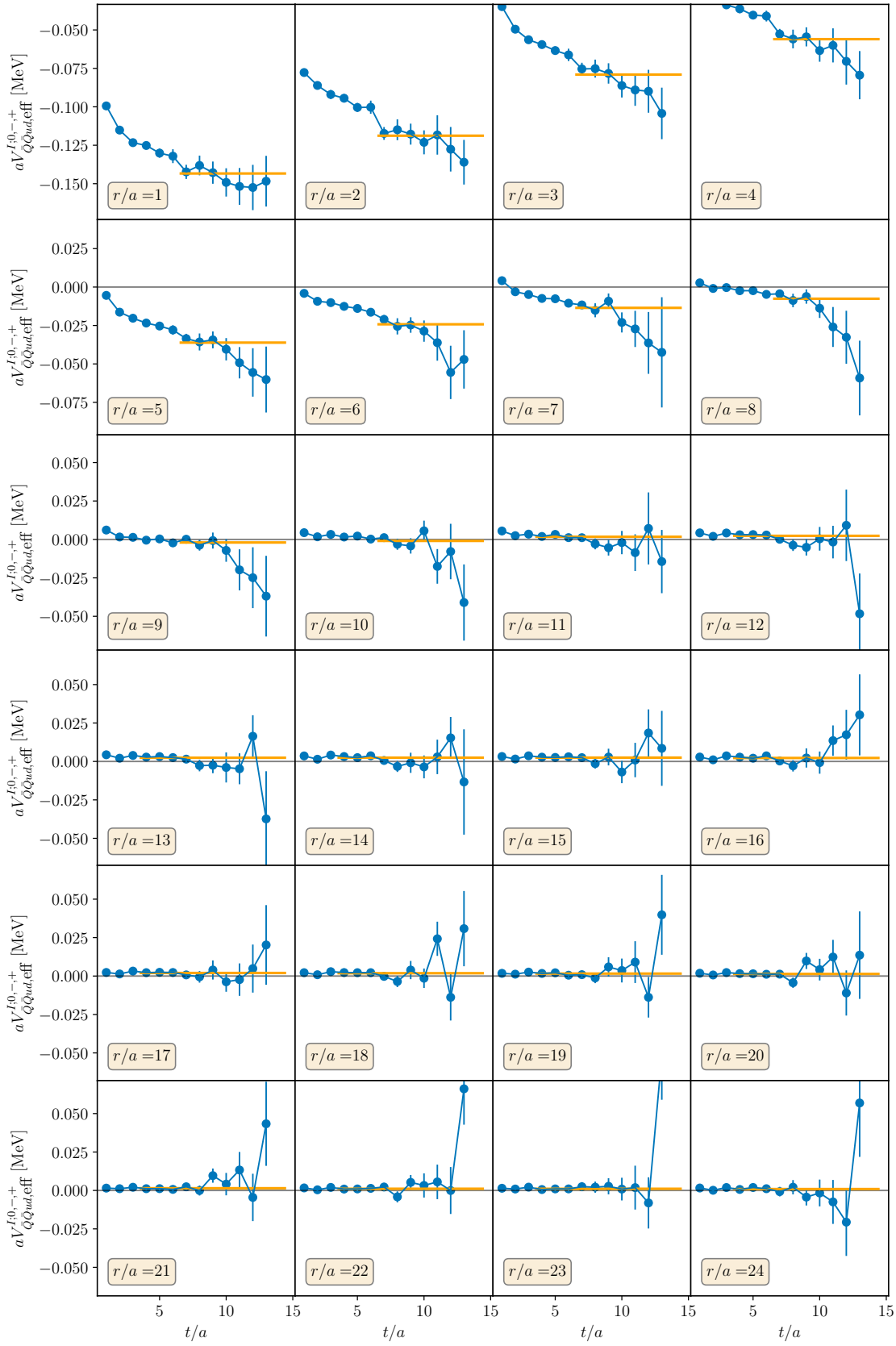

Figure 5.4: Effective mass plots corresponding to the most attractive potential $V^{0;0,-,+}_{\bar{Q}\bar{Q}ud,\mathrm{eff}}(r)$ for on-axis separations $r = 1a,2a,...24a$ for ensemble N6. Orange constants indicate the fitting range and results for $V^{0;0,-,+}_{\bar{Q}\bar{Q}ud}(r)$.

data quality is insufficient to make meaningful quantitative statements about the potential at small separations $r < 10a$, which is a significant limitation of this study. This issue is particularly pronounced in this and the two other attractive ground states in the $I = 1$ sector with quantum numbers $|j_z|, \mathcal{P}, \mathcal{P} = 0, -, -$ and $|j_z|, \mathcal{P}, \mathcal{P} = 1, -, \pm$.

At larger separations, the effective potentials for $r > 10a$ almost immediately reach a plateau close to zero, indicating that the $\bar{Q}\bar{Q}q_1q_2$ system at large separations behaves like two static-light mesons. As shown in Figure 5.4, we extract the plateaus starting at smaller t/a to reduce statistical errors.

The attractive ground state potentials are at least $\Delta E \approx 400$ MeV lower than the next excited state with an asymptotic value of $m^S + m^{P-}$. Contributions from excited states decay by $\exp(-\Delta E \cdot t)$ [67]. This implies that approximately 0.5 fm ≈ 400 MeV in t is required to suppress excited states by approximately $1/e$. We take the plateaus at $t \approx 0.5$ fm, again suggesting that there might still be contributions from excited states.

The picture is similar for effective potentials with off-axis separation, shown in Fig. B.1 in Appendix B.1. We also show an example of repulsive effective potentials in Fig. B.2 in Appendix B.1 where the plateaus at smaller separations appear more stable; however, as already discussed, the proximity of the attractive potential with a larger asymptotic value makes these results unreliable.

5.3.2 Potentials with asymptotic value $2m^S$

We identify three attractive ground state potentials: the most attractive with quantum numbers $I = 0$ and $|j_z|, \mathcal{P}, \mathcal{P} = 0, -, +$, and two less attractive by a factor of two in the $I = 1$ sectors $|j_z|, \mathcal{P}, \mathcal{P} = 0, -, -$ and $|j_z|, \mathcal{P}, \mathcal{P} = 1, -, \pm$. Additionally, we observe three repulsive potentials: two in the $I = 0$ sector with $|j_z|, \mathcal{P}, \mathcal{P} = 0, +, -$ and $|j_z|, \mathcal{P}, \mathcal{P} = 1, +, \pm$, and one in the $I = 1$ sector with $|j_z|, \mathcal{P}, \mathcal{P} = 0, +, +$. Fig. 5.5 presents these potentials for the three ensembles A5, G8, and N6, which show good agreement within the error margins. As discussed in the previous section, the plateaus for these potentials are somewhat uncertain; therefore, we refrain from making definitive statements about minor differences between the ensembles.

Possible phenomenological explanations of the potentials' behavior

At small separations, the potential is expected to be dominated by one-gluon exchange, which exhibits a Coulomb-like behavior with a leading term proportional to $c_\lambda \alpha_s / r$. The color factor $c_\lambda = \lambda_1\lambda_2/\mathrm{Tr}(\lambda_1\lambda_2)$ involves the Gell-Mann matrices λ and depends on the color configuration of the quarks. For $\bar{Q}\bar{Q}$ in a color triplet, $c_\lambda = -1/2$, resulting in an attractive potential. Conversely, for $\bar{Q}\bar{Q}$ in a color sextet, $c_\lambda = 1/4$, leading to a repulsive potential. This relationship initially discussed in Section 4.3.1 and formulated in [31], aligns with the observed potentials and explains why the repulsive potentials are approximately half as strong as the attractive ones.

At larger separations, the system resembles two B mesons separated by distance r, where the light quark clouds around each heavy quark screen the other heavy quark's charge, causing the antiquark-antiquark interaction to vanish.

Another significant contribution to the potentials arises from the interaction of the light quark spins, primarily governed by the hyperfine potential, which is proportional to

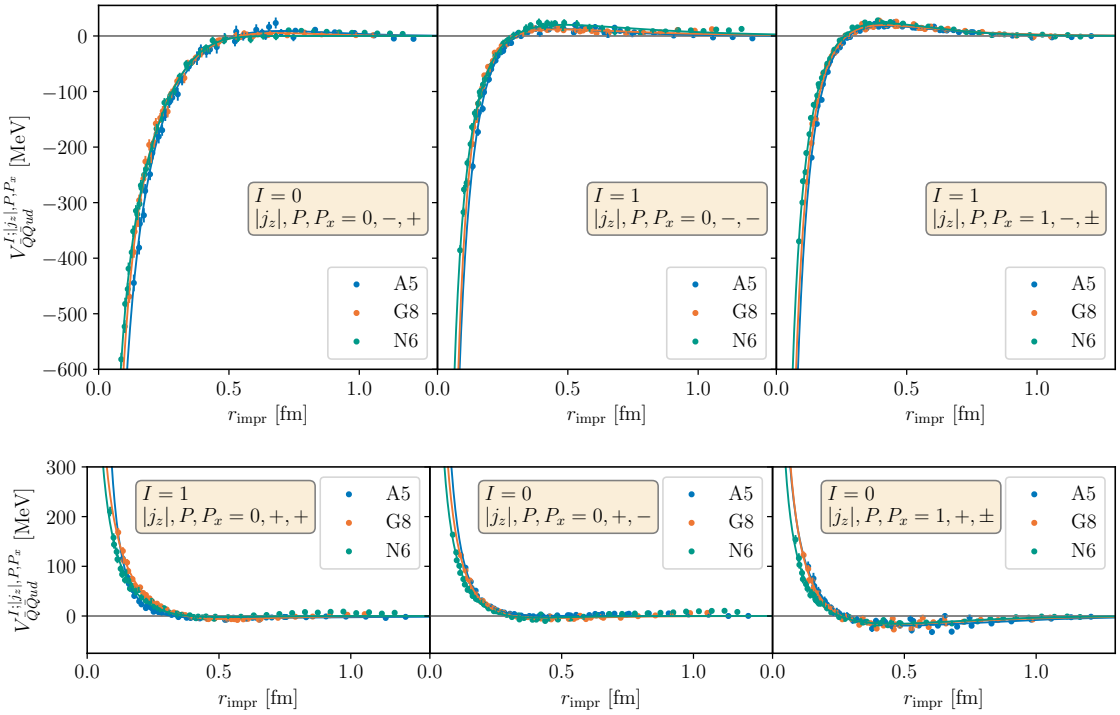

Figure 5.5: Attractive ground state $\bar{Q}\bar{Q}ud$ potentials (top) and lowest lying repulsive $\bar{Q}\bar{Q}ud$ potentials (bottom) for the ensembles A5, G8 and N6.

$-c\boldsymbol{\sigma}^1 \cdot \boldsymbol{\sigma}^2$. Here, $\boldsymbol{\sigma}^{1/2}$ denote the Pauli matrices, which couple to the spins of the light quarks and depend on the spin quantum number of the state.

While $|j_z|$ was used as a quantum number for this system, in this context, it is useful to define the total angular momentum j, to which the operators can also be related. Operators with $\Gamma = \gamma_5, \gamma_0, 1, \gamma_0\gamma_5$ correspond to $j = 0$, while all other operators correspond to $j = 1$.

We find that $-\boldsymbol{\sigma}^1 \cdot \boldsymbol{\sigma}^2 = +3$ for $j = 0$ and $-\boldsymbol{\sigma}^1 \cdot \boldsymbol{\sigma}^2 = -1$ for $j = 1$. This explains why the most attractive potential with $I = 0$ and $|j_z|, \mathcal{P}, \mathcal{P} = 0, -, +$ is significantly more attractive than the potentials in the $I = 1$ sectors $|j_z|, \mathcal{P}, \mathcal{P} = 0, -, -$ and $|j_z|, \mathcal{P}, \mathcal{P} = 1, -, \pm$.

Another important consideration is the behavior of the system at large separations. As previously mentioned and supported by the data, the potential at large distances is essentially twice the mass of two non-interacting static-light mesons. The two static antiquarks can be interpreted as a single anticolor source at small separations, making the system equivalent to a static baryon. When the two static antiquarks are separated, the static baryon system transitions into a system of two non-interacting static-light mesons at large separations, which generally have a different mass. In other words, at large separations, the potential corresponds to $2m^S$, while at smaller separations, it corresponds to $m_{\text{Baryon}} + V(r)$, where m_{Baryon} is the static baryon mass (containing two static antiquarks at the same position) and $V(r)$ is the potential from interactions.

To further investigate this, we considered the difference between the most attractive

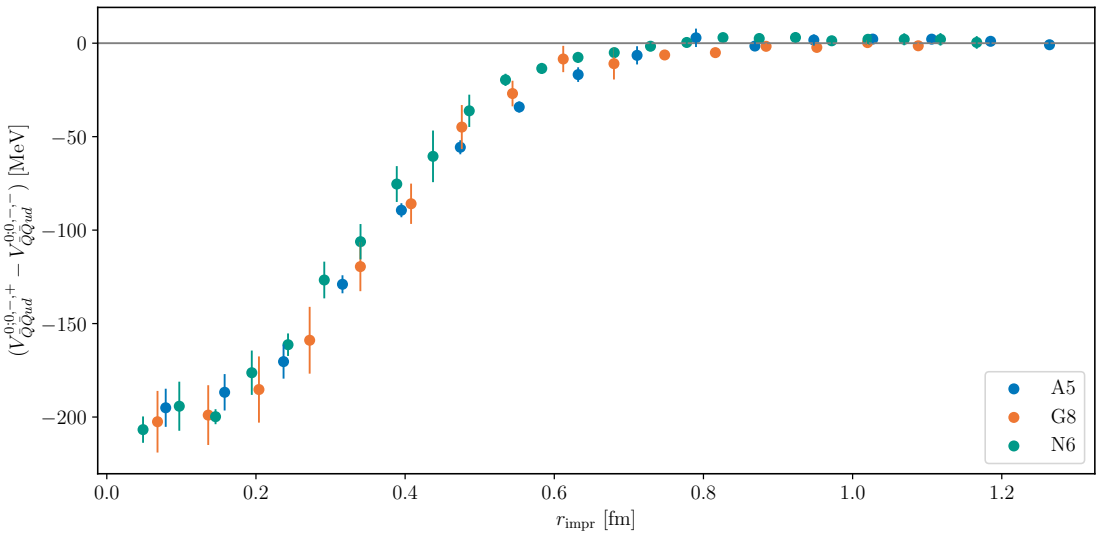

Figure 5.6: Difference between the two ground state potentials $V_{BB}^{0;0,-,+}(r)$ and $V_{BB}^{0;0,-,-}(r)$. This difference corresponds to the difference between two static-light baryons or the "good" and "bad" diquark at small distances.

potential and the less attractive potentials $V_{BB}^{0;0,-,+}(r) - V_{BB}^{0;0,-,-}(r)$ by studying the ratios of their correlators. The result is shown in Fig. 5.6, where at small separations, we observe a mass difference of approximately 200 MeV, consistent with studies of static baryons where these potentials at vanishing separation should correspond to static baryon quantum numbers $j^P = 0^+$ and $j^P = 1^-$ [86], or to the "good" and "bad" diquarks [87]. Note that the values of the potential at very small separations suffer from severe discretization errors as the potential diverges. However, these results are still meaningful as we consider the difference between two potentials, and the divergences cancel each other.

At intermediate separations, we observe a "bump" in some potentials, i.e., a change of sign in the potential followed by an extremum before approaching the asymptotic value. This behavior can be attributed to several factors. One explanation is the difference in masses between the static-light baryon system at small separations and the system of two static-light mesons at large separations. Other possible explanations include meson exchange potentials or the flip-flop between a tetraquark string and two meson strings [88].

At large separations, only the one-pion-exchange potential (OPEP) should contribute [89], as pions are the mesons with the smallest mass $m_\pi \approx 140$ MeV. The OPEP is proportional to

$$(\boldsymbol{\tau}_1 \cdot \boldsymbol{\tau}_2)\left((3(\boldsymbol{\sigma}_1 \cdot \hat{\mathbf{r}})(\boldsymbol{\sigma}_2 \cdot \hat{\mathbf{r}}) - \boldsymbol{\sigma}_1 \cdot \boldsymbol{\sigma}_2)\left(1 + \frac{3}{m_\pi r} + \frac{3}{(m_\pi r)^2}\right) + \boldsymbol{\sigma}_1 \cdot \boldsymbol{\sigma}_2\right)\frac{e^{m_\pi r}}{r}. \quad (5.1)$$

Eqn. (5.1) also includes a hyperfine splitting term, $(\boldsymbol{\tau}_1 \cdot \boldsymbol{\tau}_2)(\boldsymbol{\sigma}_1 \cdot \boldsymbol{\sigma}_2)$, which induces a potential with the opposite sign to the Coulomb potential due to the Pauli principle. This would manifest as a "bump" at large separations; however, we expect this effect to be very

weak and, thus, difficult to observe.

There is also a tensor part $(\boldsymbol{\tau}_1 \cdot \boldsymbol{\tau}_2)(\boldsymbol{\sigma}_1 \cdot \hat{\mathbf{r}})(\boldsymbol{\sigma}_2 \cdot \hat{\mathbf{r}})$, which depends on the spin orientation relative to the separation axis $\hat{\mathbf{r}} \equiv \hat{e}_z$ and the isospin I. We summarize the resulting factors in Tab. 5.3. This might explain the differences in the center and right panel potentials from Fig. 5.5. In Fig. 5.5, the lower center and right panel ($I = 0$) potentials differ significantly at large separations, consistent with the factors from Fig. 5.3, which indicate a shift in different directions due to this effect. While in the $I = 1$ sector, these factors are also of opposite sign; they are smaller by a factor of 3, which is supported by our results in the upper center and right panels of Fig. 5.5. Tab. 5.3 also implies $(V_{BB}^{0;1,+,\pm}(r) - V_{BB}^{0;0,+,-}(r))/(V_{BB}^{1;1,+,\pm}(r) - V_{BB}^{1;0,+,-}(r)) \approx 3$ at large separations. Our potentials are consistent with this value, albeit with a large statistical error.

5.3.3 Off-axis separations

As discussed in Section 4.3.1, the rotational symmetry on the lattice breaks down to subgroups of the cylindrical rotation group $D_{\infty h}$ depending on the relative positions of the two quarks on the lattice. Depending on the symmetry group, this leads to a distinct mixing of angular momentum states. In terms of our results, this raises two concerns. Firstly, when a trial state overlaps with multiple states of different angular momentum, the correlator may be contaminated by these states, potentially leading to a slower decay to a plateau. This would be indicated by a systematic upward shift of data points associated with symmetry groups that include more angular momentum states. In Fig. 5.7, we present the data points for the six potentials with an asymptotic value of $2m^S$, grouped by symmetry. The results for off-axis symmetry groups D_{2h}, D_{3d}, C_{2h}, and C_i appear robust, as they do not exhibit significantly more contamination by higher angular momentum states compared to D_{4h}.

A second concern arises concerning the symmetry groups C_{2h} and C_i. We study sectors with angular momentum $|j_z| = 0$ and $|j_z| = 1$, which mix for symmetry groups C_{2h} and C_i as shown in Tab. 4.1. This implies that all states from both sectors contribute to the potential at these separations. However, these sectors correspond to the attractive $I = 1$ potentials with quantum numbers $|j_z|, \mathcal{P}, \mathcal{P} = 0, -, -$ and $|j_z|, \mathcal{P}, \mathcal{P} = 1, -, \pm$ (top middle and right panels), which are essentially identical, and the repulsive $I = 0$ potentials, $|j_z|, \mathcal{P}, \mathcal{P} = 0, +, -$ and $|j_z|, \mathcal{P}, \mathcal{P} = 1, +, \pm$ (bottom middle and right panels of Fig. 5.7), which show only a small difference at intermediate to large separations that might be due to one-pion exchange as discussed in the previous section.

The data points for separations with symmetry groups C_{2h} and C_i are consistent with the curve indicated by all other data points; hence, we present results for all separations.

Table 5.3: Values for the tensor part $(\boldsymbol{\tau}_1 \cdot \boldsymbol{\tau}_2)(\boldsymbol{\sigma}_1 \cdot \hat{\mathbf{r}})(\boldsymbol{\sigma}_2 \cdot \hat{\mathbf{r}})$ of the one-pion-exchange potential in Eqn. (5.1) as a function of angular momentum $|j_z|$ and isospin I.

$(\boldsymbol{\tau}_1 \cdot \boldsymbol{\tau}_2)(\boldsymbol{\sigma}_1 \cdot \hat{\mathbf{r}})(\boldsymbol{\sigma}_2 \cdot \hat{\mathbf{r}})$		$\lvert j_z\rvert = 0$ $(\boldsymbol{\sigma}_1 \cdot \hat{\mathbf{r}})(\boldsymbol{\sigma}_2 \cdot \hat{\mathbf{r}}) = -1$	$\lvert j_z\rvert = 1$ $(\boldsymbol{\sigma}_1 \cdot \hat{\mathbf{r}})(\boldsymbol{\sigma}_2 \cdot \hat{\mathbf{r}}) = 1$
$I = 0$	$\boldsymbol{\tau}_1 \cdot \boldsymbol{\tau}_2 = -3$	3	-3
$I = 1$	$\boldsymbol{\tau}_1 \cdot \boldsymbol{\tau}_2 = 1$	-1	1

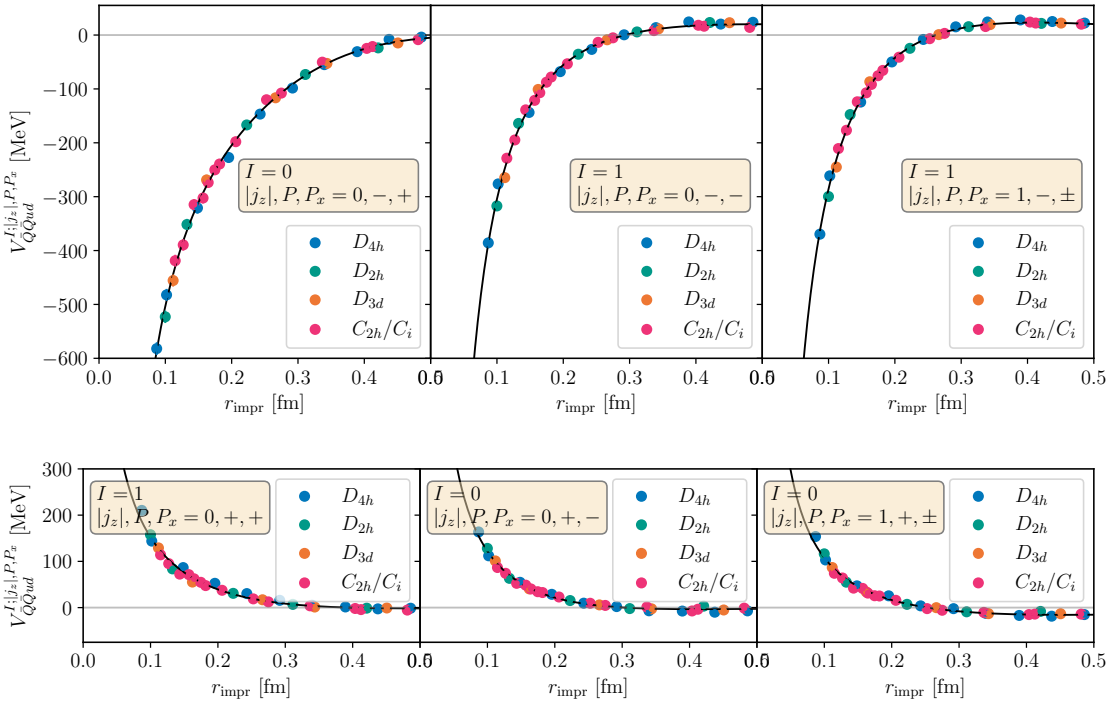

Figure 5.7: All attractive (top) and repulsive (bottom) $\bar{Q}\bar{Q}ud$ potentials with the lowest asymptotic value of $2m^S$ for ensemble N6. Different symmetry groups D_{4h}, D_{2h}, D_{3d}, C_{2h} and C_i of separations are indicated by separate colours.

However, we cannot exclude the possibility that these two effects contribute or compensate each other to some extent. Therefore, the results for these separations should be considered with caution.

5.3.4 Results for $\bar{Q}\bar{Q}us$ potentials

We also compute potentials in the $\bar{Q}\bar{Q}us$ system. The results for the potentials with asymptotic value $m^S_{\bar{Q}u/d} + m^S_{\bar{Q}s}$ for the ensemble N6 are presented in Fig. 5.8. Given the similarity of these potentials to those in the $\bar{Q}\bar{Q}ud$ system, our primary focus is on the differences. Therefore, we also include the corresponding $\bar{Q}\bar{Q}ud$ potentials in the plot for comparison. Notably, we observe significantly less binding in the $\bar{Q}\bar{Q}us$ system within the most attractive sector characterized by $|j_z|, \mathcal{P}, \mathcal{P} = 0, -, +$, which aligns with theoretical expectations. Additionally, the repulsive potential in the sector $|j_z|, \mathcal{P}, \mathcal{P} = 0, +, \pm$ appears to be slightly more repulsive. The other potentials remain unchanged when substituting the d quark with an s quark. These observations are consistent for all three ensembles; we show corresponding results for ensembles A5 and G8 in Appendix B.2.

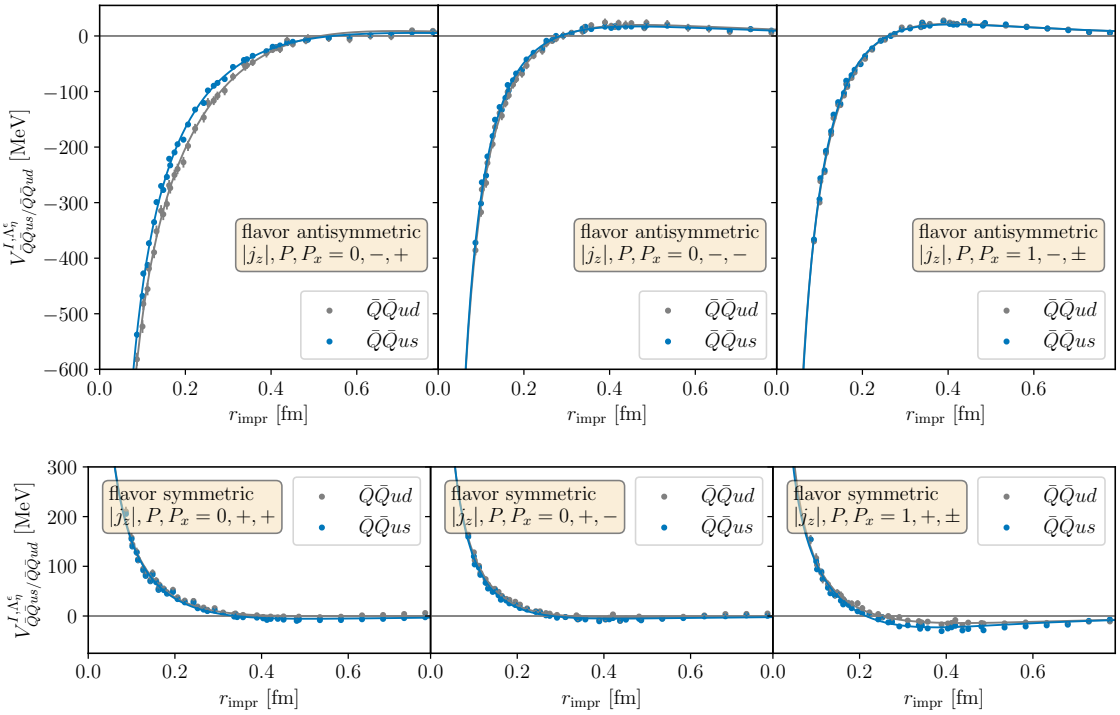

Figure 5.8: All attractive (top) and repulsive (bottom) $\bar{Q}\bar{Q}us$ potentials with asymptotic value $m^S_{\bar{Q}u/d} + m^S_{\bar{Q}s}$ for ensemble N6. The gray data points and fits indicate corresponding $\bar{Q}\bar{Q}ud$ results.

5.3.5 $\bar{Q}\bar{Q}q_1q_2$ potentials in the Schrödinger equation

We now consider bottomonium $\bar{Q} = \bar{b}$ and solve a radial Schrödinger equation

$$\left(\frac{1}{2m_b} + V(r)\right)\frac{R(r)}{r} = E\frac{R(r)}{r}, \tag{5.2}$$

where $R(r)$ is the radial part of the wave function $\psi(\mathbf{r})$, m_b is the mass of the b quark, and $V(r)$ is the static potential obtained from lattice QCD. The choice of this potential also determines the quantum numbers of the system. We will restrict this discussion to the most attractive potential in the sector $(I = 0;)\ |j_z|, \mathcal{P}, \mathcal{P}_x = 0, +, -$, which is the most likely to host a bound state [29, 30] and corresponds to $I(J^P) = 0(1^+)$ if $q_1q_2 = ud$.

Fitting ansatz

We fit the data to a suitable ansatz to utilize the potentials in a phenomenological model. Based on our arguments from Section 5.3.2, we motivate a Coulomb-like interaction at small separations, i.e., $\propto \alpha/r$, screened by an exponential at larger separations of the form $\exp(-(r/d)^p)$. This leads to the parametrization

$$V_1(r) = -\frac{\alpha_1}{r}\exp\left(-\left(\frac{r}{d}\right)^p\right) \tag{5.3}$$

with three fitting parameters α, d, and p. This ansatz has been used previously to parametrize antistatic-antistatic-light-light potentials [29, 30] and works well for the most attractive ground state potential $V^{0;0,-,+}_{\bar{Q}\bar{Q}q_1q_2}(r)$. However, as discussed, we observe a change in sign at intermediate to large separations for some other potentials, indicating an additional effect. The ansatz from Eqn. (5.3) cannot describe this behavior, so we include an additional term to fit these potentials. There are many possible ways to incorporate this behavior into the parametrization. We decide to use the idea of a mass difference of the system at small separations (static-light baryon) and large separations (two non-interacting B mesons) to motivate the parametrization

$$V_2(r) = \left(-\frac{\alpha_1}{r} + c\right) \exp\left(-\left(\frac{r}{d}\right)^p\right) \tag{5.4}$$

with an additional fitting parameter c. This ansatz was used to produce all the curves indicated in Figs. 5.5, 5.7 and 5.8. We summarize fitting parameters for the six most relevant potentials in Appendix B.3, Tab. B.1.

Binding energy

We can consider both different parametrizations from Eqns. (5.3) and (5.4), as the relevant potential in this Schrödinger equation (5.2) has no distinct repulsive behavior at intermediate to large distances. We first consider the resulting fitting parameters for the system $\bar{b}\bar{b}ud$. The fit functions resulting from these parameters are very comparable in their errors. However, the corresponding binding energies E_B show a different picture. The results for the different ensembles and parametrizations take very different values and are partly separated by multiple standard deviations σ. This indicates large systematic errors in addition to significant statistical errors. This further supports our suspicion that our results systematically overestimate the true value of the potentials, as indicated in Section

Table 5.4: Fitting parameters for the fits from Eqns. (5.3) and (5.4) to $V^{(0);0,-,+}_{\bar{Q}\bar{Q}q_1q_2}(r)$ and resulting binding energies for the $\bar{b}\bar{b}q_1q_2$ systems from solving Eqn. (5.2).

$\bar{b}\bar{b}q_1q_2$	Ens.	V_{fit}	α_1	d[fm]	p	c [MeV]	E_B[MeV]
$\bar{b}\bar{b}ud$	A5	V_1	0.356(0.024)	0.307(0.017)	2.21(0.33)		48(11)
		V_2	0.436(0.024)	0.570(0.064)	1.99(0.337)	164(19)	60(12)
	G8	V_1	0.298(0.017)	0.316(0.014)	2.27(0.36)		17(5)
		V_2	0.359(0.012)	0.552(0.067)	2.28(0.74)	130(16)	20(5)
	N6	V_1	0.264(0.010)	0.336(0.015)	2.74(0.29)		11(5)
		V_2	0.271(0.074)	0.349(0.029)	2.93(0.77)	19(53)	12(5)
$\bar{b}\bar{b}us$	A5	V_1	0.335(0.010)	0.282(0.007)	2.05(0.12)		no binding
		V_2	0.414(0.017)	0.468(0.027)	1.70(0.23)	156(6)	no binding
	G8	V_1	0.325(0.009)	0.250(0.005)	1.78(0.08)		3(1)
		V_2	0.404(0.014)	0.409(0.019)	1.28(0.11)	157(6)	5(2)
	N6	V_1	0.251(0.004)	0.310(0.011)	2.11(0.10)		no binding
		V_2	0.290(0.004)	0.612(0.040)	2.14(0.26)	107(5)	no binding

5.3.1.

To put this into perspective, we construct a potential that creates a binding energy of -100 MeV by using the ansatz from Eqn. (5.3), keeping $d = 0.45$ fm, $p = 2$ constant and increasing α until we reach -100 MeV binding energy. In Fig. 5.9, we again show the relevant, effective masses for small to intermediate on-axis separations ≈ 0.15 fm $- 0.4$ fm but added a red constant indicating the necessary effective mass to obtain this potential. The red constants are within reach of our effective masses, and it seems possible that the data could converge to this value for a larger t.

For the system $\bar{b}\bar{b}us$, we generally observe less binding, which was expected from the less attractive potentials. However, only the G8 ensemble indicates a binding by $> 3\sigma$, while no definite conclusion can be made for the other ensembles if a bound state exists.

In sum, the resulting fit functions are very unstable between the different parametrizations $V_1(r)$ and $V_2(r)$ and for different ensembles A5, G8, and N6. While we could try to understand what causes the discrepancies between different ensembles, the binding energy's error and different results for different parameterizations indicate insufficient statistics to back up any possible statements. We believe that a cause of the vastly different results is the proximity to the threshold. Would the potential be more attractive, similar fluctuations in the fitting parameters would probably cause significantly less severe fluctuations in the binding energy E_B.

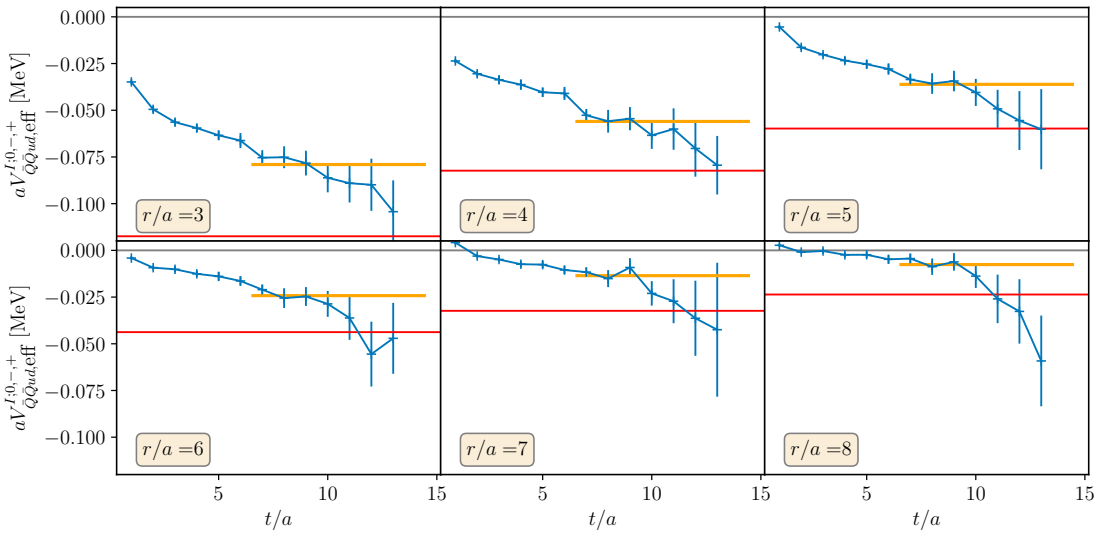

Figure 5.9: Effective mass plots corresponding to the most attractive potential $V^{0;0,-,+}_{\bar{Q}\bar{Q}ud,\mathrm{eff}}(r)$ for on-axis separations $r = 3a,...8a$ for ensemble N6. Orange constants indicate the fitting range and results for $V^{0;0,-,+}_{\bar{Q}\bar{Q}ud}(r)$. The red constants correspond to an artificially generated potential, which creates a binding of 100 MeV.

CHAPTER 6

Conclusion

Despite our efforts, we were unable to achieve the goal of producing high-quality $\bar{Q}\bar{Q}ud$ static potentials to provide a robust prediction of the $I(J^P) = 0(1^+)$ bound state within the Born-Oppenheimer approximation. Nevertheless, significant advancements were made in the techniques employed, such as employing tree-level improvement and including off-axis separations. Additionally, we identified the primary challenges and difficulties associated with studying this system.

Improving the plateaus at low separations is crucial, as there are strong indications that the effective mass decays slowly to a lower value. A logical next step would be considering correlation matrices instead of single correlators. Using N different correlators for given sectors, one can construct an $N \times N$ correlation matrix and extract the first N energy states as eigenvalues. This approach offers the benefit of rigorously separating the ground state and $N-1$ excited states, thereby obtaining a valid result for the repulsive potentials with an asymptotic value of $2m^S$, which intersects at small separations with an attractive potential of a higher asymptotic value. Furthermore, this method would reduce the contamination of the ground states by excited states. In this study, the first excited state, approximately 400 MeV above the ground state, contributed to the contamination. With $N \times N$ correlation matrices, the first excited state contaminating the ground state would be the N-th excited state, generally $\geq$ 800 MeV above the ground state. This substantial reduction in contamination means that a plateau is reached for smaller values of t when the signal-to-noise ratio is better.

In this context, it is essential also to explore fundamentally different operators to include in the correlation matrix. So far, we only considered operators corresponding to two B mesons separated by r by putting each light quark at the position of a static antiquark. Another possibility would be constructing a diquark-antidiquark system by placing a pair of two light quarks at the center between both static antiquarks. This is expected to have a larger overlap to the ground state for small separations $r < 0.3$ fm compared to the system of two B mesons, as shown in [90, 91].

Moreover, the overlap with the ground state can be further increased by employing suitable smearing techniques. Exploring more modern smearing algorithms, such as gradient flow [92], seems like a logical next step.

One more direction can be explored with the existing data: applying more sophisticated methods to extract effective potentials from the correlators. The previous work [30] applied a technique where the fit parameters α, d and p from Eqn. (5.3) were extracted from many different fits of the data, weighting every contribution by $\exp(-\chi^2/dof)$ as outlined in [93].

Furthermore, a recently suggested method applies the Lanczos algorithm to the transfer matrix to extract the effective masses and is very promising [94, 95].

We consider this study as an initial step towards achieving high-quality $\bar{Q}\bar{Q}ud$ and $\bar{Q}\bar{Q}ud$ static potentials. We are confident that these potentials can be computed with high precision by applying the abovementioned techniques and investing sufficient computational resources to improve this work's results.

We have already discussed extensively the importance of these potentials in resolving the tension between results from non-relativistic QCD with the finite volume method and results from the Born-Oppenheimer approximation using the static potentials computed in this work. However, these potentials could also be of significant interest in other contexts. The quantum numbers of our systems closely resemble those of nucleon-nucleon systems, as both systems have isospin 1/2 and spin 1/2 due to the static antiquarks in our potentials. There are many phenomenological descriptions for the shape of the $N - N$ potential [96–100] but most predicted effects have yet to be definitively observed in experiments. The $N - N$ system is also extremely challenging to treat with lattice QCD. Therefore, observing some of the predicted effects for the nucleon-nucleon system within our potentials could be a meaningful contribution. In the current results, we observe effects that can be vaguely explained by one-pion exchange, which is also expected in $N - N$ systems. Still, the data quality is not stable enough to support any definitive claims.

Part II

Bottomonium resonances in the Born-Oppenheimer approximation using lattice QCD static potentials

CHAPTER 7

Introduction

In the second part of this dissertation, we investigate a different tetraquark system, $\bar{b}b\bar{q}q$, which consists of a heavy quark-antiquark pair in the presence of a light quark-antiquark pair. While the $\bar{b}\bar{b}q_1q_2$ systems have been effectively studied in lattice QCD using non-relativistic heavy quarks, similar methods have not been successful for the $\bar{b}b\bar{q}q$ system due to the increased number of scattering channels. Experimentally, however, there are results for the spectrum of bound states for bottomonium, including multiple resonances in the $I = 0$ sector, such as $\Upsilon(10860)$, $\Upsilon(11020)$ and the recently discovered $\Upsilon(10750)_{\text{BELLE II}}$ [22]. We focus on the $I = 0$ system in this work; similar efforts have been conducted on the $I = 1$ system [101, 102], which correspond to the tetraquarks $Z_b(10610)$ and $Z_b(10650)$ found by Belle [6, 103].

As proposed in Section 4.3.2, the potentials of a static quark-antiquark pair in the presence of a light quark-antiquark pair can be computed similarly to the $\bar{b}\bar{b}q_1q_2$ system discussed in previous chapters. In this part of the thesis, we utilize existing results from [72] and extend the framework introduced in [104], employing these potentials within the Born-Oppenheimer approximation. This system is more complex due to the involvement of additional scattering channels. Specifically, the quarkonium channel must be included, as the quantum numbers of the $\bar{b}b\bar{q}q$ tetraquark candidates can also be realized in ordinary bottomonium $\bar{b}b$. Consequently, we must consider coupled channels of bottomonium and meson-meson states.

In the existing work [104], two channels are considered in the S wave, i.e., for angular momentum 0, a bottomonium channel $\bar{b}b$ and a meson-meson channel corresponding to $\bar{b}b(\bar{u}u + \bar{d}d)$, i.e., with $I = 0$.

We aim to extend this formalism by incorporating a third channel, which includes mesons with strange quarks ($\bar{b}b\bar{s}s$), as the threshold for this channel lies in the same energy region as the most relevant resonance energies, at $\approx 10.800\,\text{MeV}$. Including this channel is essential for making meaningful predictions at these energies. Furthermore, we derive the Schrödinger equation for this system for higher angular momenta to study the P, D, and F wave spectra, corresponding to angular momenta 1, 2, and 3, respectively. Additionally, we investigate the composition of the resonances we identify, determining whether the state is predominantly quarkonium-like or has a significant meson-meson component, indicating an exotic nature. These extensions are particularly relevant for clarifying the nature of the $\Upsilon(10750)$, $\Upsilon(10860)$, and $\Upsilon(11020)$ resonances observed experimentally, as $\Upsilon(10860)$ and $\Upsilon(11020)$ are often categorized as S wave bottomonium states $\Upsilon(5S)$ and $\Upsilon(6S)$, while they could also belong to the D wave spectrum. The recently discovered $\Upsilon(10750)$ resonance is

a promising candidate for an exotic state.

We commence the second part in Chapter 8 by outlining the framework for computing bound states and resonances in the Born-Oppenheimer approximation using static potentials from lattice QCD as introduced in [104]. Subsequently, we extend this framework to arbitrary angular momenta and incorporate a $\bar{b}b\bar{s}s$ channel. In the final chapter of this dissertation, Chapter 9, we present results for bound states and resonances by solving the coupled channel Schrödinger equation derived in the preceding section. This includes a quarkonium channel and four meson-meson channels (two corresponding to $\bar{b}b(\bar{u}u + \bar{d}d)$ and two corresponding to $\bar{b}b\bar{s}s$) in the S, P, D, and F wave channels. We then discuss our predictions in the context of experimental results and compare them to other theoretical predictions from [105–110].

CHAPTER 8

Studying bottomonium in the Born-Oppenheimer approximation using static potentials from lattice QCD

In this section, we present a methodology that utilizes static potentials derived from lattice QCD to determine the spectrum of bottomonium within the Born-Oppenheimer approximation. This approximation applies to systems where interacting particles operate on significantly different scales. By employing this approach, we solve the Schrödinger equation for heavy quarks, such as $\bar{b}b$, while incorporating the influence of light quarks through static potentials computed via lattice QCD. This approximation simplifies the complex quantum field theoretical problem into a better treatable quantum mechanical problem.

This chapter commences with a brief review of scattering theory in quantum mechanics, emphasizing the concepts most relevant to our approach. Subsequently, we derive the Schrödinger equation, encompassing both a quarkonium channel and a $I = 0$ meson-meson channel with light quarks $\bar{u}u+\bar{d}d$. We introduce relevant restrictions and a meaningful set of quantum numbers for this system. Following this, we discuss existing lattice computations of quarkonium static potentials, initially performed in studying string breaking, and relate them to the potential in our Schrödinger equation. We then construct a set of angular momentum eigenfunctions to enable partial wave decomposition and the projection of the Schrödinger equation onto definite angular momentum. We also consider the wave function's asymptotic behavior to construct the T-matrix.

Finally, we extend the wave function to incorporate a meson-meson channel $\bar{M}_s M_s$ with s quarks as light quarks and derive the corresponding 5×5 coupled channel Schrödinger equation. We also introduce a method to extract the composition of bound states and resonances by analyzing the components of the wave functions.

8.1 Scattering theory in quantum mechanics

The stationary Schrödinger equation in three spatial dimensions is given by

$$\left(-\frac{1}{2m}\nabla^2 + V(\mathbf{r})\right)\phi_k(\mathbf{r}) = E(k)\phi_k(\mathbf{r}), \tag{8.1}$$

where $E = k^2/2m$ and $k = |\mathbf{k}|$. The wave number k enumerates the solutions $\phi_k(\mathbf{r})$ of the equation with energy $E(k)$.

When switching to spherical coordinates, an arbitrary energy eigenfunction $\phi_k(\mathbf{r})$ can be expanded using a superposition of spherical Bessel functions $j_l(kr)$ and Neumann functions

$n_l(kr)$,

$$\phi_k(\mathbf{r}) = \sum_{l=0}^{\infty} \sum_{m=-l}^{l} \left(A_{lm}(k) j_l(kr) + B_{lm}(k) n_l(kr)\right) Y_{lm}(\theta,\phi), \tag{8.2}$$

where $Y_{lm}(\theta,\phi)$ are spherical harmonics. For example, a plane wave propagating in the z-direction, e^{ikz}, can be written as

$$e^{ikz} = \sum_{l=0}^{\infty} i^l (2l+1) j_l(kr) P_l(\cos(\theta)), \tag{8.3}$$

where $P_l(\cos(\theta)) = \sqrt{\frac{4\pi}{2l+1}} Y_{l0}(\theta,\phi)$ are the Legendre polynomials, which are proportional to the ϕ-independent spherical harmonics $Y_{l0}(\theta,\phi)$. Analogously, the wave function for an incoming plane wave e^{ikz} can be expanded as

$$\phi_{\mathbf{k}}(\mathbf{r}) = \sum_{l=0}^{\infty} i^l (2l+1) R_l(r) P_l(\cos(\theta)). \tag{8.4}$$

This is referred to as partial wave decomposition, and $R_l(r)$ must be determined to solve the scattering problem.

Often, Hankel functions

$$h_l^{(1)}(x) = j_l(x) + i n_l(x) \quad \text{and} \quad h_l^{(2)}(x) = j_l(x) - i n_l(x) \tag{8.5}$$

are used instead of Bessel and Neumann functions. While Bessel and Neumann functions describe standing waves, Hankel functions describe incoming and outgoing waves.

Thus, we can write $R_l(r)$ as the sum of an incoming and an outgoing wave

$$R_l(r) = C\left(h_l^{(2)}(kr) + S_l(E) h_l^{(1)}(kr)\right), \tag{8.6}$$

where C is a constant and $S_l(E)$ contains the information about the contribution of the l-th partial wave to the scattering process. $S_l(E)$ is a complex number that satisfies

$$|S_l(E)| = 1, \tag{8.7}$$

which allows us to define the scattering phase shift $\delta_l(E)$ via

$$S_l(E) = e^{2i\delta_l(E)}. \tag{8.8}$$

This implies that scattering shifts the phase of the wave function. If there is no scattering, i.e., for a vanishing potential $V(r) = 0$, $S_l(E) = 1$ and thus the scattering phase shift $\delta_l(E)$ is 0 or a multiple of π. This $S_l(E)$ is the single-channel analog to the S-matrix for multi-channel scattering, which contains the complete information about the scattering process. For an in-depth introduction to scattering theory, we refer to quantum mechanics

textbooks, e.g., [111–114].

In the following chapters, we will construct a multi-channel Schrödinger equation for a system of a static quark-antiquark pair in the presence of a light quark-antiquark pair and derive the corresponding S-matrix to study resonances of this system.

8.2 Quantum numbers

We consider two coupled channels, a confined quarkonium channel $\bar{Q}Q$ and an open meson-meson channel $\bar{M}M$. Unlike the first part of this work, where Q denoted a static quark, in this chapter and Chapter 9, Q represents a heavy quark with finite mass m_Q (typically a bottom quark with mass m_b), and M consists of one heavy quark and one light u/d quark. We restrict our system to isospin $I = 0$, i.e., $\bar{M}M = \bar{Q}Q(\bar{u}u + \bar{d}d)$.

In Chapter 8.6, we will introduce a third scattering channel $\bar{M}_s M_s = \bar{Q}Q\bar{s}s$, which will be included in our final computations. However, this additional channel does not conceptually alter our approach, so we derive the method more comprehensively with only two channels and extend it by the $\bar{M}_s M_s$ channel afterward.

We use the following quantum numbers to describe the quarkonium system with or without light quarks:

- J^{PC}: total angular momentum, parity, and charge conjugation.
- $S^{PC}_{q/Q}$: spin, parity, and charge conjugation of the heavy quarks Q or light quarks q.
- $\tilde{J}^{PC}$: total angular momentum, parity, and charge conjugation excluding the heavy quark spin S^{PC}_Q.

While J^{PC} and $S^{PC}_{q/Q}$ are standard quantum numbers, we explicitly define $\tilde{J}^{PC}$ because our observables will be independent of the heavy quark spin. This makes $\tilde{J}^{PC}$ the relevant quantum number for this work, rather than J^{PC} as usual. However, when comparing our results to experimental data, we must remember that $\tilde{J}^{PC}$ must be coupled with the heavy quark spins $S^{PC}_Q = 0^{-+}, 1^{--}$ to obtain J^{PC} (see Tab. 8.1).

A heavy-light meson M can have positive parity $P = +$ or negative parity $P = -$. A $P = +$ heavy-light meson has a mass approximately $400 - 500$ MeV higher than a negative parity one. Since low-lying states are generally more relevant, we restrict our approach to $\bar{M}M$ as a pair of two negative parity mesons. This allows us to study bound states below the energy threshold of $2m_M$ and resonances up to approximately $400 - 500$ MeV above.

Table 8.1: Possibilities to couple $\tilde{J}^{PC}$ with S^{PC}_Q to J^{PC}.

$\tilde{J}^{PC}$	S^{PC}_Q	J^{PC}
0^{++}	0^{-+}	0^{-+}
	1^{--}	1^{--}
1^{--}	0^{-+}	1^{+-}
	1^{--}	0^{++}, 1^{++}, 2^{++}
2^{++}	0^{-+}	2^{-+}
	1^{--}	1^{--}, 2^{--}, 3^{--}
...	...	...

8.3 Coupled channel Schroedinger equation

After these considerations, we obtain a four-component wave function $\psi(\mathbf{r}) = \left(\psi_{\bar{Q}Q}, \psi_{\bar{M}M}\right)$, where the first component corresponds to the quarkonium state, while the lower three components describe the spin-1 triplet of the $\bar{M}M$ system. The Schrödinger equation can be expressed as

$$\left(-\frac{1}{2}\mu^{-1}\left(\partial_r^2 + \frac{2}{r}\partial_r - \frac{\mathbf{L}^2}{r^2}\right) + V(\mathbf{r}) + \begin{pmatrix} E_{\text{threshold}} & 0 \\ 0 & 2m_M \end{pmatrix} - E\right)\psi(\mathbf{r}) = 0, \tag{8.9}$$

where $\mu^{-1} = \text{diag}(1/\mu_Q, 1/\mu_M, 1/\mu_M, 1/\mu_M)$ with the reduced mass of the heavy quark $\mu_Q = m_Q/2$ and meson $\mu_M = m_M/2$, and $\mathbf{L} = \mathbf{r} \times \mathbf{p}$ is the orbital angular momentum operator. The potential matrix is given in terms of the quarkonium potential $V_{\bar{Q}Q}$, the meson-meson potential $V_{\bar{M}M}$, and a mixing potential V_{mix} as

$$V(\mathbf{r}) = \begin{pmatrix} V_{\bar{Q}Q} & V_{\text{mix}}(r)\,(1 \otimes \mathbf{e}_r) \\ V_{\text{mix}}(r)\,(\mathbf{e}_r \otimes 1) & V_{\bar{M}M,\parallel}(r)\,(\mathbf{e}_r \otimes \mathbf{e}_r) + V_{\bar{M}M,\perp}(r)\,(1 - \mathbf{e}_r \otimes \mathbf{e}_r) \end{pmatrix}. \tag{8.10}$$

In the subsequent chapter, we will relate these potentials to static potentials computed from lattice QCD. The energy $E_{\text{threshold}}$ is added to the first component of the Schrödinger equation (8.9) to account for a difference between the light quark mass used in the lattice computation and the physical light quark mass.

8.4 Relating $V(r)$ to static potentials from lattice QCD

Two computations exist of static bottomonium potentials in the presence of a light quark pair. The first computation, as detailed in [72], considers two channels, a bottomonium channel and a meson-meson channel with u and d light quarks. This study provides data for the ground state potential $V_0(r)$ and one excited potential $V_1(r)$, along with information about the mixing of the two channels through a mixing angle θ. The second study [73, 74] includes a meson-meson state with s light quarks as a third scattering channel, extracting the second excited potential $V_2(r)$.

While the more recent computations [73, 74] are of higher quality, they do not provide the crucial information of mixing between the different channels in the form of a mixing angle. Therefore, we must use the lattice results from the first computation in this work [72]. However, it is clear that our predictions are limited by the quality of this lattice data, and improved data will be necessary to enhance our theoretical results.

Additionally, both studies suffer from another problem. The meson-meson operators used in the correlation matrix (see Eqn. (4.28)) should have the same quantum numbers as the quarkonium operator to extract excited states in the same sector, i.e., $\Lambda_\eta^\varepsilon = \Sigma_g^+$ (this notation is introduced in Section 4.3.2). However, the meson-meson operators chosen in these studies also overlap with additional sectors Σ_u^-, Π_g^+, and Π_g^-, causing contamination from these states. In [104], the results from the lattice study [72] were corrected by resampling the existing data and fitting additional exponential functions, considering all contributing sectors. In this work, unless stated otherwise, we will use these corrected potentials, which we will refer to as $V_0^{\Sigma_g^+}(r)$ and $V_1^{\Sigma_g^+}(r)$.

In [104], it is shown that $V_{\bar{Q}Q}(r)$, $V_{\bar{M}M}(r)$, and $V_{\text{mix}}(r)$ can be related to the ground state and first excited state static potentials $V_0^{\Sigma_g^+}(r)$ and $V_1^{\Sigma_g^+}(r)$ according to

$$V_{\bar{Q}Q}(r) = \cos^2(\theta(r))V_0^{\Sigma_g^+}(r) + \sin^2(\theta(r))V_1^{\Sigma_g^+}(r), \tag{8.11}$$

$$V_{\bar{M}M}(r) = \sin^2(\theta(r))V_0^{\Sigma_g^+}(r) + \cos^2(\theta(r))V_1^{\Sigma_g^+}(r), \tag{8.12}$$

$$V_{\text{mix}}(r) = \cos(\theta(r))\sin(\theta(r))\left(V_0^{\Sigma_g^+}(r) - V_1^{\Sigma_g^+}(r)\right). \tag{8.13}$$

If the system is predominantly in a quarkonium state, the mixing angle is small, while $\theta \approx \pi/2$ indicates a significant meson-meson contribution. For this work, we use the lattice results from [72]. The data is shown in Fig. 8.1 together with the parameterizations

$$V_{\bar{Q}Q}(r) = E_0 - \frac{\alpha}{r} + \sigma r + \sum_{j=1}^{2} c_{\bar{Q}Q,j}\, r \exp\left(-\frac{r^2}{2\lambda_{\bar{Q}Q,j}^2}\right), \tag{8.14}$$

$$V_{\bar{M}M,\parallel}(r) = 0, \tag{8.15}$$

$$V_{\text{mix}}(r) = \sum_{j=1}^{2} c_{\text{mix},j}\, r \exp\left(-\frac{r^2}{2\lambda_{\text{mix},j}^2}\right). \tag{8.16}$$

There is no lattice data available for $V_{\bar{M}M,\perp}(r)$. However, a reasonable assumption is $V_{\bar{M}M,\perp}(r) = V_0^{\Pi_g^\pm}(r)$, i.e., the ground state of the sectors Π_g^+ and Π_g^-, which are degenerate. As there is no string-like state present in this sector, it is reasonable to assume that this ground state energy is around twice the static-light meson mass, i.e.,

$$V_{\bar{M}M,\perp}(r) = V_0^{\Pi_g^\pm}(r) = 0. \tag{8.17}$$

Table 8.2: Parameters of the potential parameterizations (8.14) and (8.16).

potential	parameter	value
$V_{\bar{Q}Q}(r)$	E_0	$-1.599(269)$ GeV
	α	$+0.320(94)$
	σ	$+0.253(035)$ GeV^2
	$c_{\bar{Q}Q,1}$	$+0.826(882)$ GeV^2
	$\lambda_{\bar{Q}Q,1}$	$+0.964(47)$ GeV^{-1}
	$c_{\bar{Q}Q,2}$	$+0.174(1.004)$ GeV^2
	$\lambda_{\bar{Q}Q,2}$	$+2.663(425)$ GeV^{-1}
$V_{\text{mix}}(r)$	$c_{\text{mix},1}$	$-0.988(32)$ GeV^2
	$\lambda_{\text{mix},1}$	$+0.982(18)$ GeV^{-1}
	$c_{\text{mix},2}$	$-0.142(7)$ GeV^2
	$\lambda_{\text{mix},2}$	$+2.666(46)$ GeV^{-1}

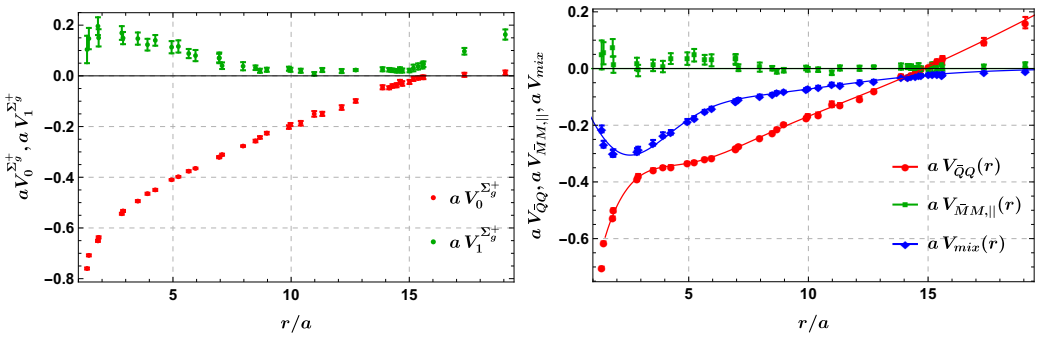

Figure 8.1: Data points for the static potential of the ground state $V_0^{\Sigma_g^+}(r)$ and the first excited state $V_1^{\Sigma_g^+}(r)$ with lattice spacing $a \approx 1/(2.37\text{ GeV})$, obtained by resampling and correcting the lattice results from [72] as discussed in [104] (left). Data points for $V_{\bar{Q}Q}(r)$, $V_{\bar{M}M}(r)$ and $V_{\text{mix}}(r)$ as a result of Eqns. (8.11)-(8.13) and their fitted parametrizations (8.14)-(8.16) (right).

8.5 Schrödinger equation for definite angular momentum $\tilde{J}$

We want to expand the Schrödinger equation (8.9) in terms of eigenfunctions of the angular momentum $\tilde{J}$ and then project it to definite $\tilde{J}$ afterward. This allows us to find bound states and resonances with definite quantum numbers $\tilde{J}^{PC}$, which can give insight into the angular momentum J^{PC} of states found by the experiment by comparing with our prediction.

Furthermore, the resulting Schrödinger equations become systems of coupled ordinary differential equations after the decomposition, which makes them much easier to solve numerically compared to the initial equation (8.9), a partial differential equation.

In [104], the Schrödinger equation (8.9) is derived and investigated for angular momentum $\tilde{J} = 0$. In this section, we generalize this procedure to arbitrary angular momentum.

8.5.1 Eigenbasis for angular momentum $\tilde{J}$

We want to find a suitable set of eigenfunctions to expand the wave function similarly to Eqn. (8.2). The first component of $\psi(\mathbf{r})$ is spinless, i.e. $\tilde{J} = L_{\bar{Q}Q}$. Thus, it can be expanded in terms of spherical harmonics $Y_{\tilde{J},\tilde{J}_z}(\Omega)$ according to

$$Z_{\bar{Q}Q,\tilde{J},\tilde{J}_z}(\Omega) = (Y_{\tilde{J},\tilde{J}_z}(\Omega),\mathbf{0}). \tag{8.18}$$

For the lower three components, eigenfunctions of $\tilde{\mathbf{J}}^2$ and $\tilde{J}_z$ can be constructed via Clebsch-Gordon coupling of the orbital angular momentum $L \equiv L_{\bar{M}M}$ and the three spin-1 components of the light quarks. Analogously to Eqn. (8.18) eigenfunctions of $\mathbf{L}^2$ and L_z can be represented by spherical harmonics $Y_{L,L_z}(\Omega)$. For the representation of the spin-1

components we use the Gell-Mann-matrices

$$S_x = \begin{pmatrix} 0 & 0 & 0 \\ 0 & 0 & -i \\ 0 & i & 0 \end{pmatrix}, \qquad S_y = \begin{pmatrix} 0 & 0 & i \\ 0 & 0 & 0 \\ -i & 0 & 0 \end{pmatrix}, \qquad S_z = \begin{pmatrix} 0 & 0-i & 0 \\ i & 0 & 0 \\ 0 & 0 & 0 \end{pmatrix}, \tag{8.19}$$

which fulfill the angular momentum algebra $[S_j,S_k] = i\varepsilon_{jkl}S_l$. Eigenfunctions of $\mathbf{S}^2$ and S_z are given by the eigenvectors of S_z

$$\mathbf{v}_{-1} = \frac{1}{\sqrt{2}} \begin{pmatrix} -1 \\ i \\ 0 \end{pmatrix}, \qquad \mathbf{v}_0 = \begin{pmatrix} 0 \\ 0 \\ 1 \end{pmatrix}, \qquad \mathbf{v}_1 = \frac{1}{\sqrt{2}} \begin{pmatrix} 1 \\ i \\ 0 \end{pmatrix}. \tag{8.20}$$

The orbital angular momentum and spin eigenfunctions can be coupled with Clebsch-Gordon coefficients

$$C^{\tilde{J},\tilde{J}_z}_{L,L_z;S,S_z} = \langle L,L_z;S,S_z|\tilde{J},\tilde{J}_z;L;S\rangle \tag{8.21}$$

to construct eigenfunctions of $\tilde{\mathbf{J}}^2$ and $\tilde{J}_z$ given by

$$Z_{\bar{M}M,L\to\tilde{J},\tilde{J}_z}(\Omega) = (0, \mathbf{Z}_{L\to\tilde{J},\tilde{J}_z}(\Omega)) \tag{8.22}$$

with

$$\mathbf{Z}_{L\to\tilde{J},\tilde{J}_z}(\Omega) = \sum_{j=-1}^{1} \sum_{L=\tilde{J}-1}^{\tilde{J}+1} C^{\tilde{J},\tilde{J}_z}_{L,j;1,-j} Y_{L,j}(\Omega)\mathbf{v}_{-j}. \tag{8.23}$$

With Eqn. (8.23) the eigenfunctions $\mathbf{Z}_{L\to\tilde{J},\tilde{J}_z}(\Omega)$ are straightforward to construct, e.g.,

$$\mathbf{Z}_{1\to0,0}(\Omega) = \sqrt{\frac{1}{4\pi}}\mathbf{e}_r, \tag{8.24}$$

$$\mathbf{Z}_{0\to1,j}(\Omega) = \sqrt{\frac{3}{8\pi}}\varepsilon_{jkl}\frac{r_k}{r}\mathbf{e}_l, \tag{8.25}$$

$$\mathbf{Z}_{2\to1,j}(\Omega) = \sqrt{\frac{9}{8\pi}}\left(\frac{r_j}{r}\mathbf{e}_r - \frac{1}{3}\mathbf{e}_j\right). \tag{8.26}$$

But in practice, we will stick to the general expression from Eqn. (8.23) to derive the Schrödinger equation for arbitrary angular momenta $\tilde{J}$. We can expand an arbitrary three-component function $\mathbf{G}(\mathbf{r})$ in terms of $\mathbf{Z}_{L\to\tilde{J},\tilde{J}_z}(\Omega)$ according to

$$\mathbf{G}(\mathbf{r}) = g_{1\to0,0}(r)\mathbf{Z}_{1\to0,0}(\Omega) + \sum_{\tilde{J}=1}^{\infty} \sum_{\tilde{J}_z=-\tilde{J}}^{\tilde{J}} \sum_{L=\tilde{J}-1}^{\tilde{J}+1} g_{L\to\tilde{J},\tilde{J}_z}(r)\mathbf{Z}_{L\to\tilde{J},\tilde{J}_z}(\Omega). \tag{8.27}$$

8.5.2 Partial wave decomposition

According to Eqn. (8.18) we can write down the partial wave decomposition of $\psi_{\bar{Q}Q}(\mathbf{r})$ as an expansion in spherical harmonics

$$\psi_{\bar{Q}Q}(\mathbf{r}) = \frac{u_{0,0}(r)}{kr} Y_{0,0}(\Omega) + \sum_{\tilde{J}=1}^{\infty} \sum_{\tilde{J}_z=-\tilde{J}}^{\tilde{J}} \frac{u_{\tilde{J},\tilde{J}_z}(r)}{kr} Y_{\tilde{J},\tilde{J}_z}(\Omega) \tag{8.28}$$

with expansion coefficients $u_{\tilde{J},\tilde{J}_z}(r)$.
Up to this point, we summarized the method from [104], now we have to tweak the next steps to be able to derive and solve the Schrödinger equation for arbitrary angular momentum $\tilde{J}$.
We write $\boldsymbol{\psi}_{\bar{M}M}(\mathbf{r})$ as a sum of incoming and emergent wave

$$\boldsymbol{\psi}_{\bar{M}M}(\mathbf{r}) = \mathbf{X}_{\text{in}}(\mathbf{r}) + \mathbf{X}_{\text{out}}(\mathbf{r}). \tag{8.29}$$

In contrast to [104], we do not assume a plane wave for the incoming part but a general solution of the Schrödinger equation $\mathbf{X}_{\text{in}}(\mathbf{r})$. We can write the radial part of these solutions as a linear combination of spherical Bessel and Neumann functions. However, we exclude a singular behavior at the origin, and thus, all factors of the Neumann function have to vanish. The expansion reads

$$\mathbf{X}_{\text{in}}(\mathbf{r}) = \alpha_{1\to 0,0} j_0(kr) \mathbf{Z}_{1\to 0,0}(\Omega) + \sum_{\tilde{J}=1}^{\infty} \sum_{\tilde{J}_z=-\tilde{J}}^{\tilde{J}} \sum_{L=\tilde{J}-1}^{\tilde{J}+1} \alpha_{L\to\tilde{J},\tilde{J}_z} j_L(kr) \mathbf{Z}_{L\to\tilde{J},\tilde{J}_z}(\Omega) \tag{8.30}$$

with the r-independent factor $\alpha_{L\to\tilde{J},\tilde{J}_z}$ fully determining the incoming wave. We expand the outgoing wave according to

$$\mathbf{X}_{\text{out}}(\mathbf{r}) = \frac{\chi_{1\to 0,0}(r)}{kr} \mathbf{Z}_{1\to 0,0}(\Omega) + \sum_{\tilde{J}=1}^{\infty} \sum_{\tilde{J}_z=-\tilde{J}}^{\tilde{J}} \sum_{L=\tilde{J}-1}^{\tilde{J}+1} \frac{\chi_{L\to\tilde{J},\tilde{J}_z}(r)}{kr} \mathbf{Z}_{L\to\tilde{J},\tilde{J}_z}(\Omega). \tag{8.31}$$

Since we want to project the Schrödinger equation to definite quantum numbers $J^{PC} = 1^{--}, 2^{++}, \ldots$ we can impose behavior under parity transformations upon $\psi(\mathbf{r})$. Our complete set of functions $\mathbf{Z}_{L\to\tilde{J},\tilde{J}_z}(\Omega)$ has parity $(-1)^{L+1}$. As a consequence, for parity even functions, the coefficients $\alpha_{L\to\tilde{J},\tilde{J}_z}$ and $\chi_{L\to\tilde{J},\tilde{J}_z}(r)$ with even L are zero, and for parity odd functions all coefficients with odd L are zero. A projection to definite $\tilde{J}, \tilde{J}_z$ leads to only two participating scattering channels $L = \tilde{J} - 1, \tilde{J} + 1$ for both incoming and outgoing waves.

8.5.3 Projection to definite angular momentum

To find the Schrödinger equation for a particular angular momentum $\tilde{J}$ we plug in the partial wave decomposition of $\psi(\mathbf{r}) = (\psi_{\bar{Q}Q}(\mathbf{r}), \boldsymbol{\psi}_{\bar{M}M}(\mathbf{r}))$ from Eqns. (8.28) and (8.29) into Eqn. (8.9), multiply it with the contributing $(Z_{\bar{Q}Q/\bar{M}M,\ldots})^\dagger$ from the left and perform the

solid angle integration $\int \mathrm{d}\Omega$. For a given $\tilde{J}$ there are three contributing basis functions $Z_{\bar{Q}Q/\bar{M}M,\ldots} \in \left\{ Z_{\bar{Q}Q,\tilde{J},\tilde{J}_z}(\Omega), Z_{\bar{M}M,\tilde{J}-1\to\tilde{J},\tilde{J}_z}(\Omega), Z_{\bar{M}M,\tilde{J}+1\to\tilde{J},\tilde{J}_z}(\Omega) \right\}$ which results in three coupled equations. These equations again can be written in a 3×3 matrix equation. The only term in the Schrödinger equation (8.9) that mixes channels is the potential matrix $V_{\tilde{J}}(r)$. All other terms are diagonal and thus the projection of these terms is trivial using the orthonormality of the eigenfunctions

$$\int \mathrm{d}\Omega \left(Z_{\bar{Q}Q,\tilde{J}_1,\tilde{J}_{z,1}}(\Omega) \right)^\dagger Z_{\bar{Q}Q,\tilde{J}_2,\tilde{J}_{z,2}}(\Omega) = \delta_{\tilde{J}_1,\tilde{J}_2} \delta_{\tilde{J}_{z,1}\tilde{J}_{z,2}}, \tag{8.32}$$

$$\int \mathrm{d}\Omega \left(Z_{\bar{M}M,L_1\to\tilde{J}_1,\tilde{J}_{z,1}}(\Omega) \right)^\dagger Z_{\bar{M}M,L_2\to\tilde{J}_2,\tilde{J}_{z,2}}(\Omega) = \delta_{L_1,L_2} \delta_{\tilde{J}_1,\tilde{J}_2} \delta_{\tilde{J}_{z,1}\tilde{J}_{z,2}}, \tag{8.33}$$

$$\int \mathrm{d}\Omega \left(Z_{\bar{Q}Q,\tilde{J}_1,\tilde{J}_{z,1}}(\Omega) \right)^\dagger Z_{\bar{M}M,L_2\to\tilde{J}_2,\tilde{J}_{z,2}}(\Omega) = 0. \tag{8.34}$$

The first matrix element of $V_{\tilde{J}}(r)$ is also trivially computed by using the orthonormality relation of spherical harmonics as

$$\int \mathrm{d}\Omega \begin{pmatrix} Y_{\tilde{J},0}(\Omega) \\ \mathbf{0} \end{pmatrix}^\dagger \cdot V(\mathbf{r}) \cdot \begin{pmatrix} Y_{\tilde{J},0}(\Omega) \\ \mathbf{0} \end{pmatrix} = V_{\bar{Q}Q}(r). \tag{8.35}$$

For the remaining elements of the first row of $V_{\tilde{J}}(r)$ we need to consider equations of the form

$$\int \mathrm{d}\Omega \begin{pmatrix} Y_{\tilde{J},0}(\Omega) \\ \mathbf{0} \end{pmatrix}^\dagger \cdot V(\mathbf{r}) \cdot Z_{\bar{M}M,\tilde{J}\pm1\to\tilde{J},0}(\Omega). \tag{8.36}$$

To do this, we rewrite the scalar product of $\mathbf{e}_r$ from the potential matrix (8.10) and $\mathbf{v}_{S_z}$ from the eigenvectors (see Eqn. (8.20)) of the spin operator S_z in terms of spherical harmonics, yielding

$$\mathbf{e}_r^T \cdot \mathbf{v}_{-1} = -\frac{1}{\sqrt{2}} \sin(\theta) \mathrm{e}^{-i\phi} = -2\sqrt{\frac{\pi}{3}} Y_{1,-1}(\Omega), \tag{8.37}$$

$$\mathbf{e}_r^T \cdot \mathbf{v}_0 = -\cos(\theta) = -2\sqrt{\frac{\pi}{3}} Y_{1,0}(\Omega), \tag{8.38}$$

$$\mathbf{e}_r^T \cdot \mathbf{v}_1 = \frac{1}{\sqrt{2}} \sin(\theta) \mathrm{e}^{i\phi} = -2\sqrt{\frac{\pi}{3}} Y_{1,1}(\Omega). \tag{8.39}$$

We are left with a solid angle integration over the product of three spherical harmonics, which can be solved using the relation

$$\int \mathrm{d}\Omega \, Y^*_{l_1,m_1}(\Omega) \, Y^*_{l_2,m_2}(\Omega) \, Y_{L,M}(\Omega) = \sqrt{\frac{(2l_1+1)(2l_2+1)}{4\pi(2L+1)}} \, \langle l_1,0; l_2,0 | L,0 \rangle \, \langle l_1,m_1; l_2,m_2 | L,M \rangle \, . \tag{8.40}$$

This leads to

$$\int \mathrm{d}\Omega \begin{pmatrix} Y_{\tilde{J},0}(\Omega) \\ \mathbf{0} \end{pmatrix}^{\dagger} \cdot V(\mathbf{r}) \cdot Z_{\bar{M}M,\bar{M}M,\tilde{J}\pm1\to\tilde{J},0}(\Omega) \tag{8.41}$$

$$\begin{aligned} =& -2\sqrt{\frac{\pi}{3}}\sqrt{\frac{3(2\tilde{J}+1\pm2)}{4\pi(2\tilde{J}+1)}}\,\langle \tilde{J}\pm1{,}0;1{,}0|\tilde{J}{,}0\rangle\,\langle \tilde{J}\pm1{,}-1;1{,}1|\tilde{J}{,}0\rangle\,\langle \tilde{J}\pm1{,}1;1{,}-1|\tilde{J}{,}0\rangle \\ & -2\sqrt{\frac{\pi}{3}}\sqrt{\frac{3(2\tilde{J}+1\pm2)}{4\pi(2\tilde{J}+1)}}\,\langle \tilde{J}\pm1{,}0;1{,}0|\tilde{J}{,}0\rangle\,\langle \tilde{J}\pm1{,}0;1{,}0|\tilde{J}{,}0\rangle\,\langle \tilde{J}\pm1{,}0;1{,}0|\tilde{J}{,}0\rangle \\ & -2\sqrt{\frac{\pi}{3}}\sqrt{\frac{3(2\tilde{J}+1\pm2)}{4\pi(2\tilde{J}+1)}}\,\langle \tilde{J}\pm1{,}0;1{,}0|\tilde{J}{,}0\rangle\,\langle \tilde{J}\pm1{,}1;1{,}-1|\tilde{J}{,}0\rangle\,\langle \tilde{J}\pm1{,}-1;1{,}1|\tilde{J}{,}0\rangle \\ =& \sqrt{\frac{\tilde{J}+\frac{1}{2}\pm\frac{1}{2}}{2\tilde{J}+1}}V_{\mathrm{mix}}(r). \end{aligned} \tag{8.42}$$

After projection with all three of these functions we obtain the 3×3 coupled channel Schrödinger equation

$$\begin{aligned} &\left(\frac{1}{2}\mu^{-1}\left(\partial_r^2+\frac{1}{r^2}L_{\tilde{J}}^2\right)+V_{\tilde{J}}(r)+\begin{pmatrix} E_{\mathrm{threshold}} & 0 & 0 \\ 0 & 2m_M & 0 \\ 0 & 0 & 2m_M \end{pmatrix}-E\right)\begin{pmatrix} u_{\tilde{J}}(r) \\ \chi_{\tilde{J}-1\to\tilde{J}}(r) \\ \chi_{\tilde{J}+1\to\tilde{J}}(r) \end{pmatrix} = \\ &\quad = \begin{pmatrix} V_{\mathrm{mix}}(r) \\ 0 \\ 0 \end{pmatrix}\left(\alpha_{\tilde{J}-1\to\tilde{J}}\frac{\tilde{J}}{2\tilde{J}+1}rj_{\tilde{J}-1}(kr)+\alpha_{\tilde{J}+1\to\tilde{J}}\frac{\tilde{J}+1}{2\tilde{J}+1}rj_{\tilde{J}+1}(kr)\right) \end{aligned} \tag{8.43}$$

with $\mu^{-1}=\mathrm{diag}(1/\mu_Q,1/\mu_M,1/\mu_M)$, $L_{\tilde{J}}^2=\mathrm{diag}(\tilde{J}(\tilde{J}+1),(\tilde{J}-1)\tilde{J},(\tilde{J}+1)(\tilde{J}+2),(\tilde{J}-1)\tilde{J},(\tilde{J}+1)(\tilde{J}+2))$ and

$$V_{\tilde{J}}(r)=\begin{pmatrix} V_{\bar{Q}Q}(r) & \sqrt{\frac{\tilde{J}}{2\tilde{J}+1}}V_{\mathrm{mix}}(r) & \sqrt{\frac{\tilde{J}+1}{2\tilde{J}+1}}V_{\mathrm{mix}}(r) \\ \sqrt{\frac{\tilde{J}}{2\tilde{J}+1}}V_{\mathrm{mix}}(r) & 0 & 0 \\ \sqrt{\frac{\tilde{J}+1}{2\tilde{J}+1}}V_{\mathrm{mix}}(r) & 0 & 0 \end{pmatrix}. \tag{8.44}$$

In the special case of $\tilde{J}=0$ there is of course no scattering channel corresponding to $\tilde{J}-1\to\tilde{J}$ but only $\tilde{J}+1\to\tilde{J}$. We retrieve the equations for $\tilde{J}=0$ by ignoring the second row and column from Eqn. (8.43) and the incoming wave proportional to $\alpha_{\tilde{J}-1\to\tilde{J}}$ on the right-hand side.

8.5.4 Boundary conditions

The quarkonium channel is confining, and thus, its wave function has to vanish for large distances. The boundary conditions are

$$u_{\tilde{J}}(r)\propto r^{\tilde{J}+1} \qquad \text{for} \quad r\to0, \tag{8.45}$$

$$u_{\tilde{J}}(r) = 0 \qquad \text{for} \quad r \to \infty. \tag{8.46}$$

The meson-meson wave function $\boldsymbol{\psi}_{\bar{M}M}(\mathbf{r})$ is a sum of an incoming and an emergent wave. The incoming wave is fully characterized by the choice of $\vec{\alpha} = \left(\alpha_{\tilde{J}-1\to\tilde{J}}, \alpha_{\tilde{J}-1\to\tilde{J}}\right)$ as a superposition of spherical Bessel functions $j_{L_{\text{in}}}(kr)$. If we choose $\vec{\alpha}_1 = (1,0)$ we obtain an incoming $\bar{M}M$ wave with $L_{\text{in}} = \tilde{J} - 1$ while $\vec{\alpha}_2 = (0,1)$ corresponds to an incoming wave with $L_{\text{in}} = \tilde{J} + 1$. To obtain full information about our scattering, we have to solve the system of coupled equations from Eqn. (8.43) twice, once with $\vec{\alpha} = \vec{\alpha}_1$ and once with $\vec{\alpha} = \vec{\alpha}_2$.

We choose the boundary conditions of the emergent waves to be

$$\chi_{L_{\text{out}}\to\tilde{J}}(r) \propto r^{L_{\text{out}}+1} \qquad \text{for} \quad r \to 0, \tag{8.47}$$

$$\chi_{L_{\text{out}}\to\tilde{J}}(r) = i t^{L_{\text{in}}}_{L_{\text{out}}} r h^{(1)}_{L_{\text{out}}}(kr) \qquad \text{for} \quad r \to \infty \tag{8.48}$$

with $L_{\text{in}} \in \tilde{J} - 1, \tilde{J} + 1$ corresponding to $\vec{\alpha}_1$ and $\vec{\alpha}_2$, the scattering amplitude $t^{L_{\text{in}}}_{L_{\text{out}}}$ (L_{in} is an upper index and not an exponent) and $h^{(1)}_{L_{\text{out}}}(kr)$ denoting a spherical Hankel function of the first kind.

8.5.5 T-matrix

We can use the four different scattering amplitudes $t^{L_{\text{in}}}_{L_{\text{out}}}$ from Eqn. (8.48) to construct the $\mathrm{T}_{\tilde{J}}$-matrix of our scattering problem,

$$\mathrm{T}_{\tilde{J}} = \begin{pmatrix} t^{\tilde{J}-1}_{\tilde{J}-1} & t^{\tilde{J}+1}_{\tilde{J}-1} \\ t^{\tilde{J}-1}_{\tilde{J}+1} & t^{\tilde{J}+1}_{\tilde{J}+1} \end{pmatrix}, \tag{8.49}$$

which includes all the information of the scattering. We recover the special case of $\tilde{J} = 0$ discussed in [104] by dropping the components with $L_{\text{in}} = \tilde{J} - 1$ and $L_{\text{out}} = \tilde{J} - 1$ which leaves us with just one scattering amplitude $\mathrm{T}_{\tilde{J}} = t^{\tilde{J}+1}_{\tilde{J}+1}$.
The corresponding S-Matrix $\mathrm{S}_{\tilde{J}}$ is given by

$$\mathrm{S}_{\tilde{J}} = 1 + 2i\mathrm{T}_{\tilde{J}}. \tag{8.50}$$

Another important quantity is the phase shift. For a scalar scattering matrix, i.e. with $\tilde{J} = 0$, it is defined by $\mathrm{S}_{\tilde{J}} = \exp\left(2i\delta_{\tilde{J}}\right)$ consistent with Eqn. (8.8). However, if the $\mathrm{S}_{\tilde{J}}$ is a 2×2 matrix there are two phase shifts defined via the eigenvalues $\lambda_{\tilde{J},i} = \exp\left(2i\delta_{\tilde{J},i}\right)$. We define the eigenphase sum [115–117] as

$$\det\left(\mathrm{S}_{\tilde{J}}\right) = \exp\left(2i\delta_{\tilde{J}}\right), \tag{8.51}$$

which is the sum of all phaseshifts $\delta_{\tilde{J},i}$. While this quantity is not the same as the scattering phase shift, it has properties similar to $\delta_{\tilde{J},i}$ while remaining one number, even for systems with many channels.

8.6 Extension by a $\bar{M}_s M_s$ channel

We now extend our system by incorporating an $\bar{M}_s M_s$ channel. This extension is crucial for accurately describing the energy region of interest. To illustrate this, consider the $\bar{Q}Q = \bar{b}b$ and $\bar{M}M = \bar{B}^{(*)}B^{(*)}$ channels. Our current method allows us to identify bound states below the $\bar{B}^{(*)}B^{(*)}$ threshold, which is approximately 10.628 GeV (calculated using the average mass of the four possible spin configurations $m_M = (m_B + 3m_{B^*})/4 = 5.313$ GeV). Additionally, we can identify resonances up to the threshold of a meson with negative parity and another with positive parity at 11.025 GeV. However, the threshold for a $\bar{b}b\bar{s}s$ meson-meson state is at 10.807 GeV (with $m_{M_s} = (m_{B_s} + 3m_{B_s^*})/4 = 5.403$ GeV). This indicates that results above this energy are questionable if only the $\bar{b}b$ and $\bar{B}^{(*)}B^{(*)}$ channels are considered. This energy region is particularly significant for studying the $\Upsilon(10860)$ and $\Upsilon(11020)$ resonances observed experimentally. Therefore, we extend our coupled-channel system to include the $\bar{M}_s M_s$ channel.

Ideally, we would utilize static potentials from a lattice study with a 3×3 correlation matrix that includes a $\bar{M}_s M_s$ operator. Such a correlation matrix was computed in [73], but the results are unsuitable for our method, as discussed in Section 8.4.

Consequently, we construct the $\bar{M}_s M_s$ channel using the same lattice data employed for the $\bar{M}M$ channel. This approach is reasonable because the quark mass used in the lattice study is closer to the physical s quark mass than to the u/d quark mass. We extend the potential matrix from Eqn. (8.10) from two channels to three channels,

$$\begin{pmatrix} V_{\bar{Q}Q}(r) & V_{\text{mix}}(r) \\ V_{\text{mix}}(r) & 0 \end{pmatrix} \to \begin{pmatrix} V_{\bar{Q}Q}(r) & V_{\text{mix}}(r) & 1/\sqrt{2}\, V_{\text{mix}}(r) \\ V_{\text{mix}}(r) & 0 & 0 \\ 1/\sqrt{2}\, V_{\text{mix}}(r) & 0 & 0 \end{pmatrix}, \tag{8.52}$$

where we assume no mixing between the two different meson-meson channels. The mixing between $\bar{M}_s M_s$ and $\bar{Q}Q$ is reduced by a factor of $1/\sqrt{2}$ compared to the mixing between $\bar{M}M$ and $\bar{Q}Q$ due to the different number of degenerate flavors (one for $\bar{M}_s M_s$ and two for $\bar{M}M$).

To test the validity of this extension, we solve the eigenvalue problem of the 3×3 equation to extract the first three energy levels of the system. In Fig. 8.2, we present the resulting energies E_1, E_2, E_3 as a function of the separation r. The shape of these potentials is generally consistent with the energies obtained in the lattice study of a 3×3 correlation function that includes a $\bar{M}_s M_s$ operator [73].

8.6.1 5x5 coupled channel Schrödinger equation

To derive the corresponding Schrödinger equation, we follow the same steps as in the previous section. The only difference is adding a fourth and fifth component to the wave function $\psi(\mathbf{r})$ corresponding to a $\tilde{J}-1$ and $\tilde{J}+1$ $\bar{M}_s M_s$ channel. Thus, the 3×3 Schrödinger

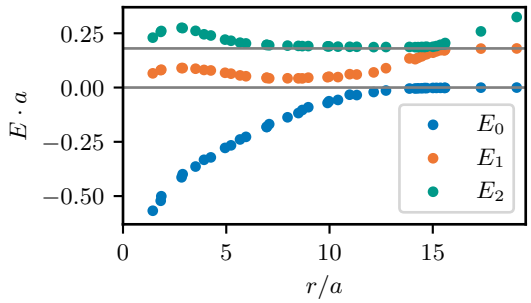

Figure 8.2: Energy eigenvalues E_1, E_2, E_3 as a function of the separation r/a for the 3×3 potential matrix from Eqn. (8.52) with lattice spacing $a \approx 1/(2.37\ \text{GeV})$. The two gray lines mark 0 and the difference of the $\bar{M}_s M_s$ and $\bar{M}M$ threshold $2m_{M_s} - 2m_M$.

equation (8.9) expands to the 5×5 equation

$$\left(\frac{1}{2}\mu^{-1}\left(\partial_r^2 + \frac{1}{r^2}L_{\tilde{J}}^2\right) + V_{\tilde{J}}(r) + M - E\right)\begin{pmatrix} u_{\tilde{J}}(r) \\ \chi_{\bar{M}M,\tilde{J}-1\to\tilde{J}}(r) \\ \chi_{\bar{M}M,\tilde{J}+1\to\tilde{J}}(r) \\ \chi_{\bar{M}_sM_s,\tilde{J}-1\to\tilde{J}}(r) \\ \chi_{\bar{M}_sM_s,\tilde{J}+1\to\tilde{J}}(r) \end{pmatrix} =$$

$$= \begin{pmatrix} V_{\text{mix}}(r) \\ 0 \\ 0 \\ 0 \\ 0 \end{pmatrix}\left(\alpha_{\bar{M}M,\tilde{J}-1}\frac{\tilde{J}}{2\tilde{J}+1}rj_{\tilde{J}-1}(kr) + \alpha_{\bar{M}M,\tilde{J}+1}\frac{\tilde{J}+1}{2\tilde{J}+1}rj_{\tilde{J}+1}(kr)\right.$$

$$\left. + \alpha_{\bar{M}_sM_s,\tilde{J}-1}\frac{\tilde{J}}{2\tilde{J}+1}\frac{rj_{\tilde{J}-1}(k_sr)}{\sqrt{2}} + \alpha_{\bar{M}_sM_s,\tilde{J}+1}\frac{\tilde{J}+1}{2\tilde{J}+1}\frac{rj_{\tilde{J}+1}(k_sr)}{\sqrt{2}}\right) \tag{8.53}$$

with $\mu^{-1} = \text{diag}(1/\mu_Q, 1/\mu_M, 1/\mu_M, 1/\mu_{M_s}, 1/\mu_{M_s})$,
$L_{\tilde{J}}^2 = \text{diag}(\tilde{J}(\tilde{J}+1), (\tilde{J}-1)\tilde{J}, (\tilde{J}+1)(\tilde{J}+2), (\tilde{J}-1)\tilde{J}, (\tilde{J}+1)(\tilde{J}+2))$,
$M = \text{diag}(E_{\text{threshold}}, 2m_M, 2m_M, 2m_{M_s}, 2m_{M_s})$ and

$$V_{\tilde{J}}(r) = \begin{pmatrix} V_{\bar{Q}Q} & \sqrt{\frac{\tilde{J}}{2\tilde{J}+1}}V_{\text{mix}} & \sqrt{\frac{\tilde{J}+1}{2\tilde{J}+1}}V_{\text{mix}} & \sqrt{\frac{\tilde{J}}{4\tilde{J}+2}}V_{\text{mix}} & \sqrt{\frac{\tilde{J}+1}{4\tilde{J}+2}}V_{\text{mix}} \\ \sqrt{\frac{\tilde{J}}{2\tilde{J}+1}}V_{\text{mix}} & 0 & 0 & 0 & 0 \\ \sqrt{\frac{\tilde{J}+1}{2\tilde{J}+1}}V_{\text{mix}} & 0 & 0 & 0 & 0 \\ \sqrt{\frac{\tilde{J}}{4\tilde{J}+2}}V_{\text{mix}} & 0 & 0 & 0 & 0 \\ \sqrt{\frac{\tilde{J}+1}{4\tilde{J}+2}}V_{\text{mix}} & 0 & 0 & 0 & 0 \end{pmatrix}. \tag{8.54}$$

The different momenta of the incoming waves are denoted by k and k_s for the $\bar{M}M$ and $\bar{M}_sM_s$ channel respectively. They are related to the energy E by

$$E = 2m_M + \frac{k^2}{2\mu_M}, \qquad E = 2m_{M_s} + \frac{k_s^2}{2\mu_{M_s}}. \tag{8.55}$$

With four open channels the incoming wave also has four degrees of freedom denoted by $\alpha = (\alpha_{\bar{M}M,\tilde{J}-1},\alpha_{\bar{M}M,\tilde{J}+1},\alpha_{\bar{M}_sM_s,\tilde{J}-1},\alpha_{\bar{M}_sM_s,\tilde{J}+1})$. Thus, we have to solve the system of coupled equations (8.53) four times, once for each of the four possible incoming waves. The emergent waves are denoted by $\chi_{\bar{M}_{(s)}M_{(s)},\tilde{J}-1\to\tilde{J}}$ and $\chi_{\bar{M}_{(s)}M_{(s)},\tilde{J}+1\to\tilde{J}}$ with $\bar{M}_{(s)}M_{(s)} \in \{\bar{M}M, \bar{M}_sM_s\}$. The boundary conditions for the emergent waves must also be extended for the $\bar{M}_sM_s$ channels. For the quarkonium channel Eqn. (8.46) remains unchanged while for the meson-meson channels we now demand

$$\chi_{\bar{M}M(\bar{M}_sM_s),L_{\text{out}}\to\tilde{J}}(r) \propto r^{L_{\text{out}}+1} \qquad \text{for} \quad r \to 0, \tag{8.56}$$

$$\chi_{\bar{M}M,L_{\text{out}}\to\tilde{J}} = it^{\bar{M}_{(s)}M_{(s)},L_{\text{in}}}_{\bar{M}M,L_{\text{out}}} r h^{(1)}_{L_{\text{out}}}(kr) \qquad \text{for} \quad r \to \infty, \tag{8.57}$$

$$\chi_{\bar{M}_sM_s,L_{\text{out}}\to\tilde{J}} = it^{\bar{M}_{(s)}M_{(s)},L_{\text{in}}}_{\bar{M}_sM_s,L_{\text{out}}} r h^{(1)}_{L_{\text{out}}}(k_sr) \qquad \text{for} \quad r \to \infty. \tag{8.58}$$

8.6.2 4x4 T-matrix

The $\mathrm{T}_{\tilde{J}}$-matrix is now a 4×4 matrix with the following components

$$\mathrm{T}_{\tilde{J}} = \begin{pmatrix} t^{\bar{M}M,\tilde{J}-1}_{\bar{M}M,\tilde{J}-1} & t^{\bar{M}M,\tilde{J}+1}_{\bar{M}M,\tilde{J}-1} & t^{\bar{M}_sM_s,\tilde{J}-1}_{\bar{M}M,\tilde{J}-1} & t^{\bar{M}_sM_s,\tilde{J}+1}_{\bar{M}M,\tilde{J}-1} \\ t^{\bar{M}M,\tilde{J}-1}_{\bar{M}M,\tilde{J}+1} & t^{\bar{M}M,\tilde{J}+1}_{\bar{M}M,\tilde{J}+1} & t^{\bar{M}_sM_s,\tilde{J}-1}_{\bar{M}M,\tilde{J}+1} & t^{\bar{M}_sM_s,\tilde{J}+1}_{\bar{M}M,\tilde{J}+1} \\ t^{\bar{M}M,\tilde{J}-1}_{\bar{M}_sM_s,\tilde{J}-1} & t^{\bar{M}M,\tilde{J}+1}_{\bar{M}_sM_s,\tilde{J}-1} & t^{\bar{M}_sM_s,\tilde{J}-1}_{\bar{M}_sM_s,\tilde{J}-1} & t^{\bar{M}_sM_s,\tilde{J}+1}_{\bar{M}_sM_s,\tilde{J}-1} \\ t^{\bar{M}M,\tilde{J}-1}_{\bar{M}_sM_s,\tilde{J}+1} & t^{\bar{M}M,\tilde{J}+1}_{\bar{M}_sM_s,\tilde{J}+1} & t^{\bar{M}_sM_s,\tilde{J}-1}_{\bar{M}_sM_s,\tilde{J}+1} & t^{\bar{M}_sM_s,\tilde{J}+1}_{\bar{M}_sM_s,\tilde{J}+1} \end{pmatrix}. \tag{8.59}$$

$\mathrm{S}_{\tilde{J}}$ and the eigenphase sum are defined analogously to the 2x2 case (i.e. Eqns. (8.50) and (8.51)).

8.7 Quarkonium and meson-meson content

By construction the components of the wave function $\psi(\mathbf{r})$ correspond to the $\bar{Q}Q$, $\bar{M}M$ and $\bar{M}_sM_s$ channels of the system. We can investigate the nature of a resonance or bound state by considering the distribution of the wave function coefficients. To do so in a rigorous way we define

$$\%\bar{Q}Q = \frac{Q}{Q + M_{\tilde{J}-1} + M_{\tilde{J}+1} + M_{s,\tilde{J}-1} + M_{s,\tilde{J}+1}}, \tag{8.60}$$

$$(\%\bar{M}M)_{L_{\text{out}}} = \frac{M_{L_{\text{out}}}}{Q + M_{\tilde{J}-1} + M_{\tilde{J}+1} + M_{s,\tilde{J}-1} + M_{s,\tilde{J}+1}}, \tag{8.61}$$

$$(\%\bar{M}_sM_s)_{L_{\text{out}}} = \frac{M_{s,L_{\text{out}}}}{Q + M_{\tilde{J}-1} + M_{\tilde{J}+1} + M_{s,\tilde{J}-1} + M_{s,\tilde{J}+1}}. \tag{8.62}$$

where

$$Q = \int_0^{R_{\max}} \mathrm{d}r \left| u_{\tilde{J}}(r) \right|^2, \tag{8.63}$$

$$M_{L_{\mathrm{out}}} = \int_0^{R_{\max}} \mathrm{d}r \left| \chi_{\bar{M}M, L_{\mathrm{out}} \to \tilde{J}}(r) \right|^2, \tag{8.64}$$

$$M_{s, L_{\mathrm{out}}} = \int_0^{R_{\max}} \mathrm{d}r \left| \chi_{\bar{M}_s M_s, L_{\mathrm{out}} \to \tilde{J}}(r) \right|^2. \tag{8.65}$$

$R_{\max}$ is the maximum distance we integrate to. For bound states Q, $M_{L_{\mathrm{out}}}$ and $M_{s,L_{\mathrm{out}}}$ approach constant values for a finite $R_{\max} \approx 2.0$ fm while for resonances they proceed to change slowly for larger $R_{\max}$ and a reasonable cutoff has to be applied.

CHAPTER 9

Results for bottomonium resonances in the Born-Oppenheimer approximation using lattice QCD static potentials

In this chapter, we present our findings on bottomonium resonances in the S, P, D, and F waves using lattice QCD static potentials from [72] within the framework introduced in the previous chapter, solving a Schrödinger equation in the Born-Oppenheimer approximation.

We commence this chapter by presenting our numerical methods to solve the Schrödinger equation and determine bound and resonance states. Then, we specify the parameters relevant to the bottomonium system under investigation. Subsequently, we provide results for scattering phase shifts and pole positions in the complex plane. We then compare our theoretical predictions for bound states and resonances with existing experimental data. Additionally, we analyze the quarkonium and meson-meson content of each state. Finally, we discuss the systematic errors associated with our results and compare them with other theoretical predictions.

9.1 Numerical solution

To solve the system of coupled differential equations (8.53) for a given energy E, we employed two independent methods, both of which are standard numerical techniques.

Initially, we replace the asymptotic boundary condition $r \to \infty$ with $r \leq R$, where R is sufficiently large. Subsequently, we discretize the interval $[0, R]$ using a uniform one-dimensional lattice with $N + 1$ lattice points and lattice spacing $d = R/N$.

This allows us to rewrite Eqn. (8.53) in terms of a system of linear equations, which can be solved using standard methods. Alternatively, we can solve it using a Runge-Kutta algorithm combined with the shooting method. We recommend this approach and will discuss finding bound states and resonances using a 4th-order Runge-Kutta algorithm with a shooting method and a Newton-Raphson root finder.

9.1.1 Determination of bound state energies

There is no emergent wave for bound states; thus, the right-hand side of Eqn. (8.9) vanishes. The resulting homogeneous differential equation must be solved repeatedly using the shooting method. We start with trial energy E and integrate the differential equation from a very small separation ε to a large distance R. We choose four different initial conditions corresponding to Eqns. (8.46) and (8.56), one for each of the four possible incoming waves. This yields four resulting wave functions $\psi_i^{\text{hom}}(R)$ at large distance R, which we combine into a 4×4 matrix $M = \big(\psi_1^{\text{hom}}(R), \psi_2^{\text{hom}}(R), \psi_3^{\text{hom}}(R), \psi_4^{\text{hom}}(R)\big)$. We then find the roots of $\det(M)$ as a function of the energy E by employing the Newton-Raphson method and

repeatedly integrating. The energies that minimize $\det(M)$ correspond to vanishing wave functions at large separations and thus fulfill the boundary conditions of bound states.

9.1.2 Numerical methods to compute the eigenphase sum $\delta_{\tilde{J}}(E)$ and find poles of $\mathrm{T}(E)$ in the complex plane

For resonances, the right-hand side of Eqn. (8.9) does not vanish, leading to non-trivial behavior at large distances. According to the boundary condition from Eqn. (8.58), we need to match the behavior of the wave functions at large separations to the corresponding elements of the T-matrix (8.59), which appear as factors in the asymptotic behavior of the wave function $it^{\bar{M}_{(s)}M_{(s)},L_{\text{in}}}_{\bar{M}_{(s)}M_{(s)},L_{\text{out}}} r h^{(1)}_{L_{\text{out}}}(k_{(s)}r)$ from Eqns. (8.56) to (8.58). This allows us to compute the eigenphase sum (8.51) $\delta_{\tilde{J}}(E)$ for real energies E.

We can also analytically continue the scattering problem to the complex plane and search for poles in the $\mathrm{T}(E)$-matrix for complex energies E, which directly correspond to the mass and decay width of resonances according to

$$m = \mathrm{Re}(E_{\text{pole}}), \quad \Gamma = -2\mathrm{Im}(E_{\text{pole}}). \tag{9.1}$$

We apply a Newton-Raphson root-finding algorithm to $1/\det(\mathrm{T}(E))$ to extract the resonance positions. This numerical task involves finding a root in the complex plane for an essentially unknown, highly unpredictable function. This constitutes the main numerical challenge in this chapter of the work. The following section discusses the technical difficulties of the pole search in the complex plane.

9.1.3 Technical difficulties of finding poles in the complex plane

Finding poles in the complex plane is essentially a root-finding problem in two dimensions, which is inherently complex. We employ a Newton-Raphson shooting algorithm for locating poles, which necessitates an initial guess for the energy. The algorithm then iteratively follows the gradient to identify a root of $1/\det(\mathrm{T}(E))$. The $\mathrm{T}(E)$-matrix spans multiple orders of magnitude, and its poles can be extremely narrow relative to the energy scale, making the initial guess critical.

A practical approach is to perform an energy scan, i.e., compute $\mathrm{T}(E)$ as a function of

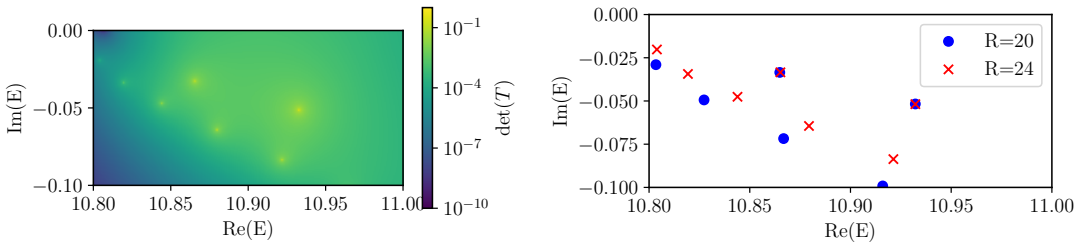

Figure 9.1: Left: $\mathrm{Det}(\mathrm{T}(E))$ in the complex energy plane for $\tilde{J} = 1$. Yellow dots indicate poles in the T matrix. Right: Poles found in the complex plane for $\tilde{J} = 1$ for integration distance $R = 20$ and $R = 24$. Unphysical "spurious" poles depend on R, while the two physical poles remain at the same position.

complex energy, and visualize it using a heatmap, as illustrated on the left side of Fig. 9.1. This visualization helps identify approximate pole positions, which can be refined using the Newton-Raphson method. Another strategy involves conducting the pole search for a dense grid of initial energies, effectively scanning the relevant region in the complex plane. For instance, to generate Fig. 9.1, we used a grid of $40 \times 40 = 1600$ initial energies within the range $10.800\ \text{GeV} - 0i\ \text{GeV}$ to $11.000\ \text{GeV} - 0.10i\ \text{GeV}$.

A significant challenge in this procedure is the emergence of unphysical poles, which we call "spurious poles". These poles are discretization artifacts influenced by the integration distance R and the step size h. To distinguish physical poles from spurious ones, we recompute the poles with varying R or h and observe any energy changes. In Fig. 9.1, we present an example where poles are computed above the $\bar{B}_s B_s$ threshold for integration distances $R = 20$ fm and $R = 24$ fm. The spurious poles exhibit significant shifts into the complex plane when R is increased from 20 fm to 24 fm, whereas the two physical poles at approximately $10.865\ \text{GeV} - i0.34\ \text{GeV}$ and $10.932\ \text{GeV} - i0.50\ \text{GeV}$ remain stable.

9.2 Parameter setting

In Chapter 8, we kept the heavy quark flavor in the system general. From this point onward, we focus on bottomonium, i.e., $Q = b$. We do not differentiate between different heavy quark spins, thus treating the $B_{(s)}$ and $B^*_{(s)}$ mesons as degenerate. Consequently, the heavy meson masses are chosen as the average over the masses of the four possible spin configurations, $m_{M_{(s)}} = (m_{B_{(s)}} + 3m_{B^*_{(s)}})/4 = 5.313\ \text{GeV}(5.403\ \text{GeV})$ (1 for spin 0 and 3 for spin 1). Thus, when we refer to $B_{(s)}$ mesons in this chapter, it, in principle, refers to both $B_{(s)}$ and $B^*_{(s)}$ mesons.

For the lattice data, we utilize the results from the study of string breaking [72], which employed an unphysical light quark mass corresponding to $m_\pi = 640$ MeV. Our equations account for this by setting $E_{\text{threshold}}$ to 10.790 GeV. Note that this value is much closer to the $\bar{B}_s B_s$ threshold than the $\bar{B}B$ threshold.

9.3 Eigenphase sum and pole positions in the complex plane

Fig. 9.2 presents the eigenphase sum as a function of energy for angular momenta $\tilde{J} \leq 3$. Resonances are identified by pronounced steps in $\delta_{\tilde{J}}(E)$. These steps can typically be parameterized by

$$\alpha + \beta \arctan\left(\frac{2}{\Gamma}(E - m)\right), \tag{9.2}$$

where m denotes the resonance mass, Γ represents the decay width, and α and β are additional fitting parameters.

However, particularly for broad resonances with large decay widths, the step in the eigenphase sum is not as pronounced as for narrow resonances. Additionally, overlapping resonances can obscure the identification of individual poles. To identify resonances reliably, we utilize the positions of T matrix poles in the complex plane by analytically continuing the scattering problem.

In Fig. 9.3, we present the positions of T matrix poles in the complex plane for angular

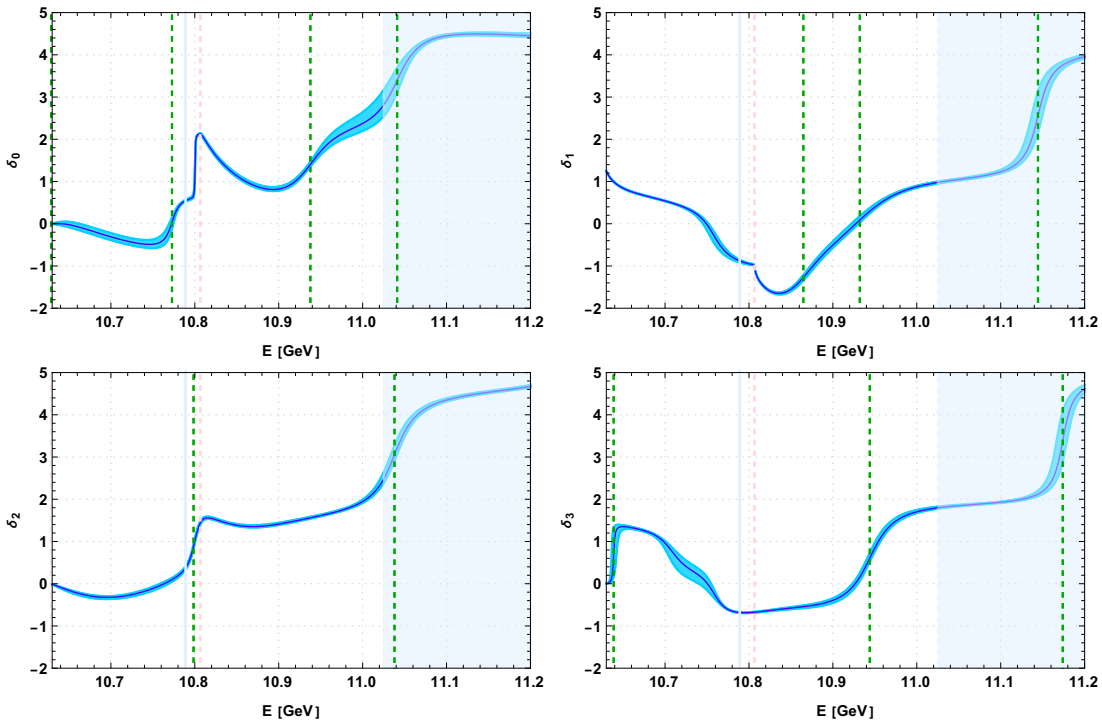

Figure 9.2: Eigenphase sum $\delta_{\tilde{J}}$ from Eqn. (8.51) for $\tilde{J} = 0,1,2,3$. The vertical red dashed line indicates the $\bar{B}_s B_s$ threshold at 10.808 GeV, while vertical green dashed lines indicate pole positions. The light blue background marks the region where the validity of our results is questionable due to the opening of a new scattering threshold.

momenta $\tilde{J} \leq 3$. Bound states on the real axis below the $\bar{B}B$ threshold are also included in the plot, while resonances appear above this threshold with non-zero imaginary parts. We employed resampling on the lattice data, leading to different fitting parameters from Tab. 8.2, to generate approximately 1000 data points for each pole position, represented by the colored point clouds. Different colors are used to distinguish between the poles. The error bars on the mean values, indicated by the black points, correspond to the 16th and 84th percentiles.

An exception is the T matrix pole for $n = 3$ and $\tilde{J} = 2$, which could not be identified by the pole-finding algorithm but is clearly indicated in the eigenphase sum δ_2. For this resonance, we instead fit Eqn. (9.2) to δ_2 to extract the mass m and decay width Γ. The resulting fit curve is shown in Fig. 9.4.

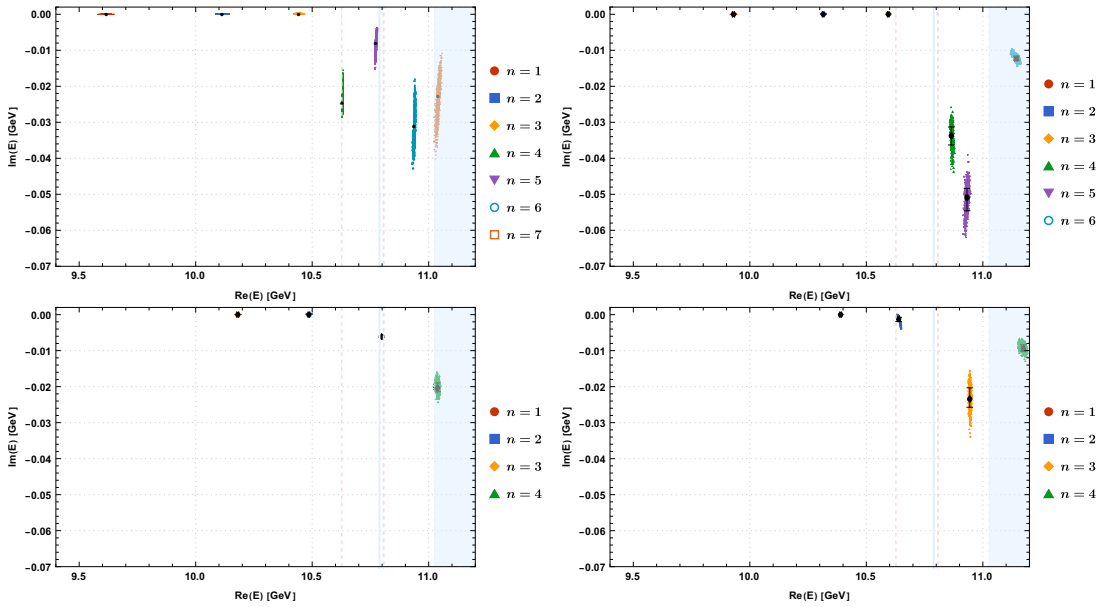

Figure 9.3: Bound state and resonance pole positions in the complex energy plane for angular momenta $\tilde{J} = 0,1,2,3$ (left to right, top to bottom). Colored point clouds indicate results with ≈ 1000 resampled parameter sets, and error bars are defined by the 16th and 84th percentile. Red dotted lines mark the $\bar{B}B$ and $\bar{B}_s B_s$ thresholds at 10.628 GeV and 10.808 GeV. The light blue region indicates the threshold of one negative and one positive parity meson, where our results are no longer reliable.

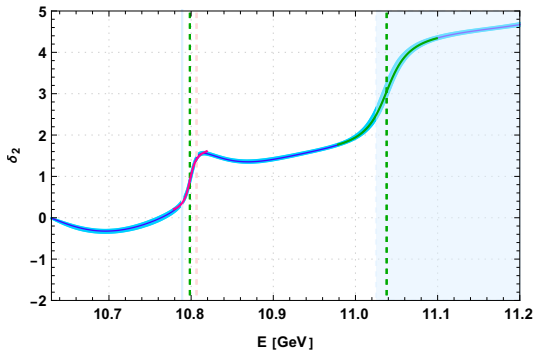

Figure 9.4: Eigenphase sum for $\bar{B}B$, $\tilde{J} = 2$. The resonance at ≈ 10.800 GeV is fitted (pink curve) with the ansatz from Eqn. (9.2) to determine the resonance mass m and decay width Γ.

9.4 Percentages of quarkonium and meson-meson composition

We also investigate the composition and internal structure of bound states and resonances to determine whether they are traditional quarkonia or contain significant contributions from $\bar{M}_{(s)}M_{(s)}$ components. As defined in Eqn. (8.62), we calculate the percentage of quarkonium and meson-meson composition for each state, i.e., $\%\bar{Q}Q$, $(\%\bar{M}M)_{L_{\text{out}}}$, and $(\%\bar{M}_sM_s)_{L_{\text{out}}}$.

For a bound state, Q, $M_{L_{\text{out}}}$, and $M_{s,L_{\text{out}}}$ approach constants for $R_{\text{max}} \approx 2.0$ fm as indicated in Fig. 9.5 (corresponding figures for $\tilde{J} = 1,2,3$ are provided in Appendix C.1, Figs. C.1-C.3). We collect the asymptotic values of $\%\bar{Q}Q$, $(\%\bar{M}M)_{L_{\text{out}}}$, and $(\%\bar{M}_sM_s)_{L_{\text{out}}}$ for bound states in Tab. 9.1.

Examining the dependence of Q, $M_{L_{\text{out}}}$, and $M_{s,L_{\text{out}}}$ on R_{max} in Fig. 9.5, we observe that the curves do not reach an asymptotic value for large R_{max} but instead exhibit an approximate linear behavior with a small slope in the range 1.8 fm $< R_{\text{max}} <$ 3.0 fm. Specifically, the meson content, i.e., $M_{L_{\text{out}}}$ and $M_{s,L_{\text{out}}}$, increases in this region. In contrast, the quarkonium content decreases due to the emergent spherical waves $\chi_{\bar{M}M,L_{\text{out}}\to\tilde{J}}(r)$ and $\chi_{\bar{M}_sM_s,L_{\text{out}}\to\tilde{J}}(r)$. At the distance where the curves behave linearly, the quarkonium component becomes negligibly small, i.e., a nearly pure emergent wave and the resonance is contained within a sphere of R_{max}. To define $\%\bar{Q}Q$, $(\%\bar{M}M)_{L_{\text{out}}}$, and $(\%\bar{M}_sM_s)_{L_{\text{out}}}$ in a meaningful way while accounting for systematic uncertainty, we compute $\%\bar{Q}Q$, $(\%\bar{M}M)_{L_{\text{out}}}$, and $(\%\bar{M}_sM_s)_{L_{\text{out}}}$ at the center of this region at $R_{\text{max}} = 2.4$ fm and use the values at the borders $R_{\text{max}} = 1.8$ fm and $R_{\text{max}} = 3.0$ fm to estimate the systematic error. We present these results in Tab. 9.1.

Most bound states are dominated by a substantial quarkonium content $\%\bar{Q}Q$ ranging from 74% to 84%. One might expect even higher values for this content. Still, the non-vanishing mixing angle computed by lattice QCD suggests a small contribution of meson-meson states to the bound states, dynamically generated by the coupled channel Schrödinger equation.

The only exception is the $\tilde{J} = 1$, $n = 3$ bound state with a mass close to the $\bar{B}B$ threshold, with a significantly smaller quarkonium component of $\%\bar{Q}Q \approx 58\%$. This may be caused by the rapidly changing mixing angle near the $\bar{B}B$ threshold, yielding a more significant meson-meson component compared to other states that are more strongly bound.

There are two resonances slightly above the $\bar{B}B$ threshold, $\tilde{J} = 0$, $n = 4$ and $\tilde{J} = 3$, $n = 2$. Their composition is balanced between quarkonium and $\bar{M}M$ components, while the $\bar{M}_sM_s$ component is minimal due to its higher energy threshold. For resonances with higher energy, the components for $\bar{M}M$ and $\bar{M}_sM_s$ increase, and the $\bar{Q}Q$ component ranges from 8% to 35%. These resonances tend to have larger widths and are less stable, indicating their predominantly meson-meson nature.

At approximately 11.025 GeV, the threshold for a negative and positive heavy-light meson opens, which is not included in our approach. We observe a rise in the quarkonium component in this region, which is likely a consequence of this limitation in our approach and is thus unphysical.

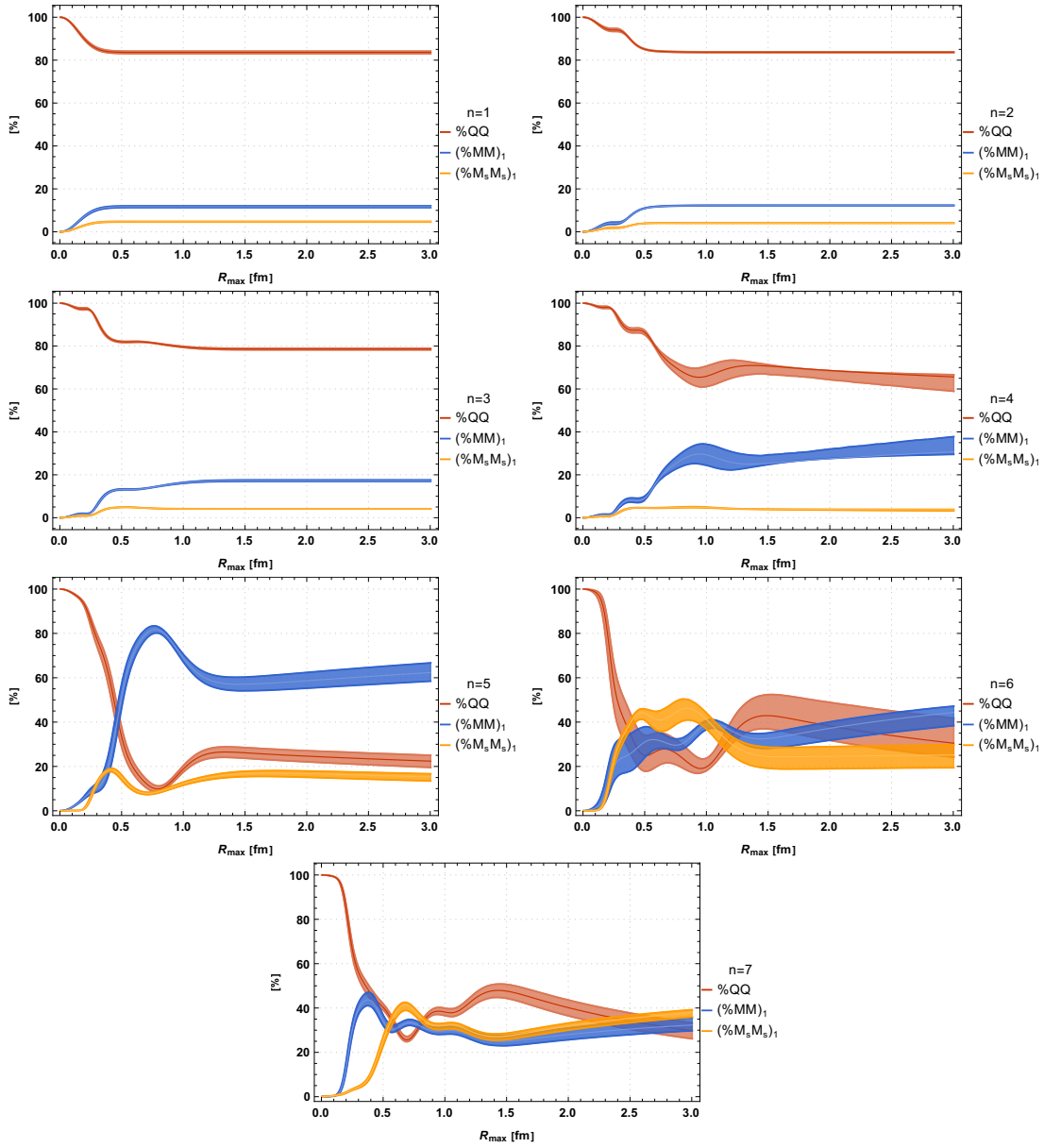

Figure 9.5: Percentages of quarkonium $\%\bar{Q}Q$ and meson-meson $(\%\bar{M}_{(s)}M_{(s)})_{L_{\rm out}}$ content for bound states and resonances with $\tilde{J} = 0$.

Table 9.1: Composition of bound states and resonances in terms of wave function components. $\%\bar{Q}Q$ and $(\%\bar{M}_{(s)}M_{(s)})_{\tilde{J}}$ are defined in Eqns. (8.63)-(8.65). The light blue backgrounds mark resonances above the threshold of one parity negative and one parity positive meson, where our results can no longer be trusted.

$\tilde{J}^{PC}$	n	m [GeV]	Γ [MeV]	$\%\bar{Q}Q$ [%]	$(\%\bar{M}M)_{\tilde{J}-1}$ [%]	$(\%\bar{M}M)_{\tilde{J}+1}$ [%]	$(\%\bar{M}_sM_s)_{\tilde{J}-1}$ [%]	$(\%\bar{M}_sM_s)_{\tilde{J}+1}$ [%]
0^{++}	1	9.618^{+10}_{-15}	–	$84(^{+\ 1}_{-\ 1})(^{+0}_{-0})$	–	$12(^{+0}_{-0})(^{+0}_{-0})$	–	$4(^{+0}_{-0})(^{+0}_{-0})$
	2	10.114^{+7}_{-11}	–	$84(^{+\ 0}_{-\ 0})(^{+0}_{-0})$	–	$12(^{+0}_{-0})(^{+0}_{-0})$	–	$4(^{+0}_{-0})(^{+0}_{-0})$
	3	10.442^{+7}_{-9}	–	$79(^{+\ 0}_{-\ 0})(^{+0}_{-0})$	–	$17(^{+0}_{-0})(^{+0}_{-0})$	–	$4(^{+0}_{-0})(^{+0}_{-0})$
	4	10.629^{+1}_{-1}	$49.3^{+\ 5.4}_{-\ 3.9}$	$67(^{+\ 5}_{-\ 0})(^{+1}_{-1})$	–	$29(^{+5}_{-0})(^{+1}_{-1})$	–	$4(^{+0}_{-0})(^{+0}_{-0})$
	5	10.773^{+1}_{-2}	$15.9^{+\ 2.9}_{-\ 4.4}$	$24(^{+\ 3}_{-\ 3})(^{+1}_{-1})$	–	$60(^{+4}_{-4})(^{+1}_{-2})$	–	$16(^{+1}_{-2})(^{+1}_{-1})$
	6	10.938^{+2}_{-2}	$61.8^{+\ 7.6}_{-\ 8.0}$	$35(^{+11}_{-\ 7})(^{+4}_{-3})$	–	$40(^{+3}_{-6})(^{+3}_{-3})$	–	$25(^{+5}_{-6})(^{+0}_{-0})$
	7	11.041^{+5}_{-7}	$45.5^{+13.5}_{-\ 8.2}$	$35(^{+\ 4}_{-\ 4})(^{+5}_{-4})$	–	$30(^{+3}_{-2})(^{+2}_{-2})$	–	$35(^{+1}_{-2})(^{+2}_{-3})$
1^{--}	1	9.930^{+4}_{-5}	–	$76(^{+\ 0}_{-\ 0})(^{+0}_{-0})$	$10(^{+0}_{-0})(^{+0}_{-0})$	$8(^{+0}_{-0})(^{+0}_{-0})$	$3(^{+0}_{-0})(^{+0}_{-0})$	$3(^{+0}_{-0})(^{+0}_{-0})$
	2	10.315^{+3}_{-4}	–	$78(^{+\ 0}_{-\ 0})(^{+0}_{-0})$	$9(^{+0}_{-0})(^{+0}_{-0})$	$8(^{+0}_{-0})(^{+0}_{-0})$	$3(^{+0}_{-0})(^{+0}_{-0})$	$2(^{+0}_{-0})(^{+0}_{-0})$
	3	10.594^{+3}_{-3}	–	$58(^{+\ 1}_{-\ 1})(^{+0}_{-0})$	$23(^{+1}_{-1})(^{+0}_{-0})$	$15(^{+0}_{-0})(^{+0}_{-0})$	$2(^{+0}_{-0})(^{+0}_{-0})$	$2(^{+0}_{-0})(^{+0}_{-0})$
	4	10.865^{+4}_{-2}	$67.5^{+\ 4.9}_{-\ 5.1}$	$8(^{+\ 1}_{-\ 1})(^{+2}_{-1})$	$5(^{+3}_{-1})(^{+0}_{-0})$	$29(^{+2}_{-4})(^{+1}_{-1})$	$44(^{+2}_{-4})(^{+1}_{-1})$	$14(^{+3}_{-2})(^{+0}_{-1})$
	5	10.932^{+3}_{-5}	$102.0^{+\ 5.0}_{-\ 7.3}$	$18(^{+\ 2}_{-\ 1})(^{+3}_{-2})$	$20(^{+1}_{-1})(^{+0}_{-0})$	$21(^{+1}_{-1})(^{+1}_{-1})$	$36(^{+2}_{-3})(^{+1}_{-2})$	$5(^{+1}_{-1})(^{+0}_{-0})$
	6	11.144^{+5}_{-8}	$24.6^{+\ 1.3}_{-\ 1.0}$	$40(^{+\ 3}_{-\ 2})(^{+4}_{-3})$	$23(^{+1}_{-2})(^{+2}_{-3})$	$8(^{+0}_{-0})(^{+0}_{-0})$	$20(^{+1}_{-1})(^{+1}_{-1})$	$9(^{+0}_{-0})(^{+0}_{-0})$
2^{++}	1	10.181^{+4}_{-5}	–	$76(^{+\ 0}_{-\ 0})(^{+0}_{-0})$	$12(^{+0}_{-0})(^{+0}_{-0})$	$6(^{+0}_{-0})(^{+0}_{-0})$	$4(^{+0}_{-0})(^{+0}_{-0})$	$2(^{+0}_{-0})(^{+0}_{-0})$
	2	10.486^{+3}_{-4}	–	$74(^{+\ 0}_{-\ 0})(^{+0}_{-0})$	$13(^{+0}_{-0})(^{+0}_{-0})$	$8(^{+0}_{-0})(^{+0}_{-0})$	$3(^{+0}_{-0})(^{+0}_{-0})$	$2(^{+0}_{-0})(^{+0}_{-0})$
	3	10.798^{+0}_{-0}	$12.3^{-\ 3.0}_{-\ 4.0}$	$21(^{+\ 1}_{-\ 1})(^{+4}_{-3})$	$51(^{+1}_{-1})(^{+3}_{-3})$	$22(^{+0}_{-0})(^{+1}_{-1})$	$4(^{+0}_{-0})(^{+1}_{-1})$	$2(^{+0}_{-0})(^{+0}_{-0})$
	4	11.038^{+3}_{-4}	$40.8^{+\ 2.8}_{-\ 2.0}$	$9(^{+\ 1}_{-\ 1})(^{+2}_{-1})$	$49(^{+0}_{-1})(^{+2}_{-3})$	$9(^{+0}_{-0})(^{+1}_{-1})$	$31(^{+0}_{-1})(^{+0}_{-0})$	$2(^{+0}_{-0})(^{+0}_{-0})$
3^{--}	1	10.390^{+3}_{-4}	–	$77(^{+\ 0}_{-\ 0})(^{+0}_{-0})$	$12(^{+0}_{-0})(^{+0}_{-0})$	$5(^{+0}_{-0})(^{+0}_{-0})$	$3(^{+0}_{-0})(^{+0}_{-0})$	$2(^{+0}_{-0})(^{+0}_{-0})$
	2	10.639^{+3}_{-2}	$2.4^{+\ 0.9}_{-\ 1.5}$	$43(^{+\ 3}_{-\ 3})(^{+3}_{-3})$	$47(^{+3}_{-3})(^{+3}_{-4})$	$7(^{+0}_{-0})(^{+0}_{-0})$	$2(^{+0}_{-0})(^{+0}_{-0})$	$1(^{+0}_{-0})(^{+0}_{-0})$
	3	10.944^{+2}_{-3}	$46.9^{+\ 6.2}_{-\ 4.6}$	$8(^{+\ 1}_{-\ 0})(^{+2}_{-1})$	$23(^{+1}_{-1})(^{+1}_{-1})$	$25(^{+0}_{-0})(^{+0}_{-0})$	$35(^{+0}_{-0})(^{+0}_{-1})$	$8(^{+0}_{-0})(^{+0}_{-0})$
	4	11.174^{+5}_{-7}	$1.9^{+\ 2.1}_{-\ 1.4}$	$43(^{+\ 3}_{-\ 2})(^{+5}_{-4})$	$27(^{+2}_{-2})(^{+1}_{-1})$	$6(^{+0}_{-0})(^{+0}_{-0})$	$13(^{+1}_{-1})(^{+2}_{-2})$	$11(^{+1}_{-1})(^{+2}_{-2})$

9.5 Comparison to experimental results

We summarize our theoretical predictions for bound states and resonances alongside corresponding experimental results in Tab. 9.2.

9.5.1 Bound states

Our predicted bound states align well with experimental observations. The $\tilde{J} = 0$ states with n = 1,2,3,4 correspond to well-established quarkonium states: $\eta_b(1S) \equiv \Upsilon(1S)$, $\Upsilon(2S)$, $\Upsilon(3S)$, and $\Upsilon(4S)$. Similarly, the $\tilde{J} = 1$ states with n = 1,2,3 correspond to $h_b(1P) \equiv \chi_{b0}(1P) \equiv \chi_{b1}(1P) \equiv \chi_{b2}(1P)$, $h_b(2P) \equiv \chi_{b0}(2P) \equiv \chi_{b1}(2P) \equiv \chi_{b2}(2P)$, and $\chi_{b1}(3P)$. The $\tilde{J} = 2$ state with $n = 1$ corresponds to $\Upsilon(1D)$.

The masses of the low-lying states are mainly consistent with their experimental counterparts. Discrepancies are primarily observed for the lowest masses. The most significant difference is seen in our results corresponding to $\eta_b(1S) \equiv \Upsilon(1S)$. This low-lying mass is particularly sensitive to the reference point for the energy scale, which is set by $E_{\text{threshold}}$ and thus directly depends on the accuracy of the lattice data. Additionally, the scale setting in the lattice computations modestly affects the results in this mass region. We estimate that combining these factors leads to approximately a 10% deviation in the results. In Section 9.6, we discuss the systematic errors in detail.

Table 9.2: Our theoretical prediction for masses and decay widths found as poles of the T matrix for angular momenta $\tilde{J} = 0,1,2,3$ and corresponding experimental results. The only exception is the $\tilde{J} = 2, n = 3$ resonance where results instead stem from a fit of Eqn. (9.2) to the eigenphase sum δ_2. Dashed lines indicate the $\bar{B}B$ and $\bar{B}_s B_s$ thresholds at 10.628 MeV and 10.808 MeV. The light blue background marks resonances above the threshold of one parity negative and one parity positive meson, where our results can no longer be trusted.

		theory		**experiment**			
$\tilde{J}^{PC}$	n	m[GeV]	Γ[MeV]	name	m[GeV]	Γ[MeV]	$I^G(J^{PC})$
0^{++}	1	9.618^{+10}_{-15}	-	$\eta_b(1S)$	9.399(2)	10(5)	$0^+(0^{+-})$
				$\Upsilon_b(1S)$	9.460(0)	≈ 0	$0^-(1^{--})$
	2	10.114^{+7}_{-11}	-	$\eta_b(2S)_{\text{BELLE}}$	9.999(6)	-	$0^+(0^{+-})$
				$\Upsilon(2S)$	10.023(0)	≈ 0	$0^-(1^{--})$
	3	10.442^{+7}_{-9}	-	$\Upsilon(3S)$	10.355(1)	≈ 0	$0^-(1^{--})$
	4	10.629^{+1}_{-1}	$49.3^{+5.4}_{-3.9}$	$\Upsilon(4S)$	10.579(1)	21(3)	$0^-(1^{--})$
	5	10.773^{+1}_{-2}	$15.9^{+2.9}_{-4.4}$	$\Upsilon(10750)_{\text{BELLE II}}$	10.753(7)	36(22)	$0^-(1^{--})$
	6	10.938^{+2}_{-2}	$61.8^{+7.6}_{-8.0}$	$\Upsilon(10860)$	10.890(3)	51(7)	$0^-(1^{--})$
	7	11.041^{+5}_{-7}	$45.5^{+13.5}_{-8.2}$	$\Upsilon(11020)$	10.993(1)	49(15)	$0^-(1^{--})$
1^{--}	1	9.930^{+43}_{-52}	-	$\chi_{b0}(1P)$	9.859(1)	-	$0^+(0^{++})$
				$h_b(1P)$	9.890(1)	-	$?^?(1^{+-})$
				$\chi_{b1}(1P)$	9.893(1)	-	$0^+(1^{++})$
				$\chi_{b2}(1P)$	9.912(1)	-	$0^+(2^{++})$
	2	10.315^{+29}_{-40}	-	$\chi_{b0}(2P)$	10.233(1)	-	$0^+(0^{++})$
				$\chi_{b1}(2P)$	10.255(1)	-	$0^+(1^{++})$
				$h_b(2P)_{\text{BELLE}}$	10.260(2)	-	$?^?(1^{+-})$
				$\chi_{b2}(2P)$	10.267(1)	-	$0^+(2^{++})$
	3	10.594^{+32}_{-28}	-	$\chi_{b1}(3P)$	10.512(2)	-	$0^+(0^{++})$
	4	10.865^{+37}_{-21}	$67.5^{+5.1}_{-4.9}$				
	5	10.932^{+33}_{-54}	$101.8^{+7.3}_{-5.1}$				
	6	11.144^{+52}_{-75}	$25.0^{+1.1}_{-1.3}$				
2^{++}	1	10.181^{+35}_{-46}	-	$\Upsilon(1D)$	10.164(2)	-	$0^-(2^{--})$
	2	10.486^{+32}_{-36}	-				
	3	$10.799^{+\ 2}_{-\ 2}$	$13.0^{+2.1}_{-2.0}$				
	4	11.038^{+30}_{-44}	$40.8^{+2.0}_{-2.8}$				
3^{--}	1	10.390^{+28}_{-39}	-				
	2	10.639^{+31}_{-25}	$2.4^{+1.5}_{-0.9}$				
	3	10.944^{+20}_{-29}	$46.8^{-4.6}_{+6.2}$				
	4	11.174^{+51}_{-69}	$1.9^{+2.1}_{-1.4}$				

9.5.2 Resonances

Three states are candidates for tetraquark resonances identified by experiments $\Upsilon(10750)$, $\Upsilon(10860)$ and $\Upsilon(11020)$. In particular, we wanted to clarify if these are S wave or D wave states, i.e., corresponding to $\tilde{J} = 0$ or $\tilde{J} = 2$, and whether they are possibly exotic states.

There are two candidates for $\Upsilon(10750)$ one S wave ($n = 5$) and one D wave ($n = 3$). Both are very close to the experimental result for this resonance; thus, it is impossible to draw a definitive conclusion about the angular momentum quantum number. However, this resonance also shows a substantial meson-meson component with 76% for the corresponding S wave resonance and 79% for the corresponding D wave resonance. This suggests that $\Upsilon(10750)$ is a crypto-exotic state of the Υ type.

$\Upsilon(10860)$ is commonly interpreted as $\Upsilon(5S)$. Our results support this interpretation as our $\tilde{J} = 0, n = 6$ resonance is close by, and there is no candidate in the D wave spectrum.

$\Upsilon(11020)$ often gets labeled as $\Upsilon(6S)$. We do not only find a candidate for this state in our S wave spectrum ($n = 7$) but also the D wave spectrum ($n = 4$). However, both results lie barely above the opening of the threshold of a positive parity and negative parity meson. We do not consider this channel, and thus, our results can not be trusted. Unfortunately, we cannot make a definitive conclusion about the nature of the $\Upsilon(11020)$ resonance.

9.6 Systematic errors and comparison to other theoretical predictions

Table 9.3: Masses of $\tilde{J} = 0$ (i.e. S wave) bound states. From left to right: our predictions as listed in Tab. 9.2; our predictions, when ignoring the unphysically heavy lattice quark masses from Ref. [72]; our predictions, when not correcting the lattice data from Ref. [72] as discussed in Ref. [104]; experimental results.

$E_{\text{threshold}}$	10.789 GeV	$2m_M$	10.789 GeV		
	Corr.	Corr.	Uncorr.	Experiment	
	m[GeV]	m[GeV]	m[GeV]	name	m[GeV]
$n = 1$	9.618^{+10}_{-15}	9.480^{+11}_{-15}	$9.679^{+\ 8}_{-12}$	$\eta_b(1S)$	9.399(2)
				$\Upsilon_b(1S)$	9.460(0)
$n = 2$	$10.114^{+\ 7}_{-11}$	$9.975^{+\ 8}_{-10}$	$10.168^{+\ 6}_{-\ 9}$	$\eta_b(2S)_{\text{BELLE}}$	9.999(6)
				$\Upsilon(2S)$	10.023(0)
$n = 3$	$10.442^{+\ 7}_{-\ 9}$	$10.308^{+\ 7}_{-\ 9}$	$10.497^{+\ 5}_{-\ 7}$	$\Upsilon(3S)$	10.355(1)

The lattice data from [72] is relatively old, considering the rapid advancements in computational power and lattice QCD techniques. Several intricacies must be considered when working with these results.

Firstly, the light quark mass used in this lattice computation is not the physical u/d mass but lies between the u/d quark mass and the s quark mass. This is accounted for by adding $E_{\text{threshold}} = 10.789$ GeV to the quarkonium channel of our equation, corresponding to the light quark mass of the lattice study. The choice of $E_{\text{threshold}}$ significantly influences the results. In Tab. 9.3, we present our predictions for the bound states of $\tilde{J} = 0$ (column one) compared to results obtained when setting $E_{\text{threshold}}$ to the physical quark mass, i.e., $E_{\text{threshold}} = 2m_M = 10.627$ GeV. While the results appear closer to experimental values, we do not consider $E_{\text{threshold}} = 2m_M$ a reasonable choice given the significantly larger quark mass used in the lattice study. We believe this discrepancy would diminish with new and more appropriate lattice results and thus choose $E_{\text{threshold}}$ in an objectively meaningful way rather than fitting our predictions to experimental data.

Another issue with the lattice data is the improper choice of creation operators in [72], which probe not only the Σ_g^+ sector but also Σ_u^-, Π_g^+, and Π_g^-. The data has to be resampled and modified to correct this, as discussed in detail in [104]. In Tab. 9.3, we show our predictions for the bound states of $\tilde{J} = 0$ (column one) compared to results obtained without correcting the potentials from the lattice data of [72]. These numbers suggest that this correction positively affects our predictions, shifting them approximately 50 MeV closer to the experimental results.

The amount of mixing between the quarkonium and meson-meson channels, determined

by the mixing angle θ, also plays a role. We explored the dependence of our results on this mixing by varying the mixing angle by 10%, which had a relatively minor effect on the resulting spectrum, around $10 - 15$ MeV.

Another issue, particularly for the low-lying bound states, is the scale setting, where we set the scale by identifying $r_0 = 0.5$ fm. Recent lattice studies suggest this value is slightly lower, around $r_0 \approx 0.475$ fm. We investigated the effects of choosing this smaller r_0 on our results and found an approximately -50 MeV improvement on the lowest-lying bound state $\tilde{J} = 0, n = 1$.

In recent years, multiple groups have studied the bottomonium $I = 0$ spectrum similarly [105, 107–110, 118]. One such publication [118] used the same lattice data from [72] and obtained a spectrum closer to the experimental results. However, they did not account for the different light quark mass of the lattice data. As explained above, this significantly influences the results. They attribute the discrepancies to the corrections of the potentials, which create a pronounced bump at small distances. While we do not have a definitive explanation for this bump, as shown in Tab. 9.3, correcting the potentials shifts our results towards the experimental reference values rather than away. We can reproduce similar results as shown in [118] by setting $E_{\text{threshold}} = 2m_B = 10.628$ GeV, also demonstrated in Tab. 9.3. As discussed above, this is not a reasonable choice because the pion mass used in the lattice computation [72] was much larger than the physical pion mass.

CHAPTER 10

Conclusion

We have extended the formalism from [104] to investigate the quarkonium spectrum for arbitrary angular momentum $\tilde{J}$ and to include $\bar{M}_s M_s$ channels using the same lattice QCD potentials from [72] as for the $\bar{M}M$ channels. We successfully computed the bottomonium spectrum within this framework for angular momenta $\tilde{J} \leq 3$ with one quarkonium $\bar{Q}Q$ and four meson-meson channels, two corresponding to $\bar{M}M$ and two corresponding to $\bar{M}_s M_s$. The results are summarized in Fig. 10.1.

Our findings provide counterparts for all bound states observed experimentally, albeit with moderate to large systematic errors. Furthermore, we find strong indications that $\Upsilon(10750)$ is a crypto-exotic state and that $\Upsilon(10860)$ can be identified as $\Upsilon(5S)$. Additionally, we identify possible candidates for $\Upsilon(11020)$ in the S and D wave spectrum.

We believe that the framework discussed herein is constructed carefully and meaningfully. The long-term objective is to reduce systematic and statistical errors to a level where

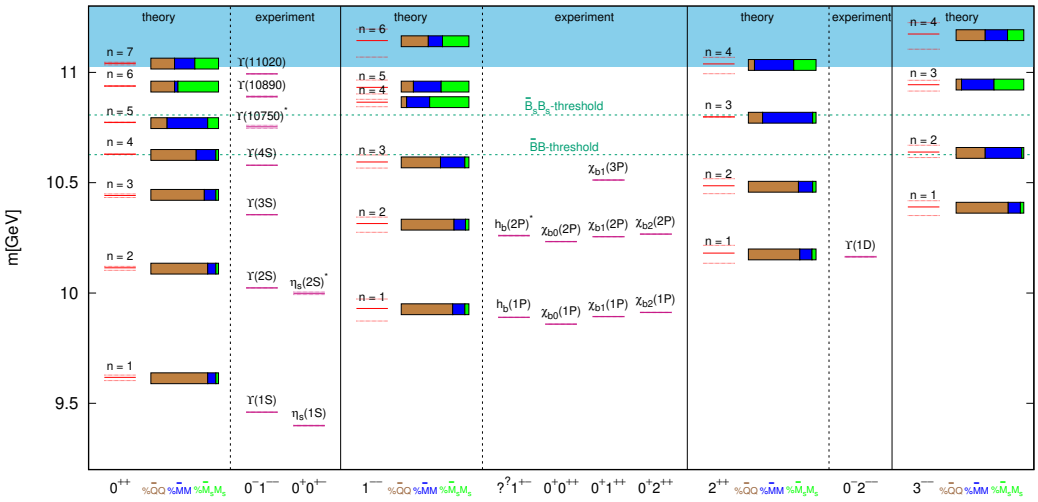

Figure 10.1: Graphical summary of our theoretical predictions for bottomonium bound states and resonances compared to experimental results. The light-blue color indicates the energy region where our results can no longer be trusted due to the threshold's opening with one parity positive and one parity negative meson.

precise predictions can be made. One essential step is recomputing the lattice potentials with more suitable operators and state-of-the-art lattice techniques. In the first part of this thesis, we computed static potentials for a different tetraquark system using identical techniques. Thus, the foundation for the computation of $\bar{B}B$ static potentials is established and represents a potential project for the near future.

These new lattice results could enable us to set the scale more precisely by using a more up-to-date Sommer parameter r_0 to determine the lattice spacing a. Additionally, we might be able to tune the bottom quark mass m_b without relying on results from quark models.

The large discrepancy between our predictions for the lowest energy bound states and experimental results might stem from the significant uncertainty in the mixing angle θ from the lattice study [72], as this angle strongly impacts the potential matrix. A more precise computation of this quantity could significantly improve these predictions.

However, the lattice data is not the sole source of systematic errors. One of the major contributors is the neglect of heavy quark spin effects; thus, an inclusion similar to that in the related work [44] is important for future studies. Moreover, one could compute $1/m_b$ and even $1/(m_b)^2$ corrections for the confining potential $V_{\bar{Q}Q}(r)$ on the lattice (see [48, 52, 53, 119–121]).

An obvious extension of this formalism would be to include the possibility of one parity-positive and one parity-negative meson, enabling the study of resonances up to ≈ 11.525 GeV and making our prediction for $\Upsilon(11020)$ more meaningful, as well as providing additional predictions for resonances not yet observed experimentally.

Bibliography

1. Group, Particle Data et al.: 'Review of Particle Physics'. *Progress of Theoretical and Experimental Physics* (Aug. 2022), vol. 2022(8): p. 083C01 (cit. on pp. 1, 11).
2. Jaffe, Robert L.: 'Multi-Quark Hadrons. 1. The Phenomenology of (2 Quark 2 anti-Quark) Mesons'. *Phys.Rev.* (1977), vol. D15: p. 267 (cit. on p. 2).
3. Liu, Z. Q. et al.: 'Study of $e^+e^-ß\pi^+\pi^- J/\psi$ and Observation of a Charged Charmoniumlike State at Belle'. *Phys. Rev. Lett.* (2013), vol. 110. [Erratum: Phys.Rev.Lett. 111, 019901 (2013)]: p. 252002 (cit. on p. 2).
4. Chilikin, K. et al.: 'Observation of a new charged charmoniumlike state in $\bar{B}^0 \to J/\psi K^-\pi^+$ decays'. *Phys. Rev. D* (2014), vol. 90(11): p. 112009 (cit. on p. 2).
5. Ablikim, M. et al.: 'Observation of a charged charmoniumlike structure in $e^+e^- \to (D^*\bar{D}^*)^\pm\pi^\mp$ at $\sqrt{s} = 4.26$GeV'. *Phys. Rev. Lett.* (2014), vol. 112(13): p. 132001 (cit. on p. 2).
6. Bondar, A. et al.: 'Observation of two charged bottomonium-like resonances in Y(5S) decays'. *Phys. Rev. Lett.* (2012), vol. 108: p. 122001 (cit. on pp. 2, 47).
7. Ablikim, M. et al.: 'Observation of a Charged Charmoniumlike Structure $Z_c(4020)$ and Search for the $Z_c(3900)$ in $e^+e^- \to \pi^+\pi^- h_c$'. *Phys. Rev. Lett.* (2013), vol. 111(24): p. 242001 (cit. on p. 2).
8. Ablikim, M. et al.: 'Observation of a charged $(D\bar{D}^*)^\pm$ mass peak in $e^+e^- \to \pi D\bar{D}^*$ at $\sqrt{s} = 4.26$ GeV'. *Phys. Rev. Lett.* (2014), vol. 112(2): p. 022001 (cit. on p. 2).
9. Ablikim, M. et al.: 'Observation of $e^+e^-ß\pi^0\pi^0 h_c$ and a Neutral Charmoniumlike Structure $Z_c(4020)^0$'. *Phys. Rev. Lett.* (2014), vol. 113(21): p. 212002 (cit. on p. 2).
10. Aaij, Roel et al.: 'Observation of the resonant character of the $Z(4430)^-$ state'. *Phys. Rev. Lett.* (2014), vol. 112(22): p. 222002 (cit. on p. 2).
11. Aaij, Roel et al.: 'Model-independent confirmation of the $Z(4430)^-$ state'. *Phys. Rev. D* (2015), vol. 92(11): p. 112009 (cit. on p. 2).
12. Aaij, Roel et al.: 'Evidence for an $\eta_c(1S)\pi^-$ resonance in $B^0 \to \eta_c(1S)K^+\pi^-$ decays'. *Eur. Phys. J. C* (2018), vol. 78(12): p. 1019 (cit. on p. 2).
13. Aaij, Roel et al.: 'A model-independent study of resonant structure in $B^+ \to D^+D^-K^+$ decays'. *Phys. Rev. Lett.* (2020), vol. 125: p. 242001 (cit. on p. 2).
14. Aaij, Roel et al.: 'Amplitude analysis of the $B^+ \to D^+D^-K^+$ decay'. *Phys. Rev. D* (2020), vol. 102: p. 112003 (cit. on p. 2).

15. Aaij, Roel et al.: 'Observation of New Resonances Decaying to $J/\psi K^+$+ and $J/\psi\phi$'. *Phys. Rev. Lett.* (2021), vol. 127(8): p. 082001 (cit. on p. 2).
16. Ablikim, M. et al.: 'Observation of a Charged Charmoniumlike Structure in e^+e^- $\rightarrow \pi^+\pi^-$ J/ψ at $\sqrt{s}$ =4.26 GeV'. *Phys. Rev. Lett.* (2013), vol. 110: p. 252001 (cit. on p. 2).
17. Ablikim, M. et al.: 'Confirmation of a charged charmoniumlike state $Z_c(3885)^{\mp}$ in $e^+e^- \rightarrow \pi^{\pm}(D\bar{D}^*)^{\mp}$ with double D tag'. *Phys. Rev. D* (2015), vol. 92(9): p. 092006 (cit. on p. 2).
18. Ablikim, Medina et al.: 'Observation of a Near-Threshold Structure in the K^+ Recoil-Mass Spectra in $e^+e^- \rightarrow K^+(D_s^-D^{*0} + D_s^{*-}D^0)$'. *Phys. Rev. Lett.* (2021), vol. 126(10): p. 102001 (cit. on p. 2).
19. Rodas, A. et al.: 'Determination of the pole position of the lightest hybrid meson candidate'. *Phys. Rev. Lett.* (2019), vol. 122(4): p. 042002 (cit. on p. 2).
20. Mizuk, R. et al.: 'Dalitz analysis of B —> K pi+ psi-prime decays and the Z(4430)+'. *Phys. Rev. D* (2009), vol. 80: p. 031104 (cit. on p. 2).
21. Chilikin, K. et al.: 'Experimental constraints on the spin and parity of the $Z(4430)^+$'. *Phys. Rev. D* (2013), vol. 88(7): p. 074026 (cit. on p. 2).
22. Mizuk, R. et al.: 'Observation of a new structure near 10.75 GeV in the energy dependence of the e$^+$e$\rightarrow$ $\Upsilon(nS)\pi^+\pi$ (n = 1, 2, 3) cross sections'. *JHEP* (2019), vol. 10: p. 220 (cit. on pp. 2, 47).
23. Xiao, T., S. Dobbs, A. Tomaradze, and Kamal K. Seth: 'Observation of the Charged Hadron $Z_c^{\pm}(3900)$ and Evidence for the Neutral $Z_c^0(3900)$ in $e^+e^- \rightarrow \pi\pi J/\psi$ at $\sqrt{s} = 4170$ MeV'. *Phys. Lett. B* (2013), vol. 727: pp. 366–370 (cit. on p. 2).
24. Ketzer, Bernhard: 'Hybrid Mesons'. *PoS* (2012), vol. QNP2012. Ed. by Pire, Bernard: p. 025 (cit. on p. 2).
25. Aaij, Roel et al.: 'Study of the doubly charmed tetraquark T_{cc}^+'. (Sept. 2021), vol. (cit. on p. 2).
26. Aaij, Roel et al.: 'Observation of an exotic narrow doubly charmed tetraquark'. (Sept. 2021), vol. (cit. on p. 2).
27. Wilson, Kenneth G.: 'Confinement of Quarks'. *Phys. Rev. D* (1974), vol. 10. Ed. by Taylor, J. C.: pp. 2445–2459 (cit. on pp. 2, 8).
28. Born, M. and R. Oppenheimer: 'Zur Quantentheorie der Molekeln'. *Annalen der Physik* (1927), vol. 389(20): pp. 457–484 (cit. on p. 2).
29. Bicudo, Pedro and Marc Wagner: 'Lattice QCD signal for a bottom-bottom tetraquark'. *Phys. Rev. D* (2013), vol. 87(11): p. 114511 (cit. on pp. 5, 40, 41).
30. Bicudo, Pedro, Krzysztof Cichy, Antje Peters, and Marc Wagner: 'BB interactions with static bottom quarks from Lattice QCD'. *Phys. Rev. D* (2016), vol. 93(3): p. 034501 (cit. on pp. 5, 21, 31, 40, 41, 43).

31. Bicudo, Pedro, Jonas Scheunert, and Marc Wagner: 'Including heavy spin effects in the prediction of a $\bar{b}\bar{b}ud$ tetraquark with lattice QCD potentials'. *Phys. Rev. D* (2017), vol. 95(3): p. 034502 (cit. on pp. 5, 32, 35).

32. Francis, Anthony, Renwick J. Hudspith, Randy Lewis, and Kim Maltman: 'Lattice Prediction for Deeply Bound Doubly Heavy Tetraquarks'. *Phys. Rev. Lett.* (2017), vol. 118(14): p. 142001 (cit. on p. 5).

33. Francis, Anthony, Renwick J. Hudspith, Randy Lewis, and Kim Maltman: 'Evidence for charm-bottom tetraquarks and the mass dependence of heavy-light tetraquark states from lattice QCD'. *Phys. Rev. D* (2019), vol. 99(5): p. 054505 (cit. on p. 5).

34. Junnarkar, Parikshit, Nilmani Mathur, and M. Padmanath: 'Study of doubly heavy tetraquarks in Lattice QCD'. *Phys. Rev. D* (2019), vol. 99(3): p. 034507 (cit. on p. 5).

35. Hudspith, R. J., B. Colquhoun, A. Francis, R. Lewis, and K. Maltman: 'A lattice investigation of exotic tetraquark channels'. *Phys. Rev. D* (2020), vol. 102: p. 114506 (cit. on p. 5).

36. Leskovec, Luka, Stefan Meinel, Martin Pflaumer, and Marc Wagner: 'Lattice QCD investigation of a doubly-bottom $\bar{b}\bar{b}ud$ tetraquark with quantum numbers $I(J^P) = 0(1^+)$'. *Phys. Rev. D* (2019), vol. 100(1): p. 014503 (cit. on pp. 5, 11).

37. Mohanta, Protick and Subhasish Basak: 'Construction of $bb\bar{u}\bar{d}$ tetraquark states on lattice with NRQCD bottom and HISQ up and down quarks'. *Phys. Rev. D* (2020), vol. 102(9): p. 094516 (cit. on p. 5).

38. Meinel, Stefan, Martin Pflaumer, and Marc Wagner: 'Search for $\mathrm{b}^{-}\mathrm{b}^{-}\mathrm{us}$ and $\mathrm{b}^{-}\mathrm{c}^{-}\mathrm{ud}$ tetraquark bound states using lattice QCD'. *Phys. Rev. D* (2022), vol. 106(3): p. 034507 (cit. on pp. 5, 11).

39. Padmanath, M., Archana Radhakrishnan, and Nilmani Mathur: 'Bound isoscalar axial-vector $bc\bar{u}\bar{d}$ tetraquark T_{bc} in QCD'. (July 2023), vol. (cit. on p. 5).

40. Luscher, Martin: 'Two particle states on a torus and their relation to the scattering matrix'. *Nucl. Phys. B* (1991), vol. 354: pp. 531–578 (cit. on p. 5).

41. Aoki, Takafumi, Sinya Aoki, and Takashi Inoue: 'Lattice study on a tetraquark state Tbb in the HAL QCD method'. *Phys. Rev. D* (2023), vol. 108(5): p. 054502 (cit. on p. 5).

42. Ishii, N., S. Aoki, and T. Hatsuda: 'The Nuclear Force from Lattice QCD'. *Phys. Rev. Lett.* (2007), vol. 99: p. 022001 (cit. on p. 5).

43. Bicudo, Pedro: 'Tetraquarks and pentaquarks in lattice QCD with light and heavy quarks'. *Phys. Rept.* (2023), vol. 1039: pp. 1–49 (cit. on p. 5).

44. Bicudo, Pedro, Marco Cardoso, Antje Peters, Martin Pflaumer, and Marc Wagner: '$ud\bar{b}\bar{b}$ tetraquark resonances with lattice QCD potentials and the Born-Oppenheimer approximation'. *Phys. Rev. D* (2017), vol. 96(5): p. 054510 (cit. on pp. 5, 78).

45. Pflaumer, Martin, Pedro Bicudo, Marco Cardoso, Antje Peters, and Marc Wagner: '$\bar{b}\bar{b}ud$ tetraquark resonances in the Born-Oppenheimer approximation using lattice QCD potentials'. *PoS* (2019), vol. Confinement2018: p. 123 (cit. on p. 5).

46. Hoffmann, Jakob, André Zimermmane-Santos, and Marc Wagner: 'Inclusion of heavy spin effects in the $ud\bar{b}\bar{b}$ $I(J^P)$=0(1$^-$) four-quark channel in the Born-Oppenheimer approximation'. *PoS* (2023), vol. LATTICE2022: p. 262 (cit. on pp. 5, 32).

47. Alexandrou, Constantia, Jacob Finkenrath, Theodoros Leontiou, Stefan Meinel, Martin Pflaumer, and Marc Wagner: 'Shallow Bound States and Hints for Broad Resonances with Quark Content b$^-$c$^-$ud in B-D$^-$ and B*-D$^-$ Scattering from Lattice QCD'. *Phys. Rev. Lett.* (2024), vol. 132(15): p. 151902 (cit. on pp. 6, 11).

48. Pineda, Antonio and Antonio Vairo: 'The QCD potential at O (1 / $m^{2)}$: Complete spin dependent and spin independent result'. *Phys. Rev. D* (2001), vol. 63. [Erratum: Phys.Rev.D 64, 039902E (2001)]: p. 054007 (cit. on pp. 6, 78).

49. Peset, Clara, Antonio Pineda, and Maximilian Stahlhofen: 'Potential NRQCD for unequal masses and the B_c spectrum at N^{3}LO'. *JHEP* (2016), vol. 05: p. 017 (cit. on p. 6).

50. Peset, Clara, Antonio Pineda, and Jorge Segovia: 'P-wave heavy quarkonium spectrum with next-to-next-to-next-to-leading logarithmic accuracy'. *Phys. Rev. D* (2018), vol. 98(9): p. 094003 (cit. on p. 6).

51. Anzai, C., D. Moreno, and A. Pineda: 'S-wave heavy quarkonium spectrum with next-to-next-to-next-to-leading logarithmic accuracy'. *Phys. Rev. D* (2018), vol. 98(11): p. 114034 (cit. on p. 6).

52. Bali, Gunnar S., Klaus Schilling, and Armin Wachter: 'Complete O (v**2) corrections to the static interquark potential from SU(3) gauge theory'. *Phys. Rev. D* (1997), vol. 56: pp. 2566–2589 (cit. on pp. 6, 78).

53. Koma, Yoshiaki and Miho Koma: 'Spin-dependent potentials from lattice QCD'. *Nucl. Phys. B* (2007), vol. 769: pp. 79–107 (cit. on pp. 6, 78).

54. Eichberg, Michael and Marc Wagner: 'Relativistic corrections to the static potential from generalized Wilson loops at finite flow time'. *PoS* (2024), vol. LATTICE2023: p. 068 (cit. on p. 6).

55. Gattringer, Christof and Christian B. Lang: *Quantum chromodynamics on the lattice*. Vol. 788. Berlin: Springer, 2010 (cit. on pp. 7, 9).

56. Rothe, Heinz J.: *Lattice Gauge Theories : An Introduction (Fourth Edition)*. Vol. 43. World Scientific Publishing Company, 2012 (cit. on p. 7).

57. Luscher, M. and P. Weisz: 'Computation of the Action for On-Shell Improved Lattice Gauge Theories at Weak Coupling'. *Phys. Lett. B* (1985), vol. 158: pp. 250–254 (cit. on pp. 8, 9).

58. Iwasaki, Y. and T. Yoshie: 'Renormalization Group Improved Action for SU(3) Lattice Gauge Theory and the String Tension'. *Phys. Lett. B* (1984), vol. 143: pp. 449–452 (cit. on p. 8).

59. Kaplan, David B.: 'A Method for simulating chiral fermions on the lattice'. *Phys. Lett. B* (1992), vol. 288: pp. 342–347 (cit. on p. 9).

60. Shamir, Yigal: 'Chiral fermions from lattice boundaries'. *Nucl. Phys. B* (1993), vol. 406: pp. 90–106 (cit. on p. 9).

61. Kogut, John B. and Leonard Susskind: 'Hamiltonian Formulation of Wilson's Lattice Gauge Theories'. *Phys. Rev. D* (1975), vol. 11: pp. 395–408 (cit. on p. 9).

62. Symanzik, K.: 'Continuum Limit and Improved Action in Lattice Theories. 1. Principles and φ^4 Theory'. *Nucl. Phys. B* (1983), vol. 226: pp. 187–204 (cit. on p. 9).

63. Symanzik, K.: 'Continuum Limit and Improved Action in Lattice Theories. 2. O(N) Nonlinear Sigma Model in Perturbation Theory'. *Nucl. Phys. B* (1983), vol. 226: pp. 205–227 (cit. on p. 9).

64. Thacker, B. A. and G. Peter Lepage: 'Heavy quark bound states in lattice QCD'. *Phys. Rev. D* (1991), vol. 43: pp. 196–208 (cit. on p. 11).

65. Hashimoto, Shoji and Tetsuya Onogi: 'Heavy quarks on the lattice'. *Ann. Rev. Nucl. Part. Sci.* (2004), vol. 54: pp. 451–486 (cit. on p. 11).

66. Meinel, Stefan: 'Heavy quark physics on the lattice with improved nonrelativistic actions'. PhD thesis. Cambridge U., DAMTP, Mar. 2010 (cit. on p. 11).

67. Blossier, Benoit, Michele Della Morte, Georg von Hippel, Tereza Mendes, and Rainer Sommer: 'On the generalized eigenvalue method for energies and matrix elements in lattice field theory'. *JHEP* (2009), vol. 04: p. 094 (cit. on pp. 12, 21, 35).

68. Abazov, V. M. et al.: 'Observation and Properties of $L = 1B_1$ and B_2^* Mesons'. *Phys. Rev. Lett.* (2007), vol. 99: p. 172001 (cit. on p. 13).

69. Aaltonen, T. et al.: 'Observation of orbitally excited B_s mesons'. *Phys. Rev. Lett.* (2008), vol. 100: p. 082001 (cit. on p. 13).

70. Jansen, Karl, Chris Michael, Andrea Shindler, and Marc Wagner: 'The Static-light meson spectrum from twisted mass lattice QCD'. *JHEP* (2008), vol. 12: p. 058 (cit. on pp. 14, 30).

71. Michael, Chris, Andrea Shindler, and Marc Wagner: 'The continuum limit of the static-light meson spectrum'. *JHEP* (2010), vol. 08: p. 009 (cit. on pp. 14, 30).

72. Bali, Gunnar S., Hartmut Neff, Thomas Dussel, Thomas Lippert, and Klaus Schilling: 'Observation of string breaking in QCD'. *Phys. Rev. D* (2005), vol. 71: p. 114513 (cit. on pp. 14, 23, 27, 47, 52–54, 65, 67, 74, 75, 77, 78).

73. Bulava, John, Ben Hörz, Francesco Knechtli, Vanessa Koch, Graham Moir, Colin Morningstar, and Mike Peardon: 'String breaking by light and strange quarks in QCD'. *Phys. Lett.* (2019), vol. B793: pp. 493–498 (cit. on pp. 14, 23, 52, 60).

74. Bulava, John, Francesco Knechtli, Vanessa Koch, Colin Morningstar, and Michael Peardon: 'The quark-mass dependence of the potential energy between static colour sources in the QCD vacuum with light and strange quarks'. (Mar. 2024), vol. (cit. on pp. 14, 23, 52).

75. Albanese, M. et al.: 'Glueball Masses and String Tension in Lattice QCD'. *Phys. Lett. B* (1987), vol. 192: pp. 163–169 (cit. on p. 25).

76. Gusken, S.: 'A Study of smearing techniques for hadron correlation functions'. *Nucl. Phys. B Proc. Suppl.* (1990), vol. 17. Ed. by Cabibbo, N., E. Marinari, G. Parisi, Roberto Petronzio, L. Maiani, G. Martinelli, and Roberto Pettorino: pp. 361–364 (cit. on p. 25).

77. Della Morte, Michele, Andrea Shindler, and Rainer Sommer: 'On lattice actions for static quarks'. *JHEP* (2005), vol. 08: p. 051 (cit. on p. 27).

78. Sommer, R.: 'A New way to set the energy scale in lattice gauge theories and its applications to the static force and α_s in SU(2) Yang-Mills theory'. *Nucl. Phys. B* (1994), vol. 411: pp. 839–854 (cit. on p. 27).

79. Hasenfratz, A., R. Hoffmann, and F. Knechtli: 'The Static potential with hypercubic blocking'. *Nucl. Phys. B Proc. Suppl.* (2002), vol. 106. Ed. by Muller-Preussker, M., Wolfgang Bietenholz, K. Jansen, F. Jegerlehner, I. Montvay, G. Schierholz, R. Sommer, and U. Wolff: pp. 418–420 (cit. on p. 28).

80. Michael, Christopher: 'The Running coupling from lattice gauge theory'. *Phys. Lett. B* (1992), vol. 283: pp. 103–106 (cit. on p. 28).

81. Schlosser, Carolin, Sonja Köhler, and Marc Wagner: 'Lattice field theory results for hybrid static potentials at short quark-antiquark separations and their parametrization'. *PoS* (2023), vol. LATTICE2022: p. 083 (cit. on p. 28).

82. Fritzsch, Patrick, Francesco Knechtli, Bjorn Leder, Marina Marinkovic, Stefan Schaefer, Rainer Sommer, and Francesco Virotta: 'The strange quark mass and Lambda parameter of two flavor QCD'. *Nucl. Phys. B* (2012), vol. 865: pp. 397–429 (cit. on p. 29).

83. Engel, Georg P., Leonardo Giusti, Stefano Lottini, and Rainer Sommer: 'Spectral density of the Dirac operator in two-flavor QCD'. *Phys. Rev. D* (2015), vol. 91(5): p. 054505 (cit. on p. 29).

84. Campos, Isabel, Patrick Fritzsch, Martin Hansen, Marina Krstic Marinkovic, Agostino Patella, Alberto Ramos, and Nazario Tantalo: 'openQ*D code: a versatile tool for QCD+QED simulations'. *Eur. Phys. J. C* (2020), vol. 80(3): p. 195 (cit. on p. 30).

85. Berwein, Matthias, Nora Brambilla, Abhishek Mohapatra, and Antonio Vairo: 'One Born−Oppenheimer Effective Theory to rule them all: hybrids, tetraquarks, pentaquarks, doubly heavy baryons and quarkonium'. (Aug. 2024), vol. (cit. on p. 32).

86. Wagner, Marc and Christian Wiese: 'The static-light baryon spectrum from twisted mass lattice QCD'. *JHEP* (2011), vol. 07: p. 016 (cit. on p. 37).

87. Francis, Anthony, Philippe de Forcrand, Randy Lewis, and Kim Maltman: 'Diquark properties from full QCD lattice simulations'. *JHEP* (2022), vol. 05: p. 062 (cit. on p. 37).

88. Bicudo, P., M. Cardoso, O. Oliveira, and P. J. Silva: 'Lattice QCD static potentials of the meson-meson and tetraquark systems computed with both quenched and full QCD'. *Phys. Rev. D* (2017), vol. 96(7): p. 074508 (cit. on p. 37).

89. Beane, S. R., Paulo F. Bedaque, M. J. Savage, and U. van Kolck: 'Towards a perturbative theory of nuclear forces'. *Nucl. Phys. A* (2002), vol. 700: pp. 377–402 (cit. on p. 37).

90. Bicudo, Pedro, Antje Peters, Sebastian Velten, and Marc Wagner: 'Importance of meson-meson and of diquark-antidiquark creation operators for a $\bar{b}\bar{b}ud$ tetraquark'. *Phys. Rev. D* (2021), vol. 103(11): p. 114506 (cit. on p. 43).

91. Wagner, Marc, Pedro Bicudo, Antje Peters, and Sebastian Velten: 'Comparing meson-meson and diquark-antidiquark creation operators for a $\bar{b}\bar{b}ud$ tetraquark'. *PoS* (2022), vol. LATTICE2021: p. 380 (cit. on p. 43).

92. Lüscher, Martin: 'Properties and uses of the Wilson flow in lattice QCD'. *JHEP* (2010), vol. 08. [Erratum: JHEP 03, 092 (2014)]: p. 071 (cit. on p. 43).

93. Bicudo, Pedro, Krzysztof Cichy, Antje Peters, Björn Wagenbach, and Marc Wagner: 'Evidence for the existence of $ud\bar{b}\bar{b}$ and the non-existence of $ss\bar{b}\bar{b}$ and $cc\bar{b}\bar{b}$ tetraquarks from lattice QCD'. *Phys. Rev. D* (2015), vol. 92(1): p. 014507 (cit. on p. 43).

94. Hackett, Daniel C. and Michael L. Wagman: 'Lanczos for lattice QCD matrix elements'. (July 2024), vol. (cit. on p. 44).

95. Wagman, Michael L.: 'Lanczos, the transfer matrix, and the signal-to-noise problem'. (June 2024), vol. (cit. on p. 44).

96. Reid, Roderick V: 'Local phenomenological nucleon-nucleon potentials'. *Annals of Physics* (1968), vol. 50(3): pp. 411–448 (cit. on p. 44).

97. Lacombe, M., B. Loiseau, J. M. Richard, R. Vinh Mau, J. Côté, P. Pirès, and R. de Tourreil: 'Parametrization of the Paris $N-N$ potential'. *Phys. Rev. C* (3 1980), vol. 21: pp. 861–873 (cit. on p. 44).

98. Nagels, M. M., T. A. Rijken, and J. J. de Swart: 'Baryon-baryon scattering in a one-boson-exchange-potential approach. I. Nucleon-nucleon scattering'. *Phys. Rev. D* (3 1975), vol. 12: pp. 744–758 (cit. on p. 44).

99. Machleidt, R., K. Holinde, and Ch. Elster: 'The bonn meson-exchange model for the nucleon—nucleon interaction'. *Physics Reports* (1987), vol. 149(1): pp. 1–89 (cit. on p. 44).

100. Wiringa, Robert B., V. G. J. Stoks, and R. Schiavilla: 'An Accurate nucleon-nucleon potential with charge independence breaking'. *Phys. Rev. C* (1995), vol. 51: pp. 38–51 (cit. on p. 44).

101. Prelovsek, S., H. Bahtiyar, and J. Petkovic: 'Zb tetraquark channel from lattice QCD and Born-Oppenheimer approximation'. *Phys. Lett. B* (2020), vol. 805: p. 135467 (cit. on p. 47).

102. Sadl, Mitja and Sasa Prelovsek: 'Tetraquark systems $\bar{b}b\bar{d}u$ in the static limit and lattice QCD'. *Phys. Rev. D* (2021), vol. 104(11): p. 114503 (cit. on p. 47).

103. Garmash, A. et al.: 'Amplitude analysis of $e^+e^- \to \Upsilon(nS)\pi^+\pi^-$ at $\sqrt{s} = 10.865$~GeV'. *Phys. Rev. D* (2015), vol. 91(7): p. 072003 (cit. on p. 47).

104. Bicudo, Pedro, Marco Cardoso, Nuno Cardoso, and Marc Wagner: 'Bottomonium resonances with $I = 0$ from lattice QCD correlation functions with static and light quarks'. *Phys. Rev. D* (2020), vol. 101(3): p. 034503 (cit. on pp. 47, 48, 52–54, 56, 59, 74, 77).

105. Tarrús Castellà, Jaume: 'Spin structure of heavy-quark hybrids'. *AIP Conf. Proc.* (2020), vol. 2249(1). Ed. by Meye, Curtis and Reinhard A. Schumacher: p. 020008 (cit. on pp. 48, 75).

106. Soto, Joan and Jaume Tarrús Castellà: 'Nonrelativistic effective field theory for heavy exotic hadrons'. *Phys. Rev. D* (2020), vol. 102(1): p. 014012 (cit. on p. 48).

107. Bruschini, R. and P. González: 'Diabatic description of charmoniumlike mesons'. *Phys. Rev. D* (2020), vol. 102(7): p. 074002 (cit. on pp. 48, 75).

108. Bruschini, R. and P. González: 'Coupled-channel meson-meson scattering in the diabatic framework'. *Phys. Rev. D* (2021), vol. 104: p. 074025 (cit. on pp. 48, 75).

109. Bruschini, R. and P. González: 'Diabatic description of bottomoniumlike mesons'. *Phys. Rev. D* (2021), vol. 103(11): p. 114016 (cit. on pp. 48, 75).

110. Bruschini, R.: 'Heavy-quark spin symmetry breaking in the Born-Oppenheimer approximation'. *JHEP* (2023), vol. 08: p. 219 (cit. on pp. 48, 75).

111. Schwabl, F.: *Advanced quantum mechanics (QM II)*. 1997 (cit. on p. 51).

112. Schwabl, Franz: *Quantum Mechanics (Fourth Edition)*. Springer, 2007 (cit. on p. 51).

113. Sakurai, Jun John and Jim Napolitano: *Modern Quantum Mechanics*. Quantum physics, quantum information and quantum computation. Cambridge University Press, Oct. 2020 (cit. on p. 51).

114. Newton, R. G.: *SCATTERING THEORY OF WAVES AND PARTICLES*. 1982 (cit. on p. 51).

115. Hazi, A. U.: 'Behavior of the eigenphase sum near a resonance'. *Phys. Rev. A* (2 1979), vol. 19: pp. 920–922 (cit. on p. 59).

116. Ashton, C. J., M. S. Child, and Jeremy M. Hutson: 'Rotational predissociation of the Ar·HCl van der Waals complex: Close-coupled scattering calculations'. *The Journal of Chemical Physics* (1983), vol. 78(6): pp. 4025–4039 (cit. on p. 59).

117. Hagino, K., H. Sagawa, S. Kanaya, and A. Odahara: 'Resonance width for a particle–core coupling model with a square-well potential'. *PTEP* (2020), vol. 2020(2): p. 023D01 (cit. on p. 59).

118. Tarrús Castellà, Jaume: 'Heavy meson thresholds in Born-Oppenheimer effective field theory'. *Phys. Rev. D* (2022), vol. 106(9): p. 094020 (cit. on p. 75).

119. Koma, Yoshiaki and Miho Koma: 'Heavy quarkonium spectroscopy in pNRQCD with lattice QCD input'. *PoS* (2012), vol. LATTICE2012. Ed. by Leinweber, Derek, Waseem Kamleh, Selim Mahbub, Hrayr Matevosyan, Anthony Thomas, Anthony G. Williams, Ross Young, and James Zanotti: p. 140 (cit. on p. 78).

120. Brambilla, Nora, Antonio Pineda, Joan Soto, and Antonio Vairo: 'The QCD potential at O(1/m)'. *Phys. Rev. D* (2000), vol. 63: p. 014023 (cit. on p. 78).

121. Brambilla, Nora, Antonio Vairo, and Thomas Rosch: 'Effective field theory Lagrangians for baryons with two and three heavy quarks'. *Phys. Rev. D* (2005), vol. 72: p. 034021 (cit. on p. 78).

List of Figures

4.1 On- and off-axis separations and corresponding symmetry groups. 20
4.2 Left: Illustration of APE smearing where the thick line in the center is the original link, while other lines indicate path of links that are summed over to create the smeared link. Right: Illustration of HYP smearing indicating, that multiple levels of smearing are performed, contained within a hypercube. 27

5.1 Effective masses of the S and P_- mesons $m_{\text{eff}}(t)$ with light u/d and s quarks for ensembles A5, G8, and N6. 31
5.2 All twelve $\bar{Q}\bar{Q}ud$ potentials for $I = 0$. 32
5.3 All twelve $\bar{Q}\bar{Q}ud$ potentials for $I = 1$. 33
5.4 Effective mass plots corresponding to the most attractive potential $V^{0;0,-,+}_{\bar{Q}\bar{Q}ud,\text{eff}}(r)$ for on-axis separations $r = 1a$,$2a$,...$24a$ for ensemble N6. 34
5.5 Attractive ground state $\bar{Q}\bar{Q}ud$ potentials and lowest lying repulsive $\bar{Q}\bar{Q}ud$ potentials for the ensembles A5, G8 and N6. 36
5.6 Difference between the two ground state potentials $V^{0;0,-,+}_{BB}(r)$ and $V^{0;0,-,-}_{BB}(r)$. 37
5.7 All attractive and repulsive $\bar{Q}\bar{Q}ud$ potentials with the lowest asymptotic value of $2m^S$ for ensemble N6 with separations grouped by symmetry. . . . 39
5.8 All attractive and repulsive $\bar{Q}\bar{Q}us$ potentials with asymptotic value $m^S_{\bar{Q}u/d} + m^S_{\bar{Q}s}$ for ensemble N6. 40
5.9 Effective mass plots for the most attractive potential $V^{0;0,-,+}_{\bar{Q}\bar{Q}ud,\text{eff}}(r)$ for on-axis separations $r = 3a$,...$8a$ for ensemble N6 compared to an artificially generated potential which creates a binding of 100 MeV. 42

8.1 Data points for the static potential of the ground state $V_0^{\Sigma_g^+}(r)$ and the first excited state $V_1^{\Sigma_g^+}(r)$, obtained by resampling and correcting the lattice results from [72] and data points with fits for $V_{\bar{Q}Q}(r)$, $V_{\bar{M}M}(r)$ and $V_{\text{mix}}(r)$. 54
8.2 Energy eigenvalues E_1, E_2, E_3 as a function of the separation r/a for the 3×3 potential matrix. 61

9.1 Det(T(E)) in the complex energy plane for $\bar{B}B$, $\tilde{J} = 1$ and physical and spurious poles found in the complex plane for $\tilde{J} = 1$ for integration distance $R = 20$ and $R = 24$. 66
9.2 Eigenphase sum $\delta_{\tilde{J}}$ for $\tilde{J} = 0$,1,2,3. 68
9.3 Bound state and resonance pole positions in the complex energy plane for angular momenta $\tilde{J} = 0$,1,2,3. 69
9.4 Eigenphase sum for $\bar{B}B$, $\tilde{J} = 2$ and a fit of the resonance at ≈ 10.800 GeV. 69

9.5 Percentages of quarkonium $\%\bar{Q}Q$ and meson-meson $(\%\bar{M}_{(s)}M_{(s)})_{L_{\text{out}}}$ content for bound states and resonances with $\tilde{J} = 0$. 71

10.1 Graphical summary of our theoretical predictions for bottomonium bound states and resonances in comparison to experimental results. 77

B.1 Effective mass plots corresponding to the most attractive potential $V^{0;0,-,+}_{\bar{Q}\bar{Q}ud,\text{eff}}(r)$ for off-axis separations for ensemble N6. Orange constants indicate the fitting range and results for $V^{0;0,-,+}_{\bar{Q}\bar{Q}ud}(r)$. 98

B.2 Effective mass plots corresponding to the repulsive potential $V^{0;0,-,-}_{\bar{Q}\bar{Q}ud,\text{eff}}(r)$ for on-axis separations $r = 1a,2a,...24a$ for ensemble N6. Orange constants indicate the fitting range and results for $V^{0;0,-,-}_{\bar{Q}\bar{Q}ud}(r)$. 99

B.3 All attractive (top) and repulsive (bottom) $\bar{Q}\bar{Q}us$ potentials with asymptotic value $m^S_{\bar{Q}u/d} + m^S_{\bar{Q}s}$ for ensemble A5. The gray data points and fits indicate corresponding results for $\bar{Q}\bar{Q}ud$. 100

B.4 All attractive (top) and repulsive (bottom) $\bar{Q}\bar{Q}us$ potentials with asymptotic value $m^S_{\bar{Q}u/d} + m^S_{\bar{Q}s}$ for ensemble G8. The gray data points and fits indicate corresponding results for $\bar{Q}\bar{Q}ud$. 101

C.1 Percentages of quarkonium $\%\bar{Q}Q$ and meson-meson $(\%\bar{M}_{(s)}M_{(s)})_{L_{\text{out}}}$ content for bound states and resonances with $\tilde{J} = 1$. 104

C.2 Percentages of quarkonium $\%\bar{Q}Q$ and meson-meson $(\%\bar{M}_{(s)}M_{(s)})_{L_{\text{out}}}$ content for bound states and resonances with $\tilde{J} = 2$. 105

C.3 Percentages of quarkonium $\%\bar{Q}Q$ and meson-meson $(\%\bar{M}_{(s)}M_{(s)})_{L_{\text{out}}}$ content for bound states and resonances with $\tilde{J} = 3$. 105

List of Tables

4.1 Remaining symmetries on the lattice for different separation axes. The first column displays the separation axis of the static anti-quark pair with numbers a, b, and c different from each other and 0. The fourth column shows which angular momenta mix. The last four columns show how these angular momenta are realized on the lattice in terms of the eigenvalues of the rotation operator $R_{|L|}(\theta)$ from Eqn. (4.26) with $\theta \in \{k \cdot 2\pi/n\}$ with $k < n, k \in \mathbb{N}_0$ acting on a trial state. 20

4.2 Quantum numbers and properties of the resulting $\bar{Q}\bar{Q}q_1q_2$ potentials: A = attractive, R = repulsive; SS, SP ,PP = asymptotic value $m^S_{\bar{Q}q_1} + m^S_{\bar{Q}q_2}$, $m^S_{\bar{Q}q_1} + m^{P_-}_{\bar{Q}q_2}$, $m^{P_-}_{\bar{Q}q_1} + m^{P_-}_{\bar{Q}q_2}$. 22

5.1 Lattice details and smearing parameters consistent with algorithms defined in Section 4.5.1 and 4.5.2. 29

5.2 Mass difference of the P_- and S meson for the ensembles A5, N6 and G8. . 30

5.3 Values for the tensor part $(\boldsymbol{\tau}_1 \cdot \boldsymbol{\tau}_2)(\boldsymbol{\sigma}_1 \cdot \hat{\mathbf{r}})(\boldsymbol{\sigma}_2 \cdot \hat{\mathbf{r}})$ of the one-pion-exchange potential. 38

5.4 Fitting parameters and binding energies for the most attractive potential $V^{(0);0,-,+}_{\bar{Q}\bar{Q}q_1q_2}(r)$. 41

8.1 Possibilities to couple $\tilde{J}^{PC}$ with $S^{PC}_{\bar{Q}}$ to J^{PC}. 51

8.2 Parameters of the potential parameterizations (8.14) and (8.16). 53

9.1 Percentages for quarkonium $\%\bar{Q}Q$ and meson-meson $(\%\bar{M}_{(s)}M_{(s)})_{\tilde{J}}$ of bound states and resonances for $\tilde{J} = 0,1,2,3$. 72

9.2 Our theoretical prediction for masses and decay widths found as poles of the T matrix for angular momenta $\tilde{J} = 0,1,2,3$ and corresponding experimental results. 73

9.3 Systematic analysis of our results with respect to $E_{\text{threshold}}$ and whether or not to correct the lattice results. 74

B.1 Fit parameters α, d, p and c from fitting the ansatz (5.4) to all attractive and repulsive $\bar{Q}\bar{Q}ud$ and $\bar{Q}\bar{Q}us$ potentials with asymptotic value $2m^S_{\bar{Q}\bar{Q}q_1q_2}$ for ensembles A5, G8 and N6. 102

Part III

Appendix

A Conventions

The following is a list of general conventions applied throughout this work.

- We use natural units, i.e. $\bar{h} = c = 1$.
- We use bold symbols $\mathbf{x}$ for three-dimensional vectors.
- Four-dimensional space-time vectors are expressed as x. However, depending on the context, this can also be the absolute value of a spatial vector.
- Greek indices run from $0, ..., 3$, while Latin indices run from $1, ..., 3$.
- Einstein's sum convention is implicitly applied unless stated otherwise.
- All lattice calculations are done in Euclidean space-time.

B Additional material for Part I - Antistatic-antistatic-light-light lattice QCD static potentials

B.1 Effective potentials

In Fig. B.1 we show the effective potential plots for corresponding to the most attractive potential $V^{0;0,-,+}_{\bar{Q}\bar{Q}ud,\mathrm{eff}}(r)$ for off-axis separations for ensemble N6.

In Fig. B.2 we show the effective potential plots for corresponding to the repulsive potential $V^{0;0,-,-}_{\bar{Q}\bar{Q}ud,\mathrm{eff}}(r)$ for on-axis separations $r = 1a$,$2a$,...$24a$ for ensemble N6.

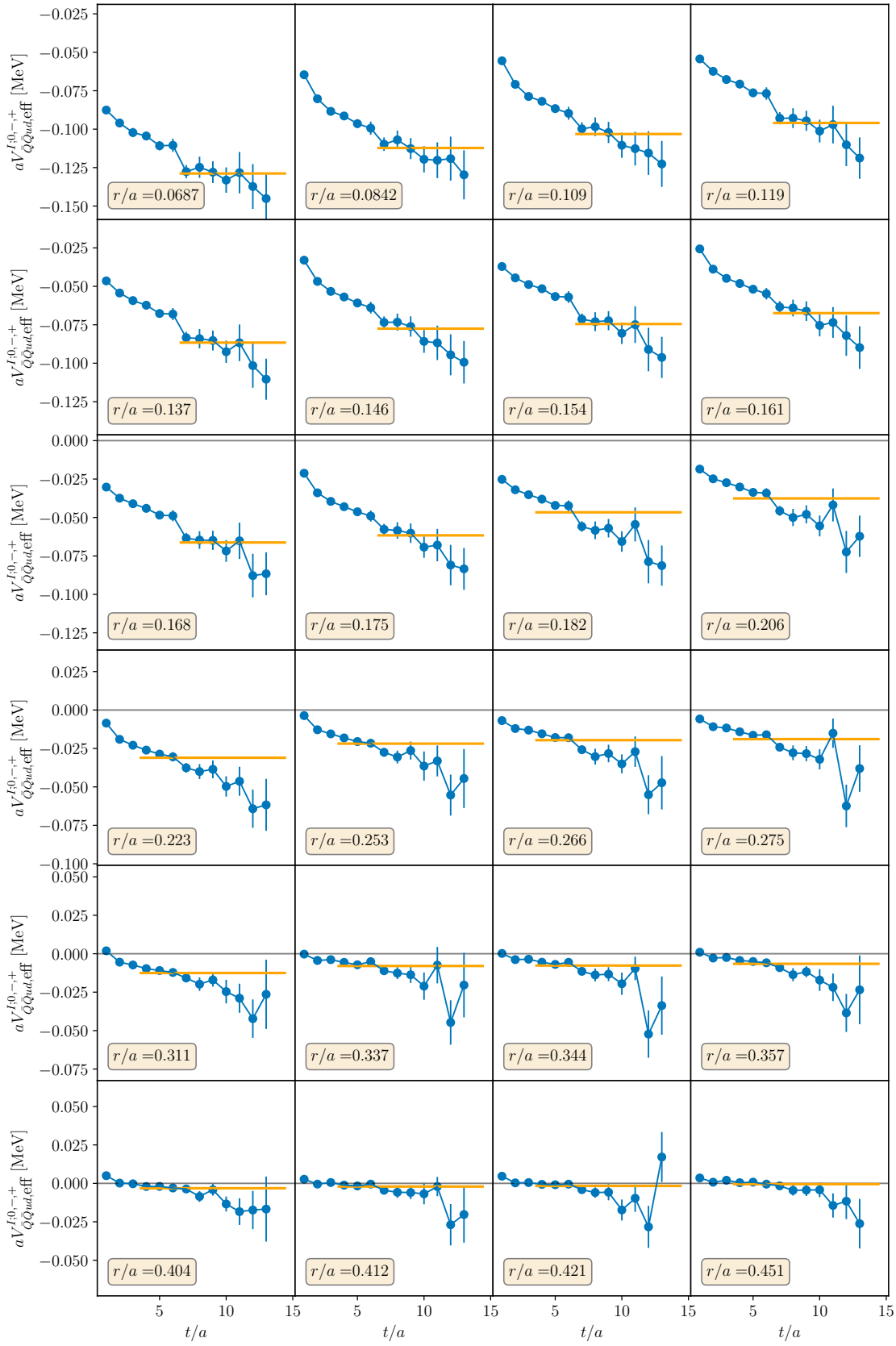

Figure B.1: Effective mass plots corresponding to the most attractive potential $V^{0;0,-,+}_{\bar{Q}\bar{Q}ud,\mathrm{eff}}(r)$ for off-axis separations for ensemble N6. Orange constants indicate the fitting range and results for $V^{0;0,-,+}_{\bar{Q}\bar{Q}ud}(r)$.

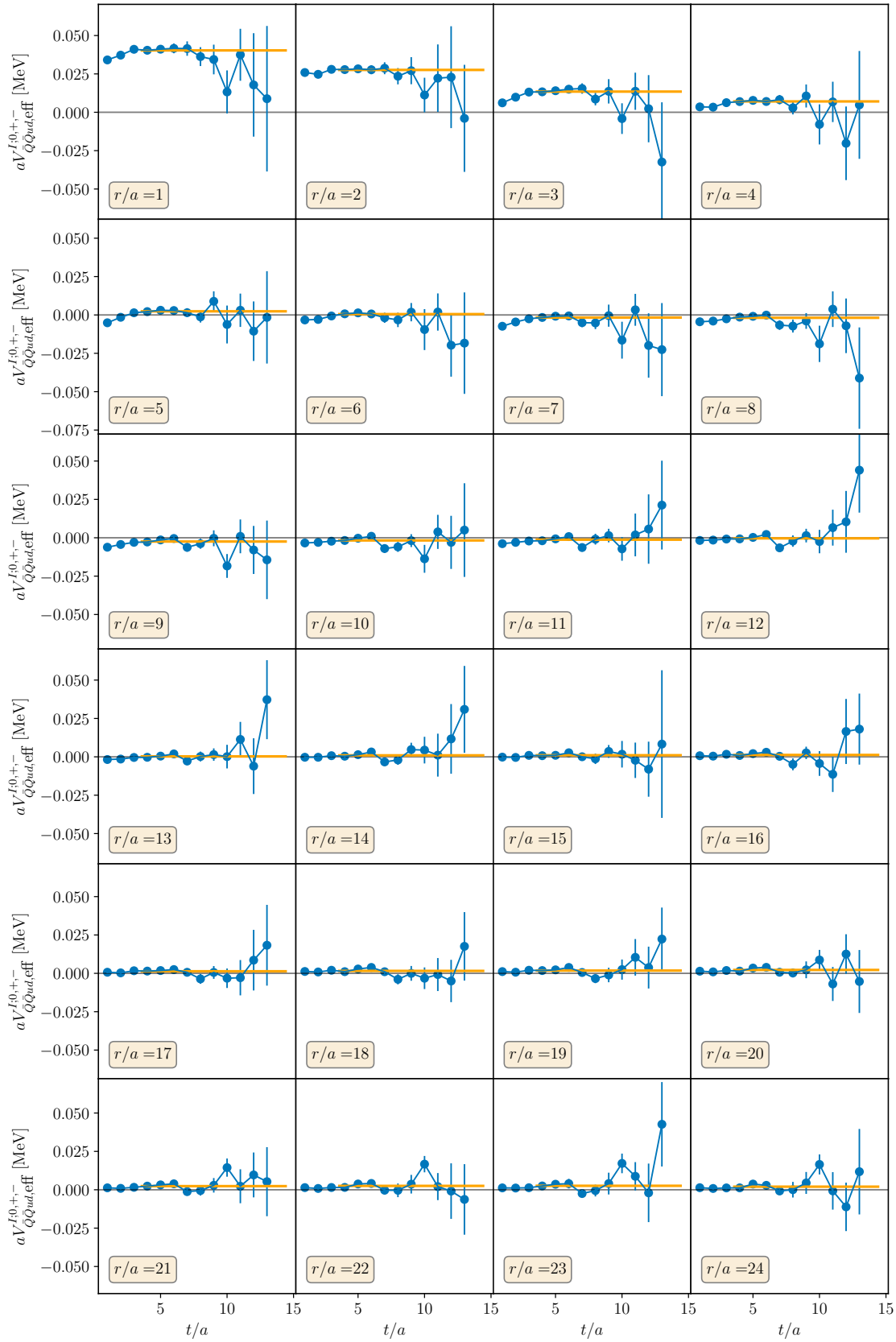

Figure B.2: Effective mass plots corresponding to the repulsive potential $V^{0;0,-,-}_{\bar{Q}\bar{Q}ud,\mathrm{eff}}(r)$ for on-axis separations $r = 1a,2a,...24a$ for ensemble N6. Orange constants indicate the fitting range and results for $V^{0;0,-,-}_{\bar{Q}\bar{Q}ud}(r)$.

B.2 $\bar{Q}\bar{Q}us$ potentials

In Figs. B.3 and B.4 we show all all attractive and repulsive $\bar{Q}\bar{Q}us$ potentials with asymptotic value $m^S_{\bar{Q}u/d} + m^S_{\bar{Q}s}$ for ensembles A5 and G8, respectively. The results for the corresponding $\bar{Q}\bar{Q}ud$ potential is indicated in gray.

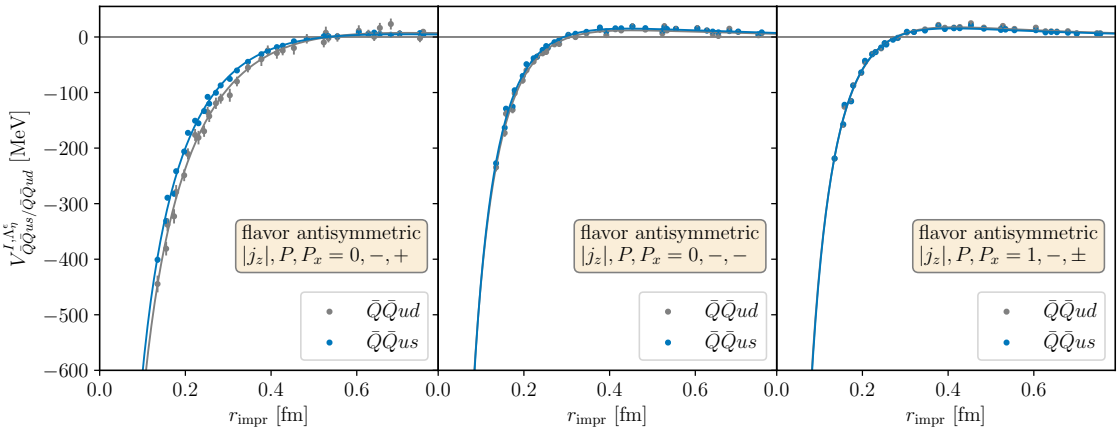

Figure B.3: All attractive (top) and repulsive (bottom) $\bar{Q}\bar{Q}us$ potentials with asymptotic value $m^S_{\bar{Q}u/d} + m^S_{\bar{Q}s}$ for ensemble A5. The gray data points and fits indicate corresponding results for $\bar{Q}\bar{Q}ud$.

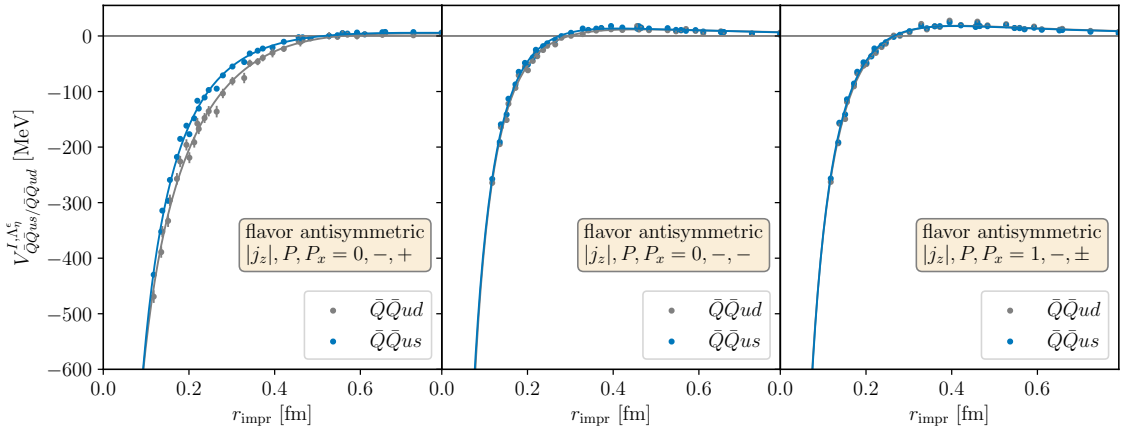

Figure B.4: All attractive (top) and repulsive (bottom) $\bar{Q}\bar{Q}us$ potentials with asymptotic value $m^S_{\bar{Q}u/d} + m^S_{\bar{Q}s}$ for ensemble G8. The gray data points and fits indicate corresponding results for $\bar{Q}\bar{Q}ud$.

B.3 Parameters from fitting of $\bar{Q}\bar{Q}q_1q_2$ static potentials

In Tab. B.1 we show fit parameters from fitting the ansatz (5.4) to all attractive and repulsive $\bar{Q}\bar{Q}q_1q_2$ potentials with asymptotic value $2m^S_{\bar{Q}\bar{Q}q_1q_2}$ for ensembles A5, G8 and N6.

Table B.1: Fit parameters α, d, p and c from fitting the ansatz (5.4) to all attractive and repulsive $\bar{Q}\bar{Q}ud$ and $\bar{Q}\bar{Q}us$ potentials with asymptotic value $2m^{S}_{\bar{Q}\bar{Q}q_1q_2}$ for ensembles A5, G8 and N6.

$\lvert j_z\rvert$,$\mathcal{P}$,$\mathcal{P}_x$	I	qq	Ens	α	d[fm]	p	c[MeV]
$0,-,+$	0	ud	A5	0.436(0.017)	0.569(0.033)	1.99(0.291)	160.783(7.0)
			G8	0.359(0.008)	0.552(0.028)	2.296(0.31)	128.346(4.185)
			N6	0.271(0.029)	0.349(0.052)	2.94(0.882)	18.834(71.255)
		us	A5	0.414(0.017)	0.467(0.025)	1.697(0.191)	153.333(5.872)
			G8	0.404(0.028)	0.409(0.034)	1.284(0.184)	154.298(9.575)
			N6	0.29(0.003)	0.613(0.021)	2.14(0.211)	104.966(2.72)
$0,-,-$	1	ud	A5	0.511(0.11)	0.223(0.054)	1.041(0.185)	321.065(67.628)
			G8	0.772(0.321)	0.103(0.061)	0.666(0.163)	500.743(203.976)
			N6	0.3(0.019)	0.361(0.034)	1.089(0.109)	197.904(12.372)
		us	A5	0.63(0.139)	0.176(0.047)	0.866(0.128)	415.629(91.408)
			G8	0.524(0.089)	0.18(0.036)	0.937(0.123)	369.647(61.812)
			N6	0.308(0.018)	0.309(0.026)	1.042(0.086)	208.133(11.788)
$1,-,\pm$	1	ud	A5	0.487(0.072)	0.241(0.038)	1.098(0.138)	338.999(50.312)
			G8	0.412(0.053)	0.259(0.038)	1.105(0.147)	295.658(38.197)
			N6	0.267(0.008)	0.375(0.014)	1.532(0.114)	197.893(6.329)
		us	A5	0.545(0.095)	0.207(0.039)	1.027(0.136)	377.286(65.517)
			G8	0.455(0.061)	0.224(0.035)	1.011(0.123)	331.715(44.475)
			N6	0.282(0.012)	0.342(0.018)	1.324(0.109)	208.92(8.858)
$0,+,+$	1	ud	A5	-0.943(1.041)	0.034(0.056)	0.5(0.197)	-571.561(625.001)
			G8	-0.146(0.007)	0.465(0.026)	1.887(0.264)	-75.14(3.984)
			N6	-0.112(0.01)	0.353(0.05)	1.955(0.707)	-55.178(5.57)
		us	A5	-0.262(0.069)	0.214(0.065)	0.972(0.193)	-174.992(46.584)
			G8	-0.146(0.013)	0.354(0.034)	1.448(0.245)	-68.394(5.644)
			N6	-0.113(0.005)	0.465(0.034)	1.964(0.364)	-65.482(3.429)
$0,+,-$	0	ud	A5	-0.277(2.576)	0.099(25.522)	1.154(38.577)	1.18(167124.486)
			G8	-0.163(0.035)	0.259(0.061)	1.227(0.317)	-99.655(20.296)
			N6	-0.11(0.013)	0.294(0.04)	1.626(0.528)	-70.103(7.493)
		us	A5	-0.141(0.017)	0.314(0.031)	1.8(0.268)	-112.528(14.554)
			G8	-0.152(0.018)	0.285(0.034)	1.382(0.205)	-116.02(13.571)
			N6	-0.118(0.011)	0.289(0.032)	1.318(0.235)	-83.413(7.377)
$1,+,\pm$	0	ud	A5	-0.142(0.03)	0.552(0.122)	1.378(0.39)	-100.427(23.792)
			G8	-0.157(0.026)	0.419(0.081)	1.224(0.261)	-116.556(21.042)
			N6	-0.096(0.004)	0.543(0.034)	1.684(0.179)	-73.065(4.289)
		us	A5	-0.157(0.025)	0.411(0.057)	1.375(0.205)	-139.574(23.234)
			G8	-0.145(0.014)	0.387(0.036)	1.438(0.181)	-120.47(12.474)
			N6	-0.097(0.003)	0.571(0.02)	2.441(0.219)	-85.075(3.63)

C Additional material for Part II - Bottomonium resonances in the Born-Oppenheimer approxima- tion using lattice QCD static potentials

C.1 Percentages of quarkonium and meson-meson composition

In Figs. C.1-C.3 we show the percentages of quarkonium $\%\bar{Q}Q$ and meson-meson $(\%\bar{M}_{(s)}M_{(s)})_{L_{\rm out}}$ content for bound states and resonances with $\tilde{J} = 1, 2, 3$.

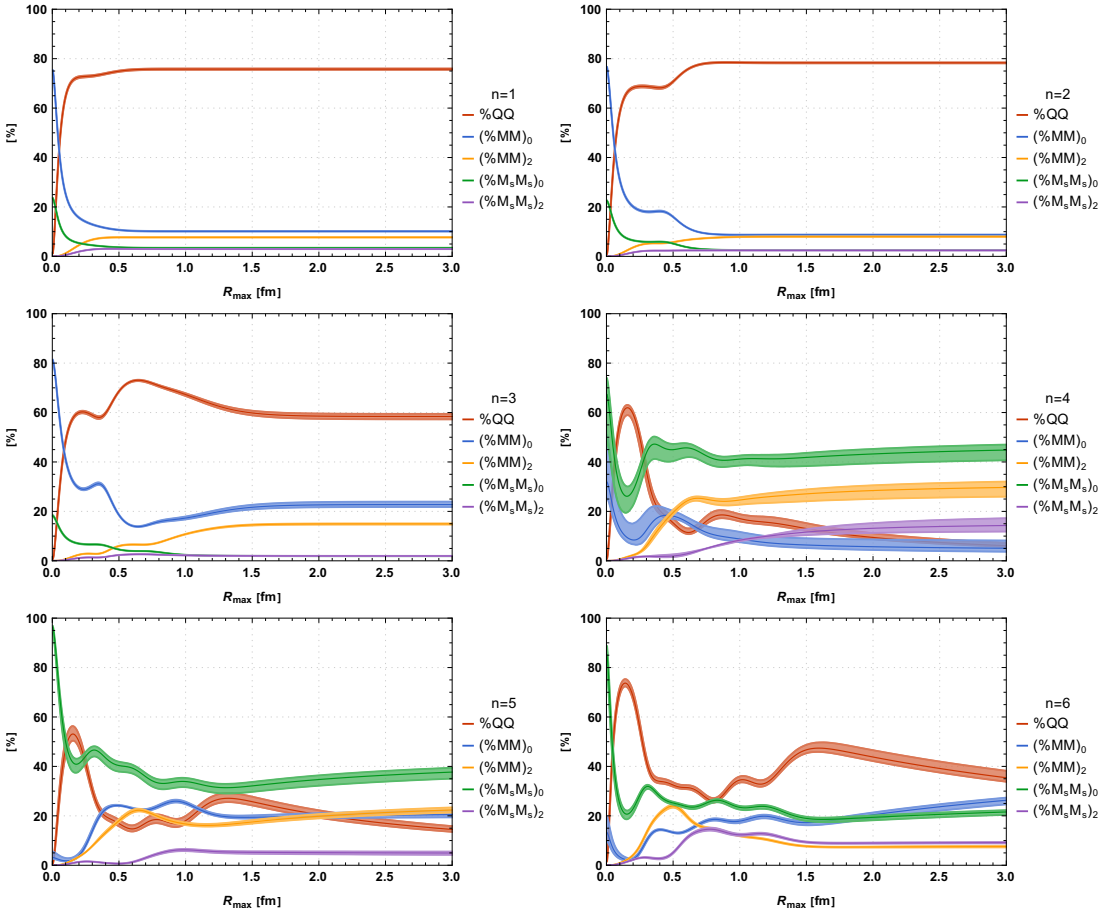

Figure C.1: Percentages of quarkonium $\%\bar{Q}Q$ and meson-meson $(\%\bar{M}_{(s)}M_{(s)})_{L_{\text{out}}}$ content for bound states and resonances with $\tilde{J} = 1$.

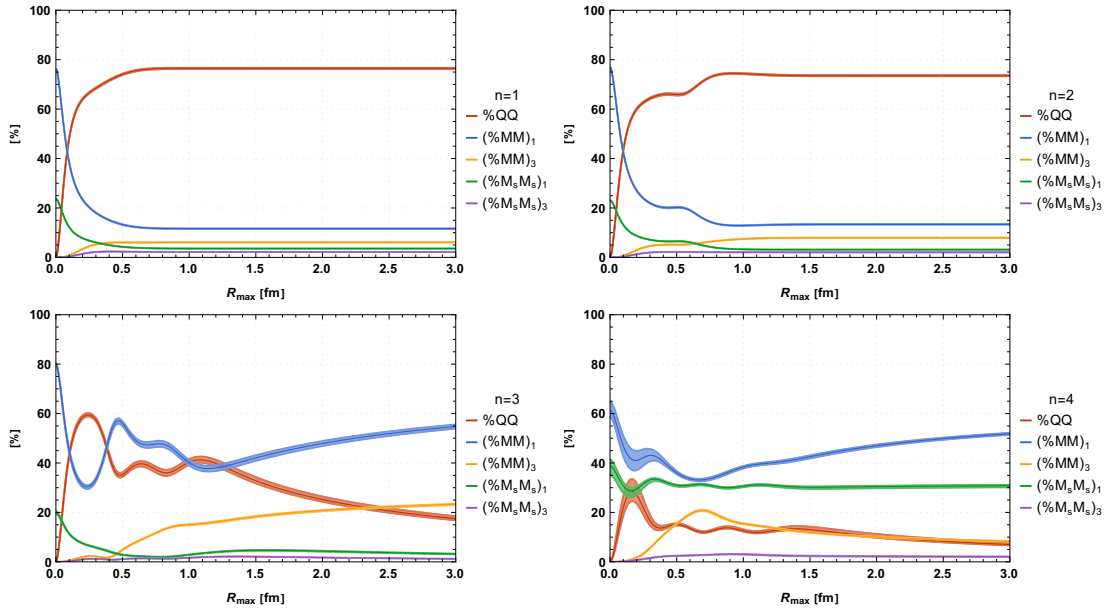

Figure C.2: Percentages of quarkonium $\%\bar{Q}Q$ and meson-meson $(\%\bar{M}_{(s)}M_{(s)})_{L_{\rm out}}$ content for bound states and resonances with $\tilde{J} = 2$.

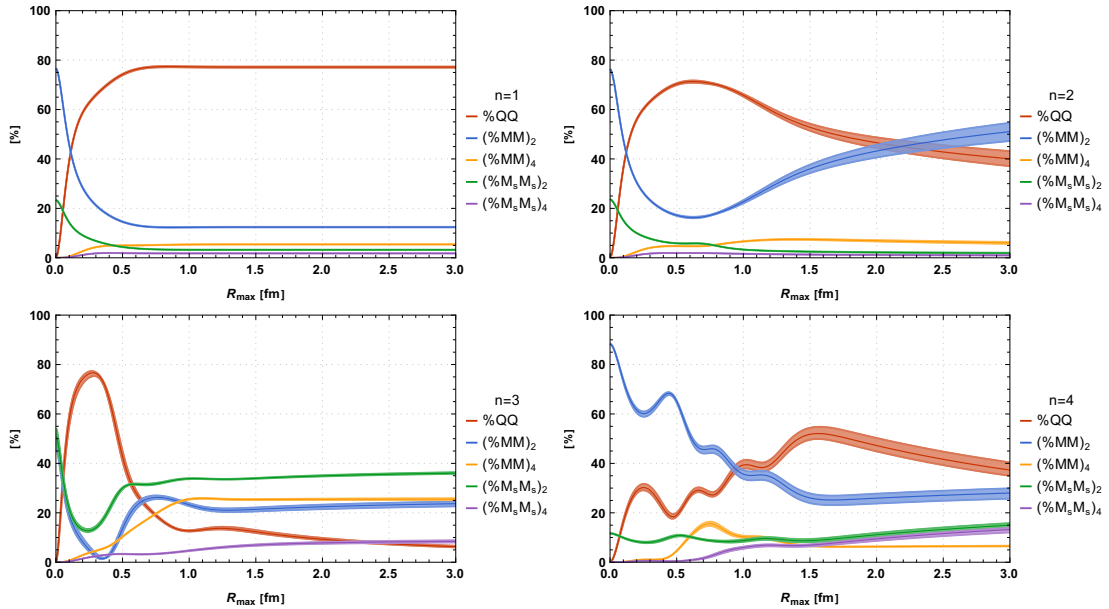

Figure C.3: Percentages of quarkonium $\%\bar{Q}Q$ and meson-meson $(\%\bar{M}_{(s)}M_{(s)})_{L_{\rm out}}$ content for bound states and resonances with $\tilde{J} = 3$.

Acknowledgments

First, I would like to thank Marc for his excellent supervision throughout the years. Not only was it always possible to discuss physics, but he also supported me as a young scientist, enabling my contributions to many conferences and promoting me for scholarships and awards.

I would also like to thank Pedro Bicudo for our interesting physics discussions, particularly when we spoke in person. He always provided a different perspective on our research, which is incredibly valuable and important.

Furthermore, I want to thank Marina Marinkovic for providing the code base for my work and all the related support I could ask for. I also thank her for the opportunity to spend one month at ETH Zurich and for a great collaboration. I thank Daniel Mohler who kindly served as an external supervisor in my PhD Committee and provided helpful input to our projects.

I want to thank my colleague and friend Laurin Pannullo for a fantastic time at the office. I thank all current and past members of our working group who always discussed great topics related and unrelated to physics during coffee and lunch breaks.

Last, I want to thank Mariana who was incredibly patient with me going through the process of writing this thesis.

I acknowledge support by a Karin and Carlo Giersch Scholarship of the Giersch foundation for the first three years of my PhD. I acknowledge funding by the Deutsche Forschungsgemeinschaft (DFG, project number 457742095).

I acknowledge access to Piz Daint at the SwissNational Supercomputing Centre, Switzerland under the ETHZ's share with the project ID eth8 and s1193. Computations on the GOETHE-NHR and on the FUCHS-CSC high-performance computers of the Frankfurt University were conducted for this research. I would like to thank HPC-Hessen, funded by the State Ministry of Higher Education, Research and the Arts, for programming advice.

Lasse Falk Mueller

Personal Data

Birth **March 05th, 1994**, *at Frankfurt a. M.*

Address **Am Niddatal 7**, *60488*, Frankfurt

E-mail **lasse.mueller@outlook.de**

Mobile **+49 174 788 3564**

Education

2010–2013 **Abitur (equivalent to A-level)**, *Max-Beckmann-Schule*, Frankfurt am Main, *final grade: 1,5*

2013–2014 **Bachelor of Science Environmental Engineering**, *Technische Universität Darmstadt*, Darmstadt, *not completed*

2014–2018 **Bachelor of Science Physics**, *Goethe University Frankfurt*, Frankfurt am Main, *final grade: 1,7*

2018–2019 **Master of Science Physics**, *Goethe University Frankfurt*, Frankfurt am Main, *final grade: 1,2*

2019-2024 **PhD Physics**, *Goethe University Frankfurt*, Frankfurt am Main

Bachelor Thesis

title *Investigation of the structure of hybrid static potential flux tubes*

grade *1,0*

supervisor Prof. Marc Wagner

Master Thesis

titel *Structure of hybrid static potential flux tubes in SU(2) and SU(3) lattice Yang-Mills theory*

grade *1,0*

supervisor Prof. Marc Wagner

Teaching

Tutorials

WS 2016/17 Mathematics for physics students I

SS 2017 Mathematics for physics students II

WS 2017/18 Mathematics for physics students I

SS 2018	Mathematics for physics students II
WS 2018/19	Theoretical physics III (electrodynamics)
SS 2019	Higher quantum mechanics
WS 2019/20	Introduction to programming for physics students
SS 2020	Theoretical Physics II (classical mechanics and special relativity)
WS 2020/21	Theoretical Physics III (electrodynamics)
SS 2021	Numerical methods in physics
WS 2021/22	Theoretical Physics I (mathematical methods)
SS 2022	Theoretical Physics II (classical mechanics and special relativity)
WS 2022/23	Theoretical Physics V (statistical mechanics and thermodynamics)
SS 2023	Higher quantum mechanics
WS 2023/24	Numerical methods in physics
SS 2024	Introduction to programming for physics students

Talks

Aug 2023	Lasse Müller, Pedro Bicudo, Marina Marinkovic, Marc Wagner **Anti-static-anti-static-light-light potentials from lattice QCD** Talk presentation at 40th International Symposium on Lattice Field Theory at Fermilab in Naperville, USA
Aug 2022	Lasse Müller, Pedro Bicudo, Nuno Cardoso, Marc Wagner **Study of $I = 0$ bottomonium bound states and resonances based on lattice QCD static potentials** Poster presentation at 39th International Symposium on Lattice Field Theory in Bonn, Germany
Jul 2021	Lasse Müller, Pedro Bicudo, Nuno Cardoso, Marc Wagner **Bottomonium resonances from lattice QCD static-static-light-light potentials** Talk at 38th International Symposium on Lattice Field Theory (Online Conference)
Aug 2020	Lasse Müller, Pedro Bicudo, Nuno Cardoso, Marc Wagner **Bottomonium resonances from lattice QCD static-static-light-light potentials** Talk at Asia-Pacific Symposium für Lattice Field Theory 2020 (Online Conference)
Aug 2018	Lasse Müller, Owe Philipsen, Christian Reisinger, Marc Wagner **Structure of hybrid static potential flux tubes in lattice Yang-Mills theory** Invited talk at Confinement XIII conference in Maynooth, Ireland
Mär 2018	Lasse Müller, Marc Wagner **Structure of hybrid static potential flux tubes in SU(2) lattice Yang-Mills theory** Invited talk at Excited QCD 2018 conference in Kopaonik, Serbia

Publications

Sep 2024 Lasse Müller, Pedro Bicudo, Marina Marinkovic, Marc Wagner
Antistatic-antistatic $\bar{Q}\bar{Q}qq$ potentials for u, d and s light quarks from lattice QCD
to be published.
arXiv: 2409.10786 [hep-lat]

Dec 2023 Lasse Müller, Pedro Bicudo, Marina Marinkovic, Marc Wagner
Antistatic-antistatic-light-light potentials from lattice QCD
published in: **PoS LATTICE2023, 064 (2024)**
arXiv: 2312.17060 [hep-lat]

May 2022 Pedro Bicudo, Nuno Cardoso, Lasse Müller, Marc Wagner
Study of I=0 bottomonium bound states and resonances in S, P, D and F waves with lattice QCD static-static-light-light potentials
published in: **Phys. Rev. D 107, 094515 (2023)**
arXiv: 2205.11475 [hep-lat]

Aug 2021 Pedro Bicudo, Nuno Cardoso, Lasse Müller, Marc Wagner
Bottomonium resonances from lattice QCD static-static-light-light potentials
published in: **PoS LATTICE2021, 349 (2021)**
arXiv: 2108.08100 [hep-lat]

Aug 2020 Pedro Bicudo, Nuno Cardoso, Lasse Müller, Marc Wagner
Computation of the quarkonium and meson-meson composition of the Υ(nS) states and of the new Υ(10753) Belle resonance from lattice QCD static potentials
published in: **Phys. Rev. D 103, 074507 (2021)**
arXiv: 2008.05605 [hep-lat]

Jul 2019 Lasse Müller, Owe Philipsen, Christian Reisinger, Marc Wagner
Hybrid static potential flux tubes from SU(2) and SU(3) lattice gauge theory
published in: **Phys. Rev. D 100, 054503 (2019)**
arXiv:1907.01482 [hep-lat]

Nov 2018 Lasse Müller, Owe Philipsen, Christian Reisinger, Marc Wagner
Structure of hybrid static potential flux tubes in lattice Yang-Mills theory
published in: **PoS Confinement2018, 053 (2018)**
arXiv: 1811.00452 [hep-lat]

Oct 2018 Christian Reisinger, Stefano Capitani, Lasse Müller, Owe Philipsen, Marc Wagner
Computation of hybrid static potentials from optimized trial states in SU(3) lattice gauge theory
published in: **PoS LATTICE2018, 054 (2018)**
arXiv: 1810.13284 [hep-lat]

Mar 2018 Lasse Müller, Marc Wagner
Structure of hybrid static potential flux tubes in SU(2) lattice Yang-Mills theory
published in: **Acta Phys. Pol. B Proceedings Supplement, Vol. 11, No. 3, 2018, page 551**
arXiv: 1803.11124 [hep-lat]

Skills

Language English(fluent) French(basic) Spanish(basic)

Computer Programming (Python, Fortran, C, C++, Haskell), LaTeX, Microsoft Office